

Characterisation of SCUBA-2 450 μ m and 850 μ m-selected Galaxies in the COSMOS Field

Caitlin M. Casey^{1*}, Chian-Chou Chen¹, Lennox L. Cowie¹, Amy J. Barger^{1,2,3}, Peter Capak⁴, Olivier Ilbert⁵, Michael Koss¹, Nicholas Lee¹, Emeric Le Floc’h⁶, David B. Sanders¹, Jonathan P. Williams¹

¹ *Institute for Astronomy, University of Hawai’i, 2680 Woodlawn Dr, Honolulu, HI 96822, USA*

² *Department of Astronomy, University of Wisconsin-Madison, 475 North Charter Street, Madison, WI 53706, USA*

³ *Department of Physics and Astronomy, University of Hawai’i, 2505 Correa Road, Honolulu, HI 96822, USA*

⁴ *Spitzer Science Center, California Institute of Technology, 1200 E. California Blvd, Pasadena, CA, 91125, USA*

⁵ *Laboratoire d’Astrophysique de Marseille, 38 rue Frederic Joliot Curie, 13388 Marseille, France*

⁶ *CEA-Saclay, Orme des Merisiers, Bat. 709, 91191 Gif-sur-Yvette, France*

Submitted 1 November 2021.

ABSTRACT

We present deep 450 μ m and 850 μ m observations of a large, uniformly covered 394 arcmin² area in the COSMOS field obtained with the SCUBA-2 instrument on the James Clerk Maxwell Telescope (JCMT). We achieve root-mean-square noise values of $\sigma_{450}=4.13$ mJy and $\sigma_{850}=0.80$ mJy. The differential and cumulative number counts are presented and compared to similar previous works. Individual point sources are identified at $>3.6\sigma$ significance, a threshold corresponding to a 3–5% sample contamination rate. We identify 78 sources at 450 μ m and 99 at 850 μ m, with flux densities $S_{450}=13\text{--}37$ mJy and $S_{850}=2\text{--}16$ mJy. Only 62–76% of 450 μ m sources are 850 μ m detected and 61–81% of 850 μ m sources are 450 μ m detected. The positional uncertainties at 450 μ m are small (1–2.5'') and therefore allow a precise identification of multiwavelength counterparts without reliance on detection at 24 μ m or radio wavelengths; we find that only 44% of 450 μ m-sources and 60% of 850 μ m-sources have 24 μ m or radio counterparts. 450 μ m-selected galaxies peak at $\langle z \rangle = 1.95 \pm 0.19$ and 850 μ m-selected galaxies peak at $\langle z \rangle = 2.16 \pm 0.11$. The two samples occupy similar parameter space in redshift and luminosity, while their median SED peak wavelengths differ by $\sim 20\text{--}50\mu$ m (translating to $\Delta T_{\text{dust}} = 8\text{--}12$ K, where 450 μ m-selected galaxies are warmer). The similarities of the 450 μ m and 850 μ m populations, yet lack of direct overlap between them, suggests that submillimeter surveys conducted at any single far-infrared wavelength will be significantly incomplete ($\gtrsim 30\%$) at censusing infrared-luminous star formation at high- z .

Key words: galaxies: evolution – galaxies: high-redshift – galaxies: infrared – galaxies: starbursts

1 INTRODUCTION

The arrival of the Submillimeter Common User Bolometer Array (SCUBA; Holland et al. 1999) on the James Clerk Maxwell Telescope (JCMT) fifteen years ago ushered in a new age of galaxy evolution studies by highlighting the importance of distant infrared-bright, ultraluminous galaxies to the buildup of the Universe’s stellar mass and the forma-

tion of massive, local elliptical galaxies. Submillimeter galaxies (SMGs, canonically selected at 850 μ m with $S_{850} \gtrsim 2\text{--}5$ mJy; Smail et al. 1997; Barger et al. 1998; Hughes et al. 1998; Eales et al. 1999) have since been shown to have a peak volume density at $z \approx 2.2\text{--}2.5$ (Chapman et al. 2003, 2005; Yun et al. 2012).

Follow-up studies of their molecular and ionised gas properties (Swinbank et al. 2004; Neri et al. 2003; Greve et al. 2005; Tacconi et al. 2006, 2008; Bothwell et al. 2010; Engel et al. 2010; Banerji et al. 2011; Alaghband-Zadeh et al. 2012) indicate that most star formation in bright SMGs is

* Hubble Fellow; cmcasey@ifa.hawaii.edu

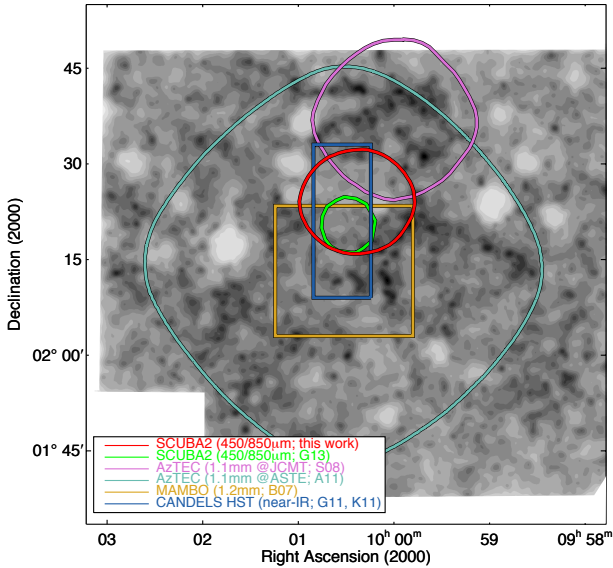


Figure 1. The surface density of galaxies showing large scale structure in the COSMOS field (darker shades indicate the most dense areas). This uses the most recent compilation in Scoville et al. (2013). Overplotted are the areas surveyed in the submillimeter at 1.2 mm (with MAMBO, *gold*; Bertoldi et al. 2007), at 1.1 mm (with AzTEC on JCMT, *lavender*; Scott et al. 2008), at 1.1 mm (with AzTEC on ASTE, *teal*; Aretxaga et al. 2011). Our 450/850 μm SCUBA-2 coverage area is shown in *red*, and the SCUBA-2 coverage of Geach et al. (2013) and Roseboom et al. (2013) is shown in *green*. The CANDELS deep near-infrared HST coverage area is shown in *blue*.

triggered by major mergers of gas-rich disk galaxies, similar to local (ultra-) luminous infrared galaxies, (U)LIRGs (e.g. Sanders et al. 1988; Sanders & Mirabel 1996; Armus et al. 2009; U et al. 2012). Furthermore, several detailed studies of the X-ray and mid-infrared properties of SMGs have led to the conclusion that the majority of the SMGs’ bolometric energy is star formation dominated (Alexander et al. 2005; Pope et al. 2008; Coppin et al. 2008; Menéndez-Delmestre et al. 2009; Coppin et al. 2010; Laird et al. 2010). However, several recent studies have pointed out that, despite their extreme star formation rates $\gtrsim 200 M_{\odot} \text{yr}^{-1}$, SMGs and high- z ULIRGs are not homogeneously described by major mergers (e.g. Daddi et al. 2009; Bothwell et al. 2010; Elbaz et al. 2011; Rodighiero et al. 2011; Alaghband-Zadeh et al. 2012; Hayward et al. 2012; Targett 2011). It is clear that the driving physical mechanisms for SMGs remains a puzzle at high- z despite these detailed multiwavelength studies.

The limiting factors in the analysis and characterisation of SMGs is small number statistics and the lack of secure counterpart identifications. The vast majority of the studies mentioned above—although thorough—are based on small samples of SMGs, anywhere from 2-75 galaxies (but mostly on samples with less than ten sources). Some of these SMGs could have been mischaracterised due to incorrect counterpart identifications, which may be a consequence of the large beamsize of submm single-dish observations (the JCMT beamsize at 850 μm is $\sim 15''$). The

problem of limited statistics can be alleviated by wide-field submillimetre mapping. Mapping large regions of sky at long wavelengths is technically challenging, particularly if the maps are intended to be sufficiently deep and sensitive enough to detect unlensed galaxies in the early Universe. New submillimeter/far-infrared (FIR) facilities, such as AzTEC (Wilson et al. 2008) and primarily *Herschel Space Observatory* (Pilbratt et al. 2010), have mapped larger sky areas in recent years. *Herschel* has mapped hundreds of square degrees at 250–500 μm (Eales et al. 2010; Oliver et al. 2012). However, its surveys are more limited in sensitivity than SCUBA, primarily due to the smaller primary dish, which results in large beam sizes and much higher confusion limits.

The new Submillimeter Common User Bolometric Array-2 (SCUBA-2 Holland et al. 2013) instrument on JCMT presents exciting new avenues to explore infrared-bright starbursts in the early Universe. Besides the four-fold increase in bolometer arrays and large field-of-view scans, which make 850 μm mapping more efficient than it was with SCUBA, the SCUBA-2 450 μm bolometers provide the first opportunity to identify 450 μm -bright sources with remarkable resolution in the FIR; the JCMT beamsize at 450 μm is $\sim 7''$, compared to $\sim 36''$ at 500 μm on *Herschel*. Direct detection in the FIR with a small beamsize is a large step forward, since multiwavelength counterpart identification has been a key limiting factor in the interpretation of submillimeter-bright sources over the past decade. Deep SCUBA-2 maps, which are much less limited by confusion noise, are the scientific complement to the large-scale mapping done with *Herschel*.

This paper presents 450 μm and 850 μm observations from SCUBA-2 in a central region of the Cosmic Evolution Survey (COSMOS) field (Scoville et al. 2007) surrounding the Cosmic Assembly Near-infrared Deep Extragalactic Legacy Survey (CANDELS) area. Recently, Geach et al. (2013) presented deep SCUBA-2 450 μm observations in the central $\sim 100 \text{ arcmin}^2$ of this area. Our observations have a wider, more uniform coverage than the data presented in Geach et al. (2013), with the motivation of selecting a homogeneous sample, while the Geach et al. (2013) data are deeper and patterned to find fainter sources. The pointing on the CANDELS area is motivated by the perceived high correlation of submillimeter emission with near-infrared emission (e.g. Wang et al. 2006; Serjeant et al. 2008) and the ability to morphologically characterise SMG counterparts using the *Hubble Space Telescope’s* high spatial resolution. However, we leave the detailed morphological analysis of these galaxies to a future work. This work is also complemented by the deeper, yet smaller area SCUBA-2 coverage and analysis in the lensed cluster field A 370 by Chen et al. (2013), which currently provides the deepest 450 μm counts.

Section 2 describes our SCUBA-2 observations and data reduction as well as ancillary data used, section 3 discusses the identification and flux density measurements of point sources in the maps and differential and cumulative number counts, section 4 describes the multiwavelength properties of the SCUBA-2-selected galaxies, and section 5 discusses their implications, relation to similar starburst galaxy populations, and implications for future, deeper SCUBA-2 observations. Throughout we assume a Λ CDM cosmology with $H_0 = 71 \text{ km s}^{-1} \text{ Mpc}^{-1}$ and $\Omega_m = 0.27$ (Hinshaw et al. 2009).

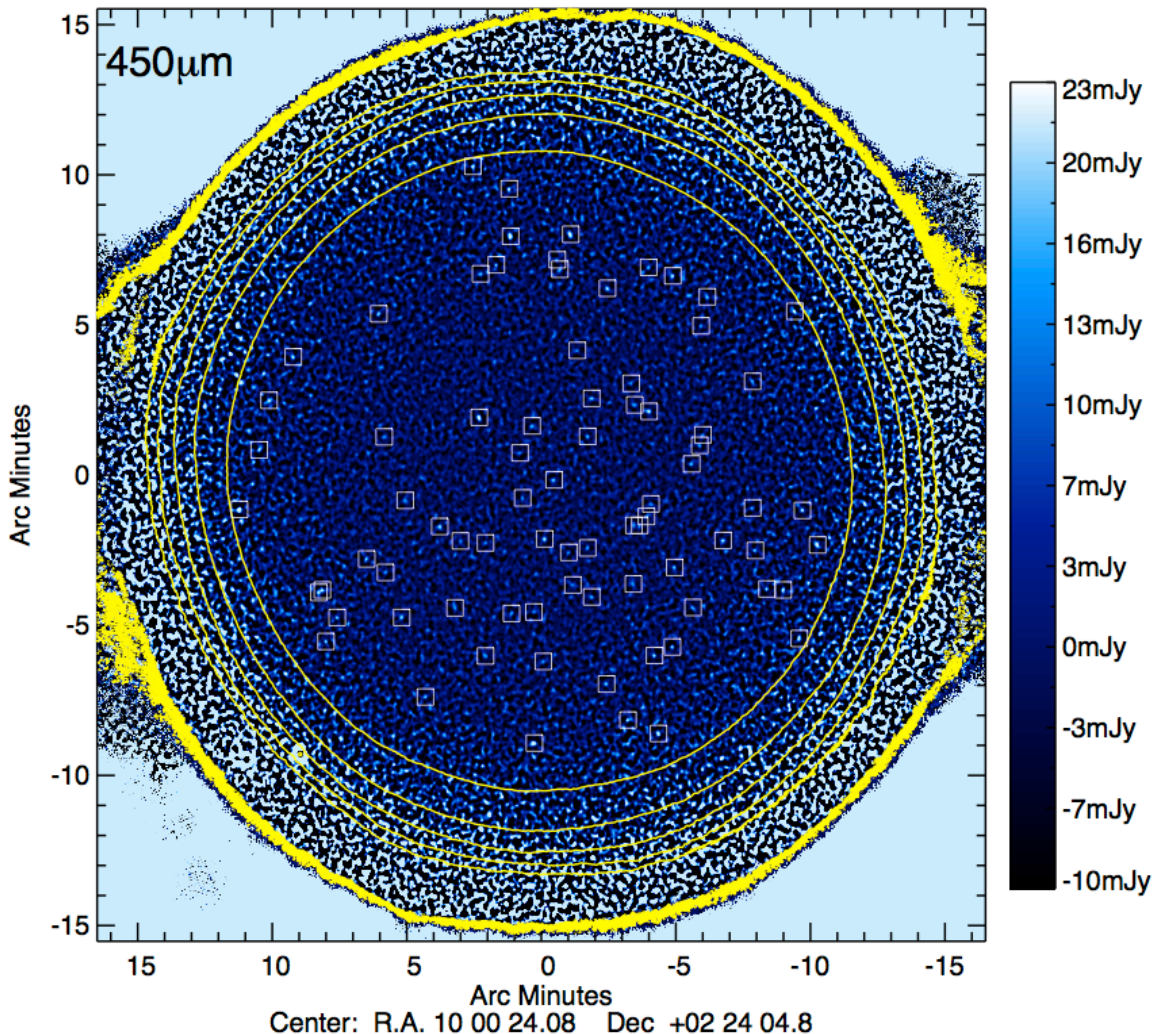


Figure 2. The COSMOS $450\mu\text{m}$ SCUBA-2 map. The colour scale is linear with upper and lower ranges of $-10 < S_{450} < 23$ mJy/beam. Contours mark the 2, 3, 4, 5, and $6\times$ the central RMS value, measured to be 4.13 mJy/beam at $450\mu\text{m}$. We search for sources which are detected with RMS less than double the central value (roughly corresponding to the inner most contour). The area probed by this cut has a radius ~ 11.2 arcmin and an area ~ 394 arcmin 2 . The $450\mu\text{m}$ -identified $>3.6\sigma$ sources are identified with white boxes (a justification of the 3.6σ cut can be found in the text).

2 OBSERVATIONS & DATA

Observations were taken with the SCUBA-2 instrument on the JCMT on 2011-Dec-26, 2011-Dec-28, 2012-Feb-04, 2012-Feb-05, 2012-Feb-07, 2012-Apr-09, 2012-Apr-30, 2012-May-01, 2012-May-02, and 2012-Dec-21 under programs M11BH11A, M12AH11A and M12BH21A. Conditions were optimum, with the optical depth varying from $0.02 < \tau_{225\text{GHz}} < 0.05$ and averaging $\tau_{225\text{GHz}} \approx 0.04$. At the wavelengths of our observations, the optical depths were approximately $\tau_{450\mu\text{m}} \approx 0.55$ and $\tau_{850\mu\text{m}} \approx 0.16$. The integration times on-field per night were 3.5 hrs, 3.6 hrs, 3.1 hrs, 5.5 hrs, 5.5 hrs, 4.5 hrs, 2.9 hrs, 3.8 hrs, 0.6 hrs and 5.0 hrs respectively, totalling 38.0 hrs on-field. We centred our map at position 10:00:28.0, +02:24:00. See Figure 1 for a map of the galaxy density in the surrounding area along with areas covered at other submm–mm wavelengths. The PONG-900 mapping pattern was used to achieve a uniform RMS over a

large area $\approx 15 \times 15$ arcmin in preference to the Daisy mapping which has substantial patterning and non-uniformity and covers a smaller area.

Raw data were downloaded via the Canadian Astronomy Data Centre (CAD) JCMT Science Archive and processed with the SCUBA-2 software packages SMURF, the Sub-Millimetre User Reduction Facility, and PICARD, Pipeline for Combining and Analyzing Reduced Data. Data were split up by night, wavelength, and sub-array for processing. SMURF processing was first executed on each night’s sub-array data (which is equivalent to combining each sub-array per Minimum Scheduable Block (MSB), and then combining all MSBs). Partial maps were constructed using the MAKEMAP routine (Chapin et al. 2013) in SMURF with the default deep extragalactic configuration file optimising background subtraction. The MAKEMAP uncalibrated maps were combined at each stage (by sub-array, then nights) using the PICARD recipe MOSAIC_JCMT_IMAGES. Each of the four sub-

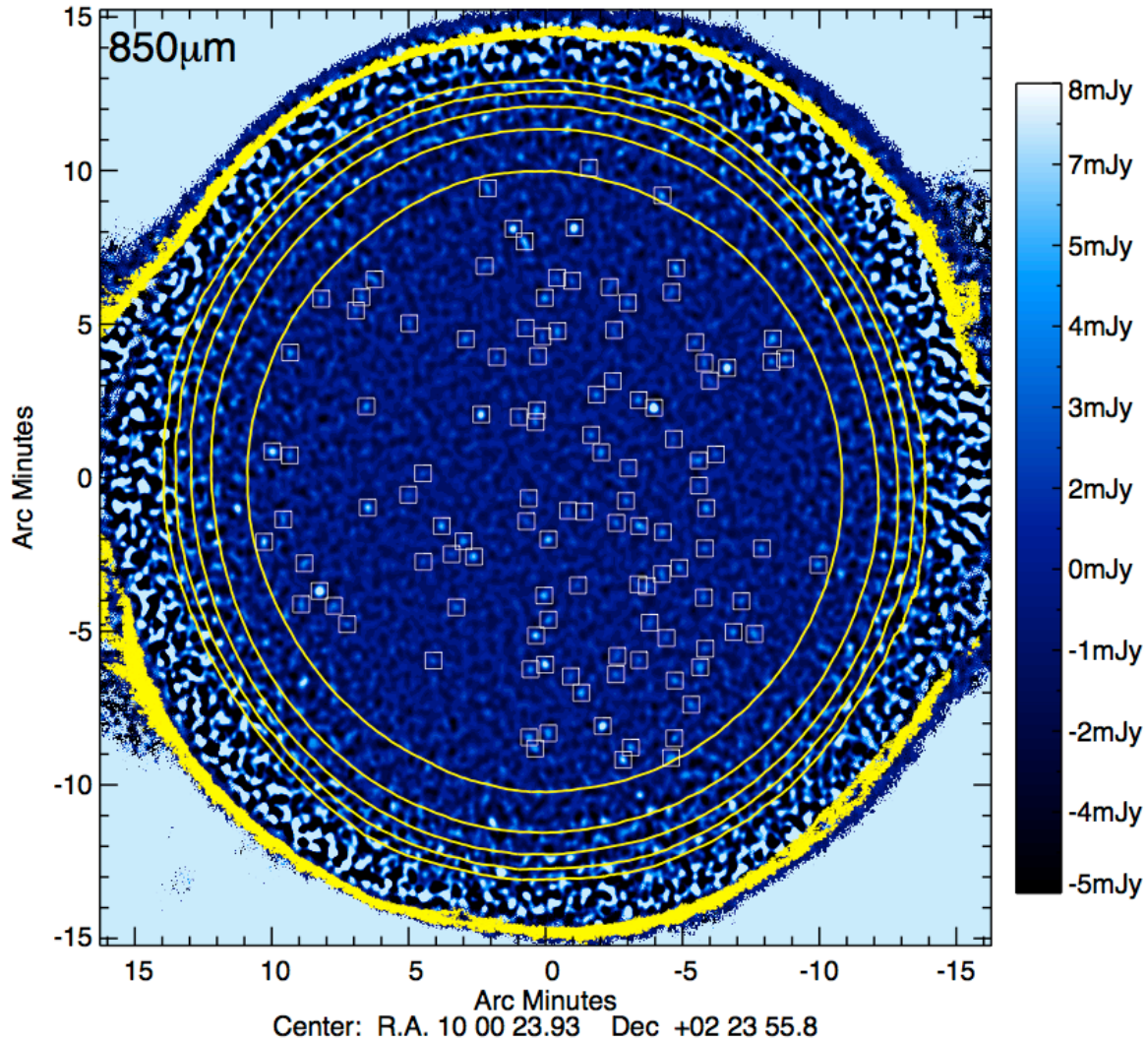


Figure 3. The COSMOS 850 μm SCUBA-2 map, plotted in the same fashion as Figure 2. The colour scale is linear and runs from $-5 < S_{850} < 8 \text{ mJy/beam}$, and the measured central RMS is 0.80 mJy/beam. All $>3.6\sigma$ sources are marked with white boxes. Some sources appear outside the nominal $2\times\text{RMS}$ contour, but locally have noise that dips below the $2\times\text{RMS}$ threshold.

arrays at 450 μm and 850 μm were combined for each night’s worth of data, and then the nights were combined to produce the unprocessed, raw maps at 450 μm and 850 μm in units of pW.

We applied the matched-filter PICARD recipe to suppress pattern noise and increase the signal from individual sources, which are generally unresolved. At 450 μm , the map RMS noise drops substantially from 14.08 mJy to 4.13 mJy. A similar yet less dramatic drop is seen at 850 μm , from 2.18 mJy to 0.80 mJy. Flux calibration is done by applying the measured flux conversion factors (FCF) from the first eight months of calibrator data, primarily from Uranus and Mars ($\text{FCF}_{850} = 556 \pm 45 \text{ Jy pW}^{-1} \text{ beam}^{-1}$ and $\text{FCF}_{450} = 606 \pm 55 \text{ Jy pW}^{-1} \text{ beam}^{-1}$). These flux conversions differ from the current canonical values (Dempsey et al. 2013) because we used an earlier version of PICARD. Calibration data taken during the observations for this project agree with these FCF values to $\sim 10\%$. Final reduced maps, in units of mJy/beam, are shown in Figures 2

and 3. The units are such that the flux density, in mJy, for an unresolved source is simply the sources’ peak value in the map. Signal-to-noise maps are constructed using the PICARD recipe MAKESNR; these are not shown here but are quite similar to the final reduced maps within the central area. We found no evidence for a systematic astrometric offset necessary after inspection of the radio data described in the next section (following the astrometric calibration procedure of Chen et al. 2013). Signal-to-noise maps are used for the identification of point sources.

To avoid contamination from the less sensitive edges of the map in calculating an overall characteristic map noise, we first measured the effective area of the sensitive region of the map, where the RMS was less than or equal to a factor of two times the RMS in the centre. We determined this boundary by measuring the RMS in concentric annuli 5'' wide from a jackknife map, having subtracted out the signal from point sources. The jackknife map represents the instrumental noise of our observations with sources removed

and is constructed by subtracting one half of our data from the other, then scaling the noise by the square root of the integration time. This $2\times$ RMS boundary lies $\sim 11.2'$ from the map centre in both the $450\mu\text{m}$ and $850\mu\text{m}$ maps, corresponding to an area of 394 arcmin^2 , slightly larger than the anticipated $15'\times 15'$ PONG-900 target area.

The pixel flux distributions for the $\sim 400\text{ arcmin}^2$ central region are shown in Figure 4 with the distributions of the jackknife pure-noise maps, in the same $\sim 400\text{ arcmin}^2$ area, highlighted in gray. The positive excess above the jackknife noise map is attributed to the detection of real sources. The negative flux excesses (prominent at $850\mu\text{m}$) is due to troughs around high-S/N sources and is a characteristic of the removal of pattern noise and is exaggerated by the matched-filter technique. In other words, in order to boost the signal in real sources, especially at S/N ratios >5 , matched-filter creates rings or troughs of negative flux surrounding the source. Since there are 44 $850\mu\text{m}$ sources at S/N >5 and only 8 $450\mu\text{m}$ sources at S/N >5 , the effect of a negative excess is more pronounced at $850\mu\text{m}$.

2.1 COSMOS Ancillary Data

We use the vast ancillary data available in the COSMOS field (Scoville et al. 2007) to investigate the physical nature of the SCUBA-2 submillimeter-bright sources and compare with larger samples of submillimeter sources previously analysed in the literature. The imaging and associated data reduction for *Spitzer Space Telescope* IRAC and MIPS data is described in Sanders et al. (2007), Le Floch et al. (2009) and Frayer et al. (2009).

Photometric redshifts were fit using the LE PHARE¹ code (Ilbert et al. 2009, 2010) to multi-band ultraviolet, optical, near-infrared (NIR) and mid-infrared (MIR) photometry. Stellar population templates (Polletta et al. 2007; Bruzual & Charlot 2003) were assumed as input to *Le Phare*. Extinction is a free parameter of the fit and is given a maximum value of $E(B-V) = 0.5$, where galaxies redder than Sb have no extinction (i.e. assuming older stellar populations rather than dustier systems). Not allowing a wider range of extinctions could impact the quality of photometric redshifts in our sample, despite the fact that 30+ photometric bands are used to measure redshift; this is an issue we will investigate in a future work.

In this paper we quote the measured LE PHARE output parameters of stellar mass and star formation rate from the (Ilbert et al. 2009) catalogue for contrast. Both are measured from stellar template matching to UV/optical/near-infrared photometry only, and in this paper, we refer to the template star formation rate as “SFR_{UV}.” While this SED fitting method is widely used for large, catalogue-based approaches to galaxy characterisation, we note that it differs from the method of using the ultraviolet slope, β , for measuring dust attenuation (and therefore dust-corrected total star formation rates). The latter method is used by Meurer et al. (1999) and Reddy et al. (2012), among others, and

is shown to more accurately predict dust attenuation in luminous infrared galaxies. We discuss the contrasting SFR measures later in section 5.2.

3 IDENTIFICATION OF POINT SOURCES

Point sources are extracted in each map by isolating high signal-to-noise pixel groups (e.g. adjacent pixels) in the signal-to-noise maps. Within each pixel group, the highest signal-to-noise pixel marks the object centre and point at which the raw flux density is measured. The raw flux densities are measured as the peak flux density of the source in mJy/beam, assuming the sources are unresolved (a safe assumption for high-redshift infrared galaxies).

Here we describe our use of Monte Carlo simulations to determine an appropriate detection threshold for reporting detections, and for measuring number counts, boosting factors and completeness and contamination rates.

3.1 Monte Carlo Simulations

The estimation of cumulative number counts at both $450\mu\text{m}$ and $850\mu\text{m}$, along with the completeness and contamination rates of our samples, deboosting factors, and adequate detection thresholds requires the use of Monte Carlo simulations. This is an iterative process which sheds light on the observational impact and limitations on the true number counts (see Coppin et al. 2005, for a thorough description of the process). Monte Carlo testing is done by injecting fake sources into a pure-noise, or jackknife, map. Injecting sources into our map with known flux densities and positions, we can measure the accuracy by which we recover those sources using the above extraction method.

Injecting fake sources into a noise map requires an *a priori* assumption of intrinsic number counts; at $450\mu\text{m}$, we vary the fit parameters from Chen et al. (2013) and Geach et al. (2013), which use a double-power law and Schechter form respectively until our measured raw number counts match those found in our Monte Carlo simulations. At $850\mu\text{m}$, we vary the parameters around those used in Knudsen et al. (2008). We use the Knudsen et al. initial variables to take advantage of data at the faintest flux densities (which are in agreement with previous blank-field number counts work Coppin et al. 2006). To generate substantial statistical samples of input and extracted sources, we generate 200 maps at both wavelengths (which generates $\sim 10,000$ extracted sources). Boosting, positional offset, completeness and contamination are all estimated using the known input sample, position and flux density, and the measured output sample, position, flux density and signal-to-noise.

The flux densities of sources we measure from our maps need correction for flux boosting. Sources’ flux densities are expected to be boosted from both Eddington boosting (Eddington 1913) and confusion boosting. We have estimated the magnitude of these two boosting factors together using our simulations results, which we show as a function of detection S/N in the top panels of Figure 5. Figure 5 also shows the median positional offset between the measured output position of a $450\mu\text{m}$ - or $850\mu\text{m}$ - source and its input position in the bottom panels (a maximum search radius of

¹ http://www.cfht.hawaii.edu/~arnouts/LEPHARE/cfht_lephare/lephare.html

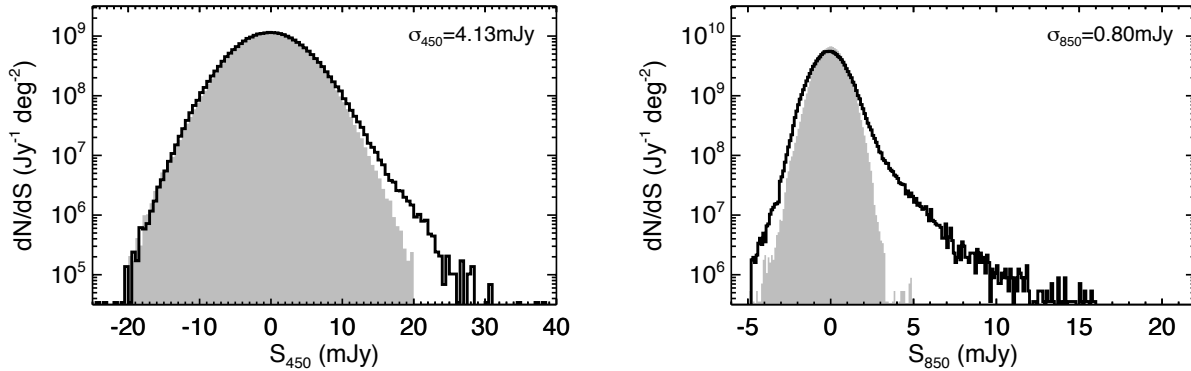


Figure 4. Pixel flux distributions (per unit area) within the central ~ 400 arcmin² area at $450\mu\text{m}$ and $850\mu\text{m}$. The solid black lines indicate the distributions of the data, showing excesses at high flux densities where point sources contribute to the distributions. At lower flux densities, the distributions are dominated by instrument noise. The negative excesses are due to residual troughs around bright sources (a characteristic of the matched filter technique). The gray shaded histograms show the pixel noise distributions within the same region for the jackknife maps. As discussed in the text, the jackknife maps were constructed by differencing two halves of the data, which removes point sources and leaves only residual noise.

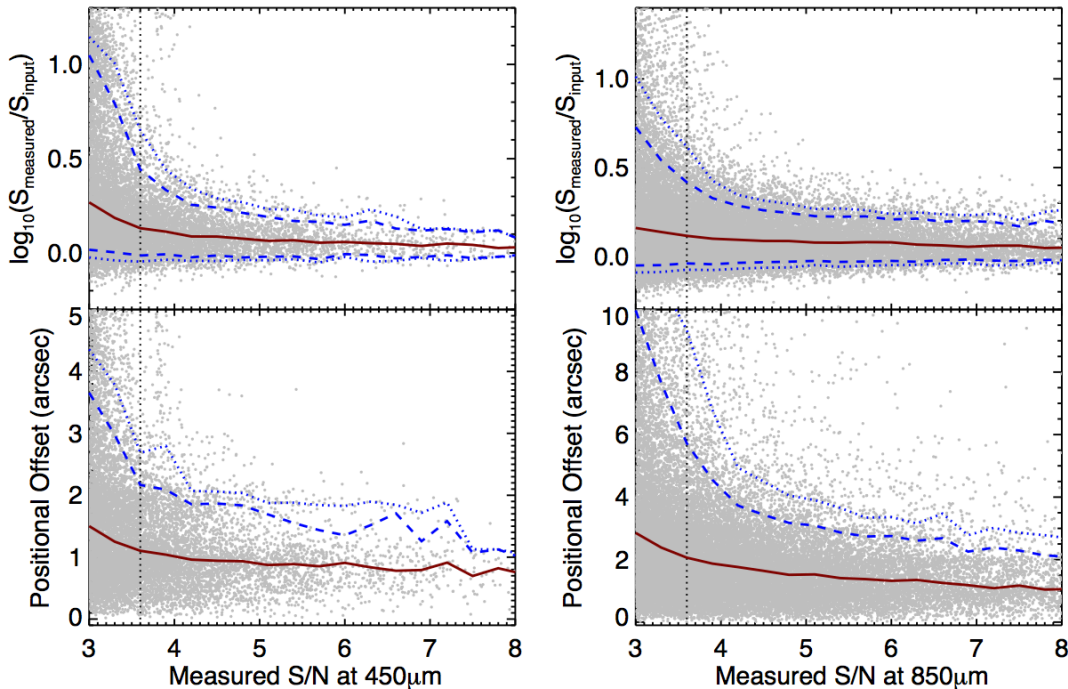


Figure 5. Our results from Monte Carlo simulations, showing more than 10000 source realisations and the measured boosting factor and positional offset for each source (gray points) at $450\mu\text{m}$ (left) and $850\mu\text{m}$ (right). The boosting factor is measured as the ratio of output measured flux density over input flux density. We deboost our sources' flux densities using the median boosting factors (red lines). The 90% confidence intervals (dashed blue lines) and 95% confidence intervals (dotted blue lines) are overplotted. We assign a positional uncertainty to sources according to the 90% confidence interval. The 3.6σ signal-to-noise threshold is marked by dotted vertical lines.

of $7''$ and $14''$ were used, respectively). The positional uncertainty quoted in Tables 1 and 5 is the 90% confidence interval, which we then use for matching to radio, $24\mu\text{m}$, and optical counterparts as described in sections 3.4. Higher signal-to-noise detections can yield very small positional uncertainties.

Before measuring the cumulative number counts or de-

termining on an appropriate S/N detection threshold, it is essential to understand our sample's completeness and contamination rate. Completeness deteriorates at low flux densities. We estimate completeness from our Monte Carlo simulations as the fraction of sources recovered $>3\sigma$ or $>4\sigma$ in our simulated maps and is shown in Figure 6. As is expected, a more conservative (4σ) cut on the sample results in a more

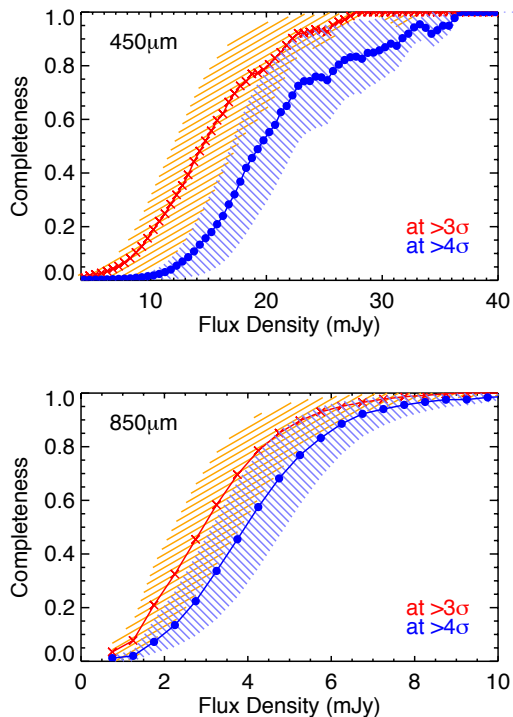


Figure 6. The completeness curves at $450\mu\text{m}$ and $850\mu\text{m}$. Completeness is measured as a function of input flux density as the number of sources in a given flux bin which are recovered at the signal-to-noise threshold (3σ and 4σ are plotted here). The uncertainty on the completeness curve is generated from a bimodal uncertainty.

incomplete sample at moderate flux densities than a more liberal cut (3σ). We will take these completeness curves into consideration with the calculation of the cumulative number counts.

Deciding on an appropriate detection threshold requires an understanding of our sample’s contaminants. We measure contamination rate as a function of detection signal-to-noise. At a given detection S/N, the contaminating fraction is the number of sources which are generated by fluctuations in the map due to noise or from sources well below the nominal detection limit. Since our maps are roughly uniform, we fix this limiting flux density at the lowest deboosted flux density of our 3σ sample. Any source with input flux density below this threshold would not be expected to be measured in our data even after Eddington and confusion boosting, so here is considered a contaminant. The contamination rate as a function of both flux density and signal-to-noise is shown in Figure 7.

Figure 7 tells us the probability that a given source with a given signal-to-noise ratio is spurious. Accordingly, we are able to assign a “probability of contamination” (p_{contam}) for each source. We use this source-by-source probability to estimate total contamination rates for samples defined by different signal-to-noise detection thresholds. In a sample sized N , the probability of having no contaminants is equal to $\prod_{i=1}^N (1 - p_i)$, the probability of having one contaminant

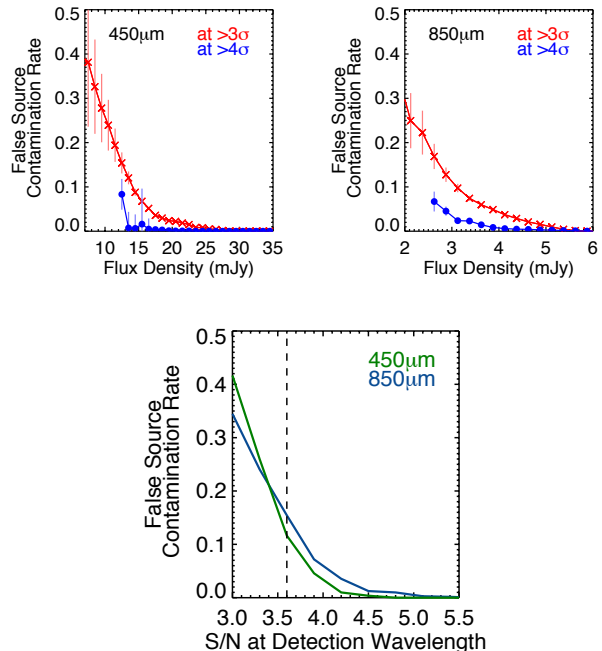


Figure 7. The contamination rates at $450\mu\text{m}$ and $850\mu\text{m}$ as a function of flux density (top two panels) and signal-to-noise (bottom panel). The contamination rate is computed as the number of sources which are extracted from Monte Carlo simulations which are (a) truly spurious, caused by noise fluctuations, or (b) at flux densities lower than the nominal 3σ detection limit, after correction for deboosting. The sharp upturn in contamination at $\sim 12\text{mJy}$ at $450\mu\text{m}$ is due to small number counts in our simulations (despite $>10\text{K}$ realisations, there are very few $>4\sigma$ sources at $\sim 12\text{mJy}$). We use the measured contamination rate curves in the bottom panel, as a function of signal-to-noise, to infer the likelihood that a source of a given signal-to-noise is a contaminant. We plot our final signal-to-noise threshold of 3.6σ on the bottom panel, which shows that the maximum individual source contamination likelihood is $\sim 15\%$ in both $450\mu\text{m}$ (green) and $850\mu\text{m}$ (blue) samples.

is equal to $\sum_{i=1}^N p_i \prod_{k \neq i}^N (1 - p_k)$, and so on. For example, there are 37 sources in a 4σ cut in our $450\mu\text{m}$ map. We estimate that the 4σ sample has a 76% likelihood of having *no* contaminants, and a 97% chance of having a contamination rate of $<3\%$. This cut is quite conservative, so we push the detection threshold lower until we estimate contamination rates of 3–5%. This is our target contamination rate since it is low enough not to significantly impact the global properties of the sample, while it allows for a far larger sample size strengthening the analysis of the population. At both $450\mu\text{m}$ and $850\mu\text{m}$, we estimate that a 3.6σ detection threshold will yield a 3–5% contamination rate. As is seen in Figure 7, these limits correspond to similar ‘worst’ individual source contamination rates of ~ 0.14 at $450\mu\text{m}$ and ~ 0.17 at $850\mu\text{m}$ (i.e. the lowest S/N sources in the 3.6σ samples have a ~ 14 or 17% likelihood of being spurious).

Table 1. 450 μm -identified $>3.6\sigma$ point sources in COSMOS.

Name	Short Name	RA ₄₅₀	DEC ₄₅₀	S/N	S ₄₅₀ RAW [mJy]	S ₄₅₀ DEBOOSTED [mJy]	$\Delta(\alpha,\delta)$ [$''$]	P_{contam}	850 μm - SOURCE	Offset [$''$]	S ₈₅₀ RAW [mJy]	S ₈₅₀ DEBOOSTED [mJy]
SMM J100028.6+023201...	450.00	10:00:28.6	02:32:01	7.80	40.58 \pm 5.20	37.54 \pm 6.58	1.06	<0.01	850.07	0.6	9.94 \pm 1.06	9.21 \pm 1.45
SMM J100033.3+022559...	450.01	10:00:33.3	02:25:59	6.89	28.43 \pm 4.13	25.62 \pm 4.96	1.51	<0.01	850.02	0.6	9.47 \pm 0.80	8.22 \pm 0.70
SMM J100109.0+022255...	450.02	10:01:09.0	02:22:55	6.15	47.20 \pm 7.68	41.70 \pm 9.00	1.48	<0.01			9.67 \pm 1.71	
SMM J100008.0+022611...	450.03	10:00:08.0	02:26:11	5.73	23.47 \pm 4.10	20.46 \pm 4.78	1.45	<0.01	850.00	0.6	16.15 \pm 0.80	10.86 \pm 0.54
SMM J100019.7+023205...	450.04	10:00:19.7	02:32:05	5.62	29.15 \pm 5.19	25.35 \pm 6.04	1.48	<0.01	850.03	1.5	12.11 \pm 1.03	10.54 \pm 0.90
SMM J100023.6+022156...	450.05	10:00:23.6	02:21:56	5.62	23.14 \pm 4.12	20.12 \pm 4.80	1.48	<0.01	850.08	1.9	7.19 \pm 0.80	6.60 \pm 1.12
SMM J100039.2+022221...	450.06	10:00:39.2	02:22:21	5.43	22.29 \pm 4.11	19.32 \pm 4.76	1.55	<0.01	850.12	1.3	6.49 \pm 0.80	5.83 \pm 1.13
SMM J100014.2+023017...	450.07	10:00:14.2	02:30:17	5.32	23.94 \pm 4.50	20.65 \pm 5.19	1.59	<0.01			2.64 \pm 0.89	
SMM J100025.1+021508...	450.08	10:00:25.1	02:15:08	5.15	31.25 \pm 6.06	26.71 \pm 6.93	1.67	<0.01	(850.46)		4.27 \pm 1.15	
SMM J100016.6+022637...	450.09	10:00:16.6	02:26:37	4.94	20.41 \pm 4.14	17.26 \pm 4.68	1.75	<0.01	850.34	2.3	4.41 \pm 0.80	3.68 \pm 1.01
SMM J100022.2+022354...	450.10	10:00:22.2	02:23:54	4.85	20.09 \pm 4.14	16.91 \pm 4.67	1.78	<0.01	850.135	5.5	2.60 \pm 0.80	1.87 \pm 1.01
SMM J100025.4+022542...	450.11	10:00:25.4	02:25:42	4.77	19.57 \pm 4.11	16.40 \pm 4.62	1.80	<0.01	850.41	2.0	4.12 \pm 0.80	3.43 \pm 0.98
SMM J095957.0+022153...	450.12	09:59:57.0	02:21:53	4.76	22.03 \pm 4.63	18.45 \pm 5.21	1.81	<0.01			1.71 \pm 0.89	
SMM J100001.7+022426...	450.13	10:00:01.7	02:24:26	4.75	19.96 \pm 4.20	16.72 \pm 4.73	1.81	<0.01	(850.32)		3.81 \pm 0.82	
SMM J100044.9+021919...	450.14	10:00:44.9	02:19:19	4.74	21.73 \pm 4.59	18.18 \pm 5.17	1.81	<0.01			1.28 \pm 0.91	
SMM J100004.2+022059...	450.15	10:00:04.2	02:20:59	4.60	19.92 \pm 4.33	16.53 \pm 4.88	1.83	<0.01	850.28	1.8	4.86 \pm 0.84	4.07 \pm 1.08
SMM J100057.2+022009...	450.16	10:00:57.2	02:20:09	4.59	25.18 \pm 5.48	20.89 \pm 6.19	1.84	<0.01	(850.05)		8.99 \pm 1.14	
SMM J100017.2+022521...	450.17	10:00:17.2	02:25:21	4.59	19.01 \pm 4.14	15.76 \pm 4.67	1.84	<0.01	850.42	2.6	4.12 \pm 0.80	3.43 \pm 0.99
SMM J100007.2+021803...	450.18	10:00:07.2	02:18:03	4.49	22.63 \pm 5.04	18.66 \pm 5.68	1.85	<0.01			-0.76 \pm 0.95	
SMM J095948.1+022014...	450.19	09:59:48.1	02:20:14	4.47	28.25 \pm 6.33	23.24 \pm 7.14	1.86	<0.01			0.77 \pm 1.16	
SMM J100004.5+023042...	450.20	10:00:04.5	02:30:42	4.44	23.28 \pm 5.24	19.11 \pm 5.91	1.87	<0.01	(850.24)		4.62 \pm 1.01	
SMM J100017.2+022138...	450.21	10:00:17.2	02:21:38	4.40	18.14 \pm 4.12	14.83 \pm 4.64	1.88	<0.01			0.72 \pm 0.80	
SMM J100030.8+023104...	450.22	10:00:30.8	02:31:04	4.34	21.10 \pm 4.86	17.15 \pm 5.47	1.90	<0.01	850.149	4.1	3.04 \pm 0.96	2.16 \pm 1.21
SMM J100004.6+021820...	450.23	10:00:04.6	02:18:20	4.33	21.95 \pm 5.07	17.81 \pm 5.71	1.90	<0.01			-0.36 \pm 0.96	
SMM J100050.1+022116...	450.24	10:00:50.1	02:21:16	4.30	19.72 \pm 4.58	15.97 \pm 5.16	1.91	<0.01			1.29 \pm 0.91	
SMM J100028.5+021927...	450.25	10:00:28.5	02:19:27	4.30	18.04 \pm 4.20	14.60 \pm 4.73	1.91	<0.01			-0.82 \pm 0.82	
SMM J100016.6+022000...	450.26	10:00:16.6	02:20:00	4.27	17.81 \pm 4.17	14.38 \pm 4.69	1.92	<0.01			-0.60 \pm 0.81	
SMM J095942.9+022144...	450.27	09:59:42.9	02:21:44	4.26	29.66 \pm 6.97	23.91 \pm 7.84	1.92	<0.01	850.115	7.3	4.26 \pm 1.26	3.14 \pm 1.56
SMM J100056.7+022014...	450.28	10:00:56.7	02:20:14	4.24	22.76 \pm 5.37	18.32 \pm 6.04	1.93	<0.01	(850.05)		10.85 \pm 1.12	
SMM J100000.5+022503...	450.29	10:00:00.5	02:25:03	4.22	18.01 \pm 4.27	14.46 \pm 4.80	1.93	<0.01			0.94 \pm 0.83	
SMM J100048.3+022926...	450.30	10:00:48.3	02:29:26	4.16	20.99 \pm 5.05	16.76 \pm 5.69	1.95	<0.01			2.23 \pm 1.04	
SMM J100008.4+022241...	450.31	10:00:08.4	02:22:41	4.11	16.96 \pm 4.13	13.46 \pm 4.69	1.97	0.02			1.17 \pm 0.80	
SMM J100010.2+022624...	450.32	10:00:10.2	02:26:24	4.10	16.86 \pm 4.11	13.37 \pm 4.67	1.97	0.02	850.26	3.0	4.87 \pm 0.80	4.12 \pm 1.06
SMM J100021.3+023055...	450.33	10:00:21.3	02:30:55	4.04	18.93 \pm 4.69	14.90 \pm 5.36	1.99	0.03			0.59 \pm 0.93	
SMM J095945.2+022553...	450.34	09:59:45.2	02:25:53	4.04	24.73 \pm 6.13	19.46 \pm 7.01	1.99	0.03			3.30 \pm 1.13	
SMM J100014.4+021706...	450.35	10:00:14.4	02:17:06	4.04	20.52 \pm 5.12	16.10 \pm 5.87	2.00	0.03			-0.55 \pm 0.97	
SMM J100101.0+022800...	450.36	10:01:01.0	02:28:00	4.00	24.27 \pm 6.07	19.03 \pm 6.96	2.00	0.03	850.58	3.8	5.67 \pm 1.31	4.60 \pm 1.57
SMM J100001.5+021939...	450.37	10:00:01.5	02:19:39	4.00	19.20 \pm 4.80	15.05 \pm 5.51	2.00	0.03			-0.98 \pm 0.91	
SMM J100010.3+022223...	450.38	10:00:10.3	02:22:23	4.00	16.47 \pm 4.12	12.91 \pm 4.73	2.01	0.03	850.14	2.8	6.25 \pm 0.80	5.55 \pm 1.11
SMM J100011.2+021554...	450.39	10:00:11.2	02:15:54	3.99	23.76 \pm 5.96	18.60 \pm 6.84	2.01	0.04			-0.70 \pm 1.11	
SMM J100033.1+023046...	450.40	10:00:33.1	02:30:46	3.98	19.15 \pm 4.81	14.98 \pm 5.53	2.01	0.04	850.90	5.0	3.52 \pm 0.96	2.71 \pm 1.16
SMM J100006.6+021527...	450.41	10:00:06.6	02:15:27	3.96	26.42 \pm 6.67	20.62 \pm 7.67	2.02	0.04			1.39 \pm 1.25	
SMM J100036.9+021938...	450.42	10:00:36.9	02:19:38	3.94	16.71 \pm 4.24	13.01 \pm 4.89	2.02	0.04	850.48	3.6	3.99 \pm 0.83	3.30 \pm 1.00
SMM J100028.8+023336...	450.43	10:00:28.8	02:33:36	3.88	24.62 \pm 6.34	19.00 \pm 7.36	2.06	0.05			1.62 \pm 1.28	
SMM J100054.5+021919...	450.44	10:00:54.5	02:19:19	3.88	20.99 \pm 5.41	16.18 \pm 6.28	2.06	0.05			-0.15 \pm 1.12	
SMM J100056.1+021831...	450.45	10:00:56.1	02:18:31	3.82	23.57 \pm 6.16	17.92 \pm 7.22	2.13	0.06			-1.21 \pm 1.30	
SMM J100032.4+022148...	450.46	10:00:32.4	02:21:48	3.81	15.72 \pm 4.13	11.90 \pm 4.86	2.16	0.07			0.11 \pm 0.80	
SMM J100025.2+021930...	450.47	10:00:25.2	02:19:30	3.80	15.90 \pm 4.18	12.03 \pm 4.91	2.16	0.07			1.60 \pm 0.81	
SMM J100009.4+022223...	450.48	10:00:09.4	02:22:23	3.80	15.72 \pm 4.13	11.89 \pm 4.86	2.16	0.07			2.73 \pm 0.80	
SMM J100000.0+022524...	450.49	10:00:00.0	02:25:24	3.79	16.29 \pm 4.30	12.27 \pm 5.07	2.18	0.07			-0.72 \pm 0.84	
SMM J095952.2+022133...	450.50	09:59:52.2	02:21:33	3.78	19.82 \pm 5.25	14.90 \pm 6.19	2.19	0.07	850.47	3.6	4.74 \pm 0.98	3.92 \pm 1.19
SMM J100044.3+022313...	450.51	10:00:44.3	02:23:13	3.77	15.64 \pm 4.15	11.74 \pm 4.90	2.20	0.08			1.27 \pm 0.81	
SMM J100007.8+022306...	450.52	10:00:07.8	02:23:06	3.77	15.57 \pm 4.13	11.68 \pm 4.88	2.20	0.08			-0.46 \pm 0.80	
SMM J100010.4+022026...	450.53	10:00:10.4	02:20:26	3.74	15.69 \pm 4.19	11.69 \pm 4.97	2.23	0.08	850.109	0.6	2.84 \pm 0.82	2.13 \pm 1.00
SMM J100026.8+022318...	450.54	10:00:26.8	02:23:18	3.74	15.46 \pm 4.13	11.51 \pm 4.90	2.23	0.08	850.96	8.1	2.93 \pm 0.80	2.24 \pm 0.97
SMM J100023.8+021751...	450.55	10:00:23.8	02:17:51	3.74	17.06 \pm 4.57	12.70 \pm 5.42	2.24	0.08	850.06	3.1	9.30 \pm 0.89	8.42 \pm 0.92
SMM J095959.3+023000...	450.56	09:59:59.3	02:30:00	3.73	20.17 \pm 5.40	14.98 \pm 6.42	2.25	0.09			-0.89 \pm 1.03	
SMM J100032.4+021802...	450.57	10:00:32.4	02:18:02	3.73	16.75 \pm 4.49	12.44 \pm 5.34	2.25	0.09			0.56 \pm 0.88	
SMM J100036.1+022152...	450.58	10:00:36.1	02:21:52	3.72	15.32 \pm 4.12	11.35 \pm 4.90	2.26	0.09	850.21	3.6	5.29 \pm 0.80	4.60 \pm 1.08
SMM J100019.4+022024...	450.59	10:00:19.4	02:20:24	3.71	15.33 \pm 4.13	11.33 \pm 4.92	2.27	0.09	850.101	3.3	2.87 \pm 0.80	2.19 \pm 0.98
SMM J100008.1+023059...	450.60	10:00:08.1	02:30:59	3.71	18.82 \pm 5.07	13.90 \pm 6.04	2.27	0.09			1.81 \pm 0.99	
SMM J100018.7+022813...	450.61	10:00:18.7	02:28:13	3.70	15.48 \pm 4.18	11.42 \pm 4.98	2.28	0.09			1.24 \pm 0.81	
SMM J100047.3+022049...	450.62	10:00:47.3	02:20:49	3.70	16.48 \pm 4.45	12.15 \pm 5.30	2.28	0.09			-0.18 \pm 0.89	
SMM J100020.0+022129...	450.63	10:00:20.0	02:21:29	3.70	15.23 \pm 4.12	11.23 \pm 4.90	2.29	0.09			0.05 \pm 0.80	
SMM J100010.7+022707...	450.64	10:00:10.7	02:27:07	3.68	15.18 \pm 4.12	11.14 \pm 4.91	2.31	0.10			0.86 \pm 0.80	
SMM J100027.2+022448...	450.65	10:00:27.2	02:24:48	3.68	15.13 \pm 4.12	11.08 \pm 4.92	2.32	0.10			0.00 \pm 0.80	
SMM J100104.6+022633...	450.66	10:01:04.6	02:26:33	3.66	23.50 \pm 6.42	17.15 \pm 7.68	2.34	0.10	850.146	4.1	4.29 \pm 1.36	3.06 \pm 1.70
SMM J100000.												

of each individual source according to its detection signal-to-noise ratio. The uncertainty in the deboosting factor is propagated to the new uncertainty in the sources' deboosted flux density. As a result, the sources' ratio of deboosted flux density to its uncertainty is lower than the sources' measured signal-to-noise ratios. The net effect of deboosting is a shift towards lower flux densities (in the x -direction on the number counts plot), seen in the middle panels of Figure 8.

The final effect which needs to be accounted for in our computation of the cumulative number counts is incompleteness and contamination in our samples. As shown in Figure 6 and Figure 7, our samples are not complete down to our nominal ~ 15 mJy $\approx 3.6\sigma_{450}$ or ~ 2.9 mJy $\approx 3.6\sigma_{850}$ detection threshold. Furthermore, 3–5% of our sources are likely contaminants. To correct for sources missing and contaminant sources we construct a correction factor, c_i , for each source, based on its flux density and signal-to-noise, such that $c_i = (1 - f_{\text{contam}})/f_{\text{complete}}$. We correct the number counts accordingly. Not surprisingly, this correction for incompleteness and contamination has an effect on the low flux density bins and a minimal effect on the high flux density bins. Our deboosted and corrected number counts are given in Table 2.

In functional form, we can assume that the differential number counts follow a few different forms. The types we adopt in this paper are a broken double power law (as most recently used in Chen et al. 2013), taking the form:

$$\frac{dN}{dS} = \begin{cases} \frac{N_0}{S_0} \left(\frac{S}{S_0}\right)^{-\alpha} & : S \leq S_0 \\ \frac{N_0}{S_0} \left(\frac{S}{S_0}\right)^{-\beta} & : S > S_0 \end{cases} \quad (1)$$

where S_0 represents the turnover flux density, N_0 a normalisation for the function in source density per mJy, α is the faint end slope and β is the bright end slope (presumed to be steeper). Alternatively we can assume the number counts follow a Schechter function, as used in Geach et al. (2013)²:

$$\frac{dN}{dS} = \frac{N_0}{S_0} \left(\frac{S}{S_0}\right)^{-\alpha} e^{-\left(\frac{S}{S_0}\right)} \quad (2)$$

We perform a χ^2 optimisation to determine best-fit parameter values at 450 μ m and 850 μ m respectively in equations 1 and 2, which are given in Table 2. These best-fit parameter values are tested for consistency with the Monte Carlo simulations; in other words, we adjust the fit parameters, populate the jackknife maps accordingly, then extract sources and re-measure the raw number counts. The parameters which reproduce the raw number counts most accurately are used in the Monte Carlo tests for boosting factor, positional uncertainty and estimating contamination and completeness rates, as given in the previous section. Once we arrive at the *corrected* number counts, we then remeasure our best-fit parameters with a χ^2 test which agrees with our initial injected counts within uncertainty. We find the power-law fit produces a better fit than a Schechter fit to both datasets

² Note that Equation 1 of Geach et al. should be written $dN/dS = (N'/S')(S/S')^{1-\alpha} \exp(-S/S')$, and the best-fit parameter N' from their paper should be quoted as $N' = 4900 \pm 1040 \text{ deg}^{-2} \text{ mJy}^{-1}$ rather than $N' = 490 \pm 104 \text{ deg}^{-2}$. Also note we use an exponent of $-\alpha$ instead of $1 - \alpha$. By our equation, the parameters of the Geach et al. data are: $N_0 = 4900 \text{ deg}^{-2} \text{ mJy}^{-1}$, $S_0 = 10 \text{ mJy}$, and $\alpha = 2.0$.

Table 2. True Number Counts at 450 μ m, 850 μ m, and best-fit double power-law/Schechter function parameters.

450 μ m-Number Counts				850 μ m-Number Counts			
S_{450}	N	dN/dS	N(> S)	S_{850}	N	dN/dS	N(> S)
(mJy)		(mJy ⁻¹ deg ⁻²)	(deg ⁻²)	(mJy)		(mJy ⁻¹ deg ⁻²)	(deg ⁻²)
10.59	15	154 ⁺⁵¹ ₋₃₈	1430 ⁺³⁷⁰ ₋₂₉₀	2.65	20	579 ⁺¹⁵⁷ ₋₁₂₄	1040 ⁺³⁰⁰ ₋₂₃₀
14.13	27	129 ⁺³¹ ₋₂₅	679 ⁺¹⁷⁵ ₋₁₃₉	3.37	23	412 ⁺¹⁰⁴ ₋₈₃	719 ⁺¹⁸⁹ ₋₁₅₀
18.84	29	66.1 ^{+15.0} _{-12.2}	215 ⁺⁸⁸ ₋₆₂	4.29	27	306 ⁺⁷⁰ ₋₅₇	380 ⁺¹²⁷ ₋₉₅
25.12	5	6.87 ^{+4.13} _{-2.58}	48 ⁺⁵² ₋₂₅	5.46	19	78.2 ^{+31.0} _{-22.2}	185 ⁺⁸⁸ ₋₆₀
33.50	1	0.97 ^{+1.80} _{-0.63}	18 ⁺³² ₋₁₂	6.96	7	40.4 ^{+19.7} _{-13.2}	85.6 ^{+101.5} _{-46.4}
				8.86	3	13.3 ^{+11.1} _{-6.0}	66.5 ^{+66.1} _{-33.2}
				11.28	4	13.9 ^{+9.6} _{-5.7}	38.0 ^{+43.6} _{-20.3}
				14.37	1	2.7 ^{+5.1} _{-1.8}	9.5 ^{+29.6} _{-7.2}

Best-Fit Parameters to Equation 1		
	450 μ m Parameters	850 μ m Parameters
$N_0 =$	$(1.4 \pm 0.4) \times 10^3$	$(1.5 \pm 0.4) \times 10^3$
$S_0 =$	18 \pm 8	4.3 \pm 1.8
$\alpha =$	1.91 \pm 0.40	1.34 \pm 0.09
$\beta =$	5.5 \pm 1.0	4.50 \pm 0.38

Best-Fit Parameters to Equation 2		
	450 μ m Parameters	850 μ m Parameters
$N_0 =$	$(1.1 \pm 0.4) \times 10^4$	$(3.3 \pm 1.4) \times 10^3$
$S_0 =$	6.1 \pm 1.0	3.7 \pm 1.1
$\alpha =$	0.5 \pm 1.3	1.4 \pm 1.1

Table Notes. Number counts are given in differential and cumulative form. The number of sources contributing to each bin is given as the number “N.” The best-fit parameters to the number counts are given at bottom and are fit to the differential counts.

(with marginally better reduced χ^2 , 7 versus 12 at 450 μ m and 3 versus 5 at 850 μ m), so we use the double power-law Monte Carlo predictions throughout.

Noting a deficit in our 850 μ m number counts relative to many literature measurements (Smail et al. 2002; Cowie et al. 2002; Scott et al. 2002; Webb et al. 2003; Borys et al. 2003; Knudsen et al. 2008; Chen et al. 2013), we investigate the strength of this deficit. To do this we compare our best-fit double powerlaw function to the Knudsen et al. double powerlaw, integrated over the flux density range where our survey is sensitive (2.5–18 mJy). This comparison indicates that our survey is $2.1^{+1.0}_{-0.6}$ times less dense than the nominal 850 μ m source density. We also test to see if the deficit exists at 450 μ m, but we find our 450 μ m source density is consistent with the only other independent measurement at this wavelength from Chen et al. (2013).

3.3 Source Lists

The 450 μ m sources detected $>3.6\sigma$ are summarised in Table 1 and the 850 μ m sources detected at $>3.6\sigma$ are summarised in Table 5 (given at the end of the paper due to its length). Both raw and deboosted flux densities are given in the tables, along with a 90% confidence interval on positional uncertainty, $\Delta(\alpha, \delta)$, the probability of contamination or spuriousness for that source (P_{contam}), and the corresponding source detected at the opposite wavelength if it exists. The search for counterparts at the opposite wavelength is done within a radius corresponding to the sum in quadrature of the positional uncertainties, $\Delta(\alpha, \delta)$, at both 450 μ m and 850 μ m (a function of the detection S/N for each

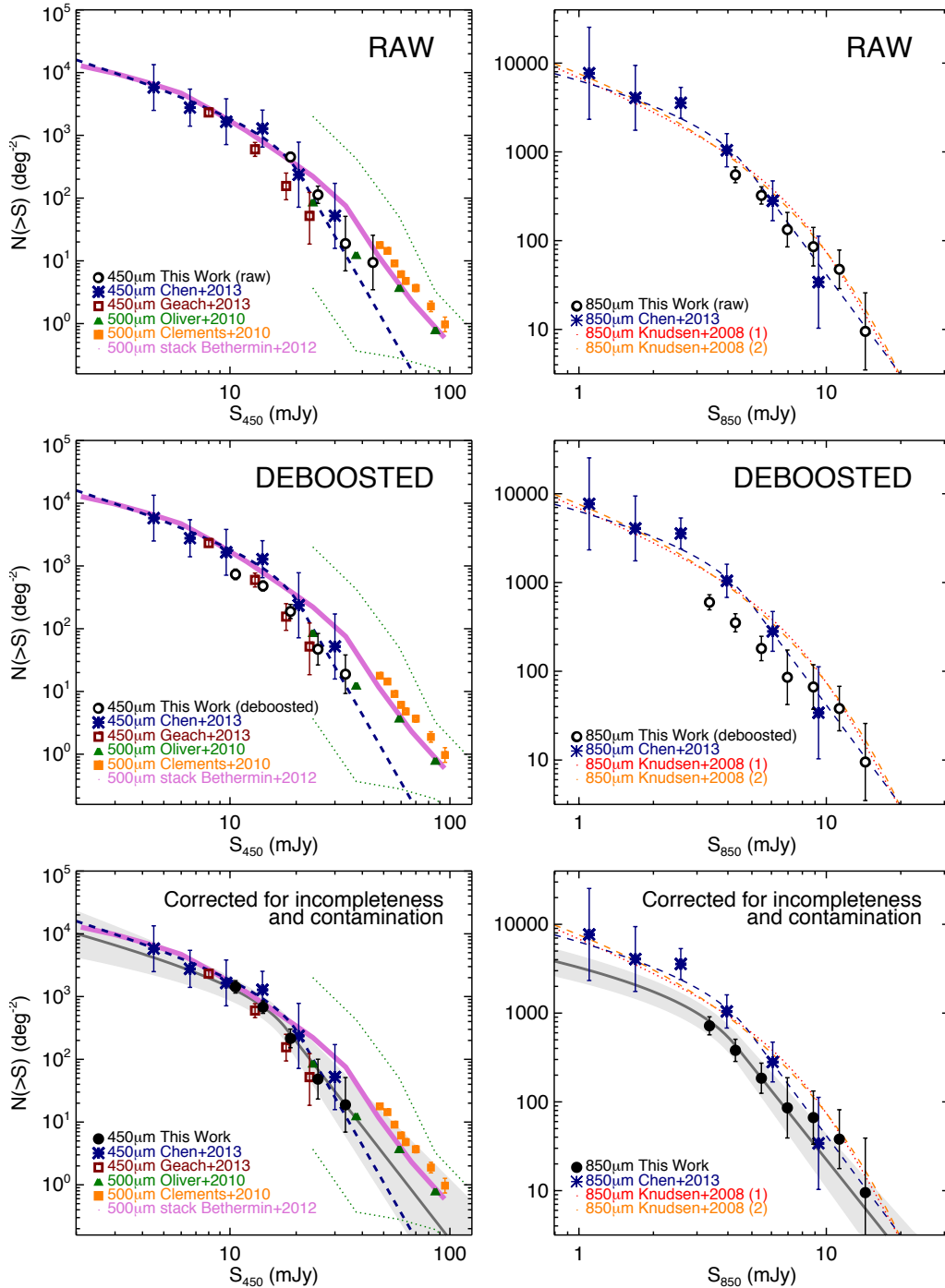


Figure 8. The cumulative number counts at $450\mu\text{m}$ (left column) and $850\mu\text{m}$ (right column) from our COSMOS data. The top row shows the raw number counts, with extracted flux densities from our map, the middle row corrects the sources' flux densities for confusion and Eddington boosting, and the bottom row corrects the deboosted number counts for incompleteness and contamination (as discussed in the text). The best-fit double power law parameterisation of the number counts are shown in gray in both bottom panels, with associated light gray uncertainties. We compare our measured counts (black open and closed circles) to those in the literature, all corrected for incompleteness and contamination. At $450\mu\text{m}$, we compare to the recent results of Chen et al. (2013) (blue asterisks, blue dashed line) and Geach et al. (2013) (red squares), and we note that the latter work is data taken in the same sky region as our COSMOS map although covering only $\sim 1/4$ the area. We also compare $450\mu\text{m}$ data to $500\mu\text{m}$ data from the *Herschel*-SPIRE instrument from Oliver et al. (2010) (green triangles) and Clements et al. (2010) (orange squares). The Bethermin et al. (2012) (pink curve) work is not from direct $500\mu\text{m}$ extractions but rather stacks on $24\mu\text{m}$ sources at $500\mu\text{m}$. At $850\mu\text{m}$, we overplot the Chen et al. (2013) results and the best-fit models from Eq. 3 & 4 in Knudsen et al. (2008) (red-orange curves), called (1) and (2) here respectively; we omit many data measurements taken at $850\mu\text{m}$ to avoid clutter on the plot.

source). If no counterpart is found, the measured flux density at the opposite wavelength is extracted at the detected source's position and quoted as a 3σ upper limit. Its flux density is not deboosted.

Of the 78 $450\mu\text{m}$ sources, 19 have $850\mu\text{m}$ counterparts detected above 3.6σ (a further 6 sources are detected at $850\mu\text{m}$ above 3σ , and 5 others are close [$<12''$] but not formally matched). Such a low fraction of $450\mu\text{m}$ corresponding to $850\mu\text{m}$ sources ($\lesssim (19-30)/78 \approx 24-38\%$) suggests that indeed, the $450\mu\text{m}$ population is intrinsically different than the $850\mu\text{m}$ population, either probing a different redshift regime, luminosity regime, or temperature regime than the $850\mu\text{m}$ population. Similarly, only 19 of 99 $850\mu\text{m}$ sources are $450\mu\text{m}$ detected $> 3.6\sigma$, with an additional 16 which are marginal $> 3\sigma$ detections and 4 nearby sources ($<12''$) which are not formally matched. This translates to a $450\mu\text{m}$ -detection rate of $850\mu\text{m}$ sources of 19–39%. We investigate the reasons for such little overlap in the next section.

Chen et al. (2013) showed that sources detected at both $450\mu\text{m}$ and $850\mu\text{m}$ at low-S/N (e.g. $3-4\sigma$) have effective S/N higher than the individual S/N in either band, in other words, that a source which is 3σ at $450\mu\text{m}$ and 3σ at $850\mu\text{m}$ is effectively a 4σ detection. We use this technique to extract $450\mu\text{m}$ sources below our nominal detection threshold. The additional $3 < \sigma < 3.6$ $450\mu\text{m}$ sources we detect with $850\mu\text{m}$ counterparts are given in Table 3. We exclude these sources from our $450\mu\text{m}$ number count computation due to the unquantified bias which requiring a $850\mu\text{m}$ counterpart enforces on the sample, but we can use this sample for comparisons to the independently-detected $>3.6\sigma$ $450\mu\text{m}$ sample in redshift, luminosity and temperature space.

3.4 Counterpart Matching

Determining the optical/near-infrared counterparts to submillimeter sources is complex, but thanks to the low positional uncertainty on our $450\mu\text{m}$ sources, it is a much more straightforward process than in other submillimeter maps. A handful of sources in our sample (five sources at $450\mu\text{m}$, eight at $850\mu\text{m}$) have interferometric observations either with the SMA (Younger et al. 2007, 2009) or the Plateau de Bure Interferometer (Smolčić et al. 2012) where the counterparts to submm observations are known, but the rest of the sample needs careful counterpart analysis. Our counterpart matching procedure at $450\mu\text{m}$ and $850\mu\text{m}$ is the same at both wavelengths, but we note that the added uncertainty at $850\mu\text{m}$ generates many more potential counterparts and is, therefore, naturally more uncertain.

All optical (i -band), near-infrared ($3.6\mu\text{m}$), $24\mu\text{m}$, and 1.4 GHz radio sources which fall within the 90% confidence positional uncertainty are considered as possible counterparts. Optical sources are taken from the Ilbert et al. catalogue, which identifies individual sources down to $i \sim 27$. Although we consider sources within the nominal positional uncertainty found by our simulations (as shown in Figure 5), additional accommodation must be made for uncertainty in the positions measured at other wavelengths or source size. Since SCUBA-2 $450\mu\text{m}$ positional uncertainties are on the order of $1-2''$, a source's size or positional uncertainty at other wavelengths is not negligible. At optical and near-infrared wavelengths we are able to estimate sources' 'po-

sitional uncertainty' by considering its measured size; we fix the positional uncertainty for each source individually by taking the area (measured in arcseconds squared) and elongation (both measured using SExtractor³) to convert to a semi-major axis. Most optical/near-infrared sources have approximated semi-major axes $\sim 0.5''$, with 90% of sources being $<1''$. Therefore, when seeking potential matches to $450\mu\text{m}$ sources, we search within a radius which is the $450\mu\text{m}$ source's positional uncertainty and the optical/near-infrared sources' approximated semi-major axis summed in quadrature.

The positional uncertainty of $24\mu\text{m}$ and 1.4 GHz sources is estimated with a more statistical method (since the resolution is not adequate to resolve source sizes) by measuring the global offset of $24\mu\text{m}$ and 1.4 GHz sources to K -band and i -band positions. We find that 90% of $24\mu\text{m}$ sources lie within $1.05''$ of their associated optical/near-infrared counterpart and 90% of 1.4 GHz sources lie within $0.85''$. Therefore, we add $1.05''$ and $0.85''$ (in quadrature) to our search radius for $24\mu\text{m}$ and 1.4 GHz counterparts, respectively. We observe many instances where $24\mu\text{m}$ and 1.4 GHz counterparts fall outside the $450\mu\text{m}$ positional uncertainty but lie $<1''$ beyond the positional uncertainty (e.g. 450.01). The median search radii at $450\mu\text{m}$ and $850\mu\text{m}$ were $2.2''$ and $4.2''$, respectively.

The advantage of identifying radio counterparts comes from the well-known FIR/radio correlation for starburst galaxies (Helou et al. 1985; Condon 1992), whereby a radio-detected galaxy is likely to be FIR-bright, and thus correspond to the source generating the FIR emission detected in our SCUBA-2 maps (Barger et al. 2000; Chapman et al. 2003, 2005). MIPS $24\mu\text{m}$ -emission also correlates with FIR emission since both are seen in dusty galaxies, although the relationship is more complex due to the variation of SED types in the mid-infrared (PAH emission features drifting in and out of the band, and AGN generated power law emission Le Floc'h et al. 2005; Lee et al. 2010). The existence of a mid-infrared or radio counterpart within the beamsize of $450\mu\text{m}$ observations can help distinguish that source from others as the likely counterpart, since the likelihood of random coincidence is quite low (this likelihood is often called the p -value; Downes et al. 1986)⁴.

A summary of counterparts is found in Table 6 for $450\mu\text{m}$ sources, Table 7 for marginal $450\mu\text{m}$ sources, and Table 8 for $850\mu\text{m}$ sources which are not $450\mu\text{m}$ -detected. Photometric redshifts (Ilbert et al. 2010) are quoted where available. Also, the handful of sources which have interferometric observations have their known counterparts in bold in Tables 6, 7 and 8. The interferometrically-observed subset of SCUBA-2 sources (along with all SCUBA-2 sources which were detected with other submillimeter instruments) is given in Table 4. The best-guess counterpart is the source with

³ SExtractor: a Source Extractor program developed in Bertin & Arnouts (1996).

⁴ We calculate the p -value (defined by $p = 1 - \exp(-\pi n \theta^2)$) where n is the source density, θ the angular offset or search area) by assuming the following source densities which we measure in this area of the COSMOS field: $885,900 \text{ deg}^{-2}$ at i -band; $151,900 \text{ deg}^{-2}$ at $3.6 \mu\text{m}$; $19,400 \text{ deg}^{-2}$ at $24 \mu\text{m}$; and $2,300 \text{ deg}^{-2}$ at 1.4 GHz.

Table 3. Marginal $3 < \sigma < 3.6$ $450\mu\text{m}$ -identified sources with $850\mu\text{m} > 3\sigma$ Counterparts.

Name	$850\mu\text{m}$ - Short Name	$450\mu\text{m}$ - Short Name	Offset [$''$]	RA ₄₅₀	DEC ₄₅₀	S/N ₈₅₀	S/N ₄₅₀	S ₄₅₀ RAW [mJy]	S ₄₅₀ DEBOOSTED [mJy]	S ₈₅₀ RAW [mJy]	S ₈₅₀ DEBOOSTED [mJy]	$\Delta(\alpha, \delta)$ [$''$]
SMM J100031.0+022751...	850.62	450.78	0.9	10:00:31.0	+02:27:51	4.29	3.60	14.94±4.15	10.72±4.99	3.46±0.81	2.80±0.96	2.42
SMM J100034.3+022121...	850.10	450.81	0.8	10:00:34.3	+02:21:21	8.60	3.58	14.71±4.11	10.47±4.98	6.90±0.80	6.24±1.13	2.45
SMM J095950.8+022745...	850.55	450.86	3.6	09:59:50.8	+02:27:45	4.51	3.55	19.80±5.58	13.95±6.80	4.77±1.06	3.89±1.27	2.50
SMM J100025.1+021847...	850.09	450.87	2.8	10:00:25.1	+02:18:47	8.89	3.55	15.24±4.30	10.74±5.24	7.47±0.84	6.83±1.17	2.50
SMM J100022.2+022842...	850.23	450.94	0.6	10:00:22.2	+02:28:42	6.24	3.50	14.67±4.19	10.14±5.17	5.06±0.81	4.31±1.07	2.58
SMM J100052.8+021906...	850.103	450.95	3.1	10:00:52.8	+02:19:06	3.54	3.50	18.59±5.31	12.83±6.56	3.88±1.10	2.94±1.34	2.59
SMM J100049.8+022448...	850.133	450.96	8.2	10:00:49.8	+02:24:48	3.25	3.49	15.25±4.36	10.50±5.39	2.85±0.88	2.06±1.09	2.60
SMM J095950.7+022823...	850.33	450.99	3.7	09:59:50.7	+02:28:23	5.54	3.47	20.15±5.80	13.76±7.20	6.20±1.12	5.18±1.41	2.63
SMM J100025.0+022757...	850.85	450.105	4.5	10:00:25.0	+02:27:57	3.73	3.44	14.24±4.14	9.60±5.16	2.99±0.80	2.32±0.97	2.69
SMM J100041.8+022358...	850.92	450.106	5.6	10:00:41.8	+02:23:58	3.67	3.44	14.19±4.13	9.57±5.15	2.94±0.80	2.27±0.97	2.69
SMM J100025.6+023051...	850.159	450.126	12.3	10:00:25.6	+02:30:51	3.05	3.36	15.79±4.70	10.32±5.91	2.89±0.95	2.02±1.19	2.83
SMM J100029.5+022131...	850.131	450.133	2.6	10:00:29.5	+02:21:31	3.27	3.32	13.67±4.12	8.78±5.19	2.64±0.81	1.91±1.00	2.90
SMM J100011.8+022935...	850.52	450.134	1.7	10:00:11.8	+02:29:35	4.73	3.31	14.45±4.36	9.26±5.50	4.09±0.86	3.37±1.04	2.91
SMM J095953.0+022641...	850.163	450.135	3.5	09:59:53.0	+02:26:41	3.00	3.31	16.78±5.07	10.76±6.39	2.91±0.97	2.02±1.22	2.91
SMM J100010.1+021758...	850.83	450.166	1.8	10:00:10.1	+02:17:58	3.77	3.24	15.87±4.90	9.79±6.20	3.52±0.93	2.74±1.12	3.08
SMM J100005.4+022516...	850.104	450.173	6.4	10:00:05.4	+02:25:16	3.51	3.22	13.31±4.13	8.11±5.23	2.82±0.80	2.12±0.98	3.13
SMM J100022.6+023023...	850.88	450.179	6.8	10:00:22.6	+02:30:23	3.69	3.21	14.51±4.52	8.80±5.73	3.31±0.90	2.56±1.08	3.15
SMM J100014.1+022836...	850.114	450.189	8.2	10:00:14.1	+02:28:36	3.40	3.17	13.37±4.22	7.92±5.33	2.81±0.83	2.08±1.02	3.25
SMM J100005.0+021718...	850.49	450.193	0.6	10:00:05.0	+02:17:18	4.79	3.16	17.40±5.50	10.27±6.95	4.94±1.02	4.05±1.24	3.27
SMM J100011.1+021507...	850.53	450.206	4.8	10:00:11.1	+02:15:07	4.68	3.14	20.69±6.60	12.04±8.32	5.72±1.22	4.70±1.47	3.33
SMM J100023.6+021916...	850.27	450.215	2.7	10:00:23.6	+02:19:16	6.08	3.11	13.05±4.20	7.48±5.28	5.00±0.82	4.23±1.08	3.39
SMM J100032.0+023324...	850.67	450.240	5.9	10:00:32.0	+02:33:24	4.07	3.06	19.01±6.21	10.61±7.75	5.15±1.26	4.12±1.50	3.51
SMM J100041.3+022534...	850.151	450.247	11.5	10:00:41.3	+02:25:34	3.12	3.05	12.58±4.13	6.97±5.14	2.52±0.81	1.79±1.02	3.54
SMM J100013.4+022224...	850.40	450.252	3.7	10:00:13.4	+02:22:24	5.20	3.04	12.57±4.14	6.91±5.15	4.16±0.80	3.47±0.99	3.57

Table Notes. Sources extracted down to 3σ in the $450\mu\text{m}$ map using $850\mu\text{m} > 3\sigma$ positional priors. The $450\mu\text{m} > 3\sigma$ list (with 274 sources) was checked against the $850\mu\text{m} > 3\sigma$ list (with 164 sources) and 25 sources were found. The positions here are given by their $450\mu\text{m}$ detection with associated positional uncertainty and the Offset is the offset between $450\mu\text{m}$ and $850\mu\text{m}$ centroid. The short names are numbered in order of decreasing S/N for all sources extracted in the map, e.g. from 450.00 at S/N= 7.80 to 450.273 with S/N= 3.00, hence the high, non-sequential numbers given at both $450\mu\text{m}$ and $850\mu\text{m}$.

the lowest p -value; generally, a p -value < 0.05 can be regarded as confident, while larger p -values are more tentative. Sources with p -values > 0.5 are removed from Tables 6–8 since they are more likely not truly-associated counterparts. Figure 15 (given at the end of this paper) show $12'' \times 12''$ postage stamp cutouts of the $450\mu\text{m}$ sources in the optical (*Biz* tricolor) and near-infrared (IRAC $3.6\mu\text{m}$) with radio and $24\mu\text{m}$ counterparts identified for reference.

A significant fraction of sources, both at $450\mu\text{m}$ and $850\mu\text{m}$ lack $24\mu\text{m}$ or radio counterparts. At $450\mu\text{m}$, only 44% (=34/78) of sources have $24\mu\text{m}$ or radio counterparts and at $850\mu\text{m}$, only 60% (=59/99, which is consistent with previous rates at $850\mu\text{m}$; Coppin et al. 2005). These fractions should improve with deeper radio data (e.g. as in Barger et al. 2012), which should be available in the coming years in the COSMOS field, but it would not fix the bias introduced in submillimeter samples which are reliant on these counterparts. Studies which are reliant on multiwavelength counterpart identification, yet which have a significant number of galaxies lacking counterparts, will be biased. However, note that the majority of sources without $24\mu\text{m}$ or radio counterparts *do* have IRAC near-infrared counterparts ($\sim 33/44=75\%$), and of those that do not, 7 sources have no counterparts at all (i.e. also lack any optical counterparts). This leaves only 4 objects (in both $450\mu\text{m}$ and $850\mu\text{m}$ samples) which rely on matching directly to optical counterparts—the most uncertain method generating the highest p -values. The median p -values for the different counterpart matching methods at $450\mu\text{m}$ are the following: 0.0009 (1.4 GHz, 16 galaxies), 0.02 ($24\mu\text{m}$, 18 galaxies), 0.09 ($3.6\mu\text{m}$, 33 galaxies), and 0.30 (optical/*i*-band, 4 galaxies).

3.5 Reliability of Counterpart Identifications

Identifying the correct multiwavelength counterpart(s) for each submillimeter source is the most important, but also the most difficult aspect of characterising the submillimetre galaxy population. Recently, it has become clear that direct, far-infrared interferometry is the only guaranteed method of identifying counterparts correctly (e.g. recent results from SMA, PdBI and ALMA targeting $850\mu\text{m}$ –1.1 mm sources; Younger et al. 2008; Wang et al. 2011; Barger et al. 2012; Smolčić et al. 2012; Karim et al. 2013; Hodge et al. 2013). For $850\mu\text{m}$ sources detected with a $\sim 15''$ beamsize, interferometric work suggests that best-guess counterpart matching to radio and/or $24\mu\text{m}$ counterparts will fail $\sim 30\%$ of the time (Hodge et al. 2013, and Smail, private communication), dependent on ancillary field depth and robustness of FIR/radio and FIR/mid-infrared correlations. This provides a good estimate to the accuracy of the counterparts given in Table 5 for our $850\mu\text{m}$ sample, but what is the reliability of our $450\mu\text{m}$ source counterparts?

For the five $450\mu\text{m}$ sources which have interferometric observations, four would have been traditionally matched with their truthful counterpart using our method; two of those sit within the $450\mu\text{m}$ positional uncertainty $< 1.5''$, two are outside but still $< 2''$ away, and one source, 450.08, is $6.8''$ away from our SCUBA-2 position. Unfortunately, small number statistics on interferometric observations limit interpretation.

In the absence of interferometry, we can speculate that the reduced beamsize with respect to $850\mu\text{m}$ would see a reduction in counterpart contamination proportional to the reduction in sky area searched for potential counterparts. The positional uncertainties of $450\mu\text{m}$ range from 1.0– $2.4''$ at $> 3.6\sigma$ (with a median of $\sim 2.1''$), while $850\mu\text{m}$ positional

Table 4. Identification of SCUBA-2 Sources at 870 μm –1.2 mm

450 μm - NAME	850 μm - NAME	ALTERNATE NAME	λ_{obs} [mm]	S_{λ} [mJy]	INTERFER- OMETRIC?	INST./ TEL	REFERENCE
450.00	850.07	AzTEC J100028.94+023200.3	1.1	3.8 \pm 0.9		AzTEC	Scott et al. (2008)
450.01	850.02	AzTEC/C80	1.1	4.1 \pm 0.9		AzTEC	Aretxaga et al. (2011)
		COSLA-47	0.87	9.0 \pm 2.8		LABOCA	Navarette et al. in prep
		COSLA-47	1.3	3.11 \pm 0.59	Y	PdBI	Smolčić et al. (2012)
450.03	850.00	AzTEC J100008.03+022612.1	1.1	8.3 \pm 1.1		AzTEC	Scott et al. (2008)
		AzTEC-2	0.89	12.4 \pm 1.0	Y	SMA	Younger et al. (2007, 2009)
		AzTEC/C3	1.1	10.5 \pm 1.0		AzTEC	Aretxaga et al. (2011)
450.04	850.03	AzTEC J100019.73+023206.0	1.1	6.5 \pm 1.3		AzTEC	Scott et al. (2008)
		AzTEC-5	0.89	9.3 \pm 1.3	Y	SMA	Younger et al. (2007, 2009)
		AzTEC/C42	1.1	4.8 \pm 1.1		AzTEC	Aretxaga et al. (2011)
450.05	850.08	AzTEC/C38	1.1	5.1 \pm 1.0		AzTEC	Aretxaga et al. (2011)
		COSLA-35	0.87	8.2 \pm 2.2		LABOCA	Navarette et al. in prep
		COSLA-35	1.3	2.15 \pm 0.51	Y	PdBI	Smolčić et al. (2012)
450.07	850.98	AzTEC/C169	1.1	3.1 \pm 0.8		AzTEC	Aretxaga et al. (2011)
450.08	850.46	COSLA-8	0.87	6.9 \pm 1.6		LABOCA	Navarette et al. in prep
		COSLA-8	1.3	2.65 \pm 0.62	Y	PdBI	Smolčić et al. (2012)
450.16		COSBO3**	1.2	7.4 \pm 1.1		MAMBO	Bertoldi et al. (2007)
		AzTEC/C6**	1.1	9.6 \pm 1.0		AzTEC	Aretxaga et al. (2011)
450.20	850.24	AzTEC J100004.54+023040.1	1.1	3.3 \pm 0.8		AzTEC	Scott et al. (2008)
		AzTEC/C150	1.1	3.3 \pm 1.2		AzTEC	Aretxaga et al. (2011)
450.27	850.115	AzTEC/C65	1.1	4.4 \pm 1.0		AzTEC	Aretxaga et al. (2011)
450.28	850.05	COSBO3**	1.2	7.4 \pm 1.1		MAMBO	Bertoldi et al. (2007)
		AzTEC/C6**	1.1	9.6 \pm 1.0		AzTEC	Aretxaga et al. (2011)
450.38	850.14	AzTEC/C24	1.1	5.7 \pm 1.0		AzTEC	Aretxaga et al. (2011)
450.55	850.06	COSBO7	1.2	5.0 \pm 0.9		MAMBO	Bertoldi et al. (2007)
		AzTEC/C160	1.1	3.1 \pm 1.2		AzTEC	Aretxaga et al. (2011)
450.66	850.146	AzTEC/C66	1.1	4.3 \pm 0.9		AzTEC	Aretxaga et al. (2011)
	850.01	AzTEC J095957.22+022729.3	1.1	5.8 \pm 1.0		AzTEC	Scott et al. (2008)
		AzTEC-9	0.89	13.5 \pm 1.8	Y	SMA	Younger et al. (2007, 2009)
		AzTEC/C18	1.1	7.9 \pm 1.5		AzTEC	Aretxaga et al. (2011)
	850.04	COSBO1	1.2	6.2 \pm 0.9		MAMBO	Bertoldi et al. (2007)
		AzTEC/C7	1.1	8.9 \pm 1.1		AzTEC	Aretxaga et al. (2011)
	850.13	AzTEC/C114	1.1	3.7 \pm 0.9		AzTEC	Aretxaga et al. (2011)
	850.15	AzTEC J100025.23+022608.0	1.1	1.9 \pm 0.6		AzTEC	Scott et al. (2008)
		AzTEC/C30	1.1	5.5 \pm 1.1		AzTEC	Aretxaga et al. (2011)
	850.18	AzTEC J100023.98+022950.0	1.1	2.6 \pm 0.7		AzTEC	Scott et al. (2008)
	850.20	AzTEC J100026.68+023128.1	1.1	2.8 \pm 0.8		AzTEC	Scott et al. (2008)
	850.22	COSLA-50	0.87	5.6 \pm 1.6		LABOCA	Navarette et al. in prep
		COSLA-50	1.3	...	Y	PdBI	Smolčić et al. (2012)
		AzTEC/C33	1.1	5.3 \pm 1.1		AzTEC	Aretxaga et al. (2011)
	850.25	COSBO19	1.2	3.0 \pm 0.8		MAMBO	Bertoldi et al. (2007)
		COSLA-38	0.87	5.8 \pm 1.6		LABOCA	Navarette et al. in prep
		COSLA-38	1.3	8.19 \pm 1.85	Y	PdBI	Smolčić et al. (2012)
450.99	850.33	AzTEC J095950.69+022829.5	1.1	3.6 \pm 0.9		AzTEC	Scott et al. (2008)
	850.35	AzTEC/C74	1.1	4.2 \pm 0.9		AzTEC	Aretxaga et al. (2011)
	850.50	AzTEC/C35	1.1	5.2 \pm 1.0		AzTEC	Aretxaga et al. (2011)
	850.57	AzTEC/C45	1.1	4.8 \pm 1.0		AzTEC	Aretxaga et al. (2011)
450.78	850.62	AzTEC J100031.06+022751.5	1.1	2.7 \pm 0.8		AzTEC	Scott et al. (2008)
	850.63	COSBO36	1.2	5.7 \pm 1.3		MAMBO	Bertoldi et al. (2007)
		AzTEC/C71	1.1	4.3 \pm 1.1		AzTEC	Aretxaga et al. (2011)
	850.94	COSBO29	1.2	3.1 \pm 1.0		MAMBO	Bertoldi et al. (2007)
		AzTEC/C162	1.1	3.1 \pm 1.2		AzTEC	Aretxaga et al. (2011)

Table Notes. Counterparts of SCUBA-2 sources at 870 μm –1.2 mm as identified by LABOCA, PdBI, AzTEC, SMA and MAMBO with given references. Sources are divided into 450 μm $>3.6\sigma$ and 850 μm $>3.6\sigma$ samples. None of the marginal $3 < \sigma < 3.6$ 450 μm /850 μm sources were reported as detections in the given references. Sources are searched within a 10'' (450 μm sources) or 12'' (850 μm sources) search radius; this is approximately one beamsize at $\sim 850\mu\text{m}$ –1.2 mm and represents a regime where chance coincidence between submm sources is very low (p -value < 0.01). Flux densities (S_{λ}) are deboosted and not raw. Sources marked with ** correspond to multiple SCUBA-2 sources in the Table, i.e., 450.16, 450.28 and 850.05 all correspond to COSBO3/AzTEC/C6.

uncertainties vary from 2–6'' at $>3.6\sigma$ (median of 3.6''). This suggests the same counterpart identification strategy (when applied to 450 μm samples) should fail only $\sim 5\%$ of the time.

While this thought experiment gives a good ballpark figure for counterpart correctness, we can also use the individual source probabilities of correctness, given by the p -value to compute the likely number of incorrect counterparts. The likelihood of all 71 450 μm counterparts being correct (note that 7 sources lack any counterparts) is $\sim 0.4\%$, the probability of one contaminant is 2.7%, the probability of two is 8%, three is 15%, four is 20%, five is 20%, six is 15%, seven is 8%, and higher than seven contaminants is 11%

likely. Therefore, we anticipate that 5–10% of our 450 μm sample has incorrect counterpart matches; it is most likely the sources with incorrect counterparts are those with the highest p -values. While this emphasises the importance of securing the correct counterparts for detailed follow-up on individual sources, this will not impact the bulk result of our analysis on the 450 μm population (in terms of redshift distribution, luminosities, etc) significantly.

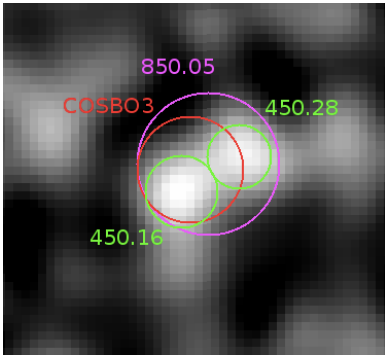


Figure 9. A $35 \times 40''$ $450\mu\text{m}$ signal-to-noise map cutout of 450.16 and 450.28. The $450\mu\text{m}$ sources are circled and labelled in green, while COSBO3, the MAMBO-detected 1.2 mm source is shown in red and the $850\mu\text{m}$ SCUBA-2 source, 850.05, is shown in magenta. The beamsizes at $450\mu\text{m}$, $850\mu\text{m}$, and 1.2mm are $7''$, $15''$, and $11''$ respectively.

3.6 Multiplicity

The improved resolution from interferometry makes it clear that a potentially large fraction (20–50%) of bright ($>10\text{mJy}$) SMGs are actually multiples (Wang et al. 2011; Barger et al. 2012; Hodge et al. 2013). Although SCUBA-2 is a bolometer array and not an interferometer, the high resolution at $450\mu\text{m}$ can detect multiple sources when longer-wavelength observations only detect one SMG. This phenomenon is found once at high S/N in our sample, surrounding sources 450.16 and 450.28; the system is illustrated in Figure 9. There is only one long-wavelength submillimeter source detected in this area: 850.05 in our sample, as well as COSBO3, detected at 1.2 mm (Bertoldi et al. 2007), and AzTEC/C6, detected at 1.1 mm (Aretxaga et al. 2011). However, we find two $450\mu\text{m}$ sources within the SCUBA-2 $850\mu\text{m}$ beam: 450.16 with a S/N of ~ 4.6 and 450.28 with a S/N of ~ 4.2 . This is the best unequivocal identification of a multiple at $450\mu\text{m}$ in our sample.

This demonstrates that shorter-wavelength, smaller beamsize bolometers can be used to probe submillimeter galaxy multiplicity in blank-field surveys at potentially lower observational cost than interferometric follow-up (e.g. future large-field surveys from LMT and CCAT).

4 DERIVED SOURCE CHARACTERISTICS

4.1 Redshift Distributions

Figure 10 shows the distributions of optical/near-infrared photometric redshifts (Ilbert et al. 2010) for the best-guess counterparts identified in Tables 6 and 8. Photometric redshifts span $0 < z < 5.1$, with most sources at $z < 3$. The median redshift for the $450\mu\text{m}$ sample is $z = 1.95 \pm 0.19$ while the median for the $850\mu\text{m}$ population is $z = 2.16 \pm 0.11$, in agreement with previous work at $850\mu\text{m}$ (Chapman et al. 2005; Wardlow et al. 2011). The uncertainties on the median are generated via bootstrapping methods.

At $850\mu\text{m}$, we split our sample by its potential biases. The increased beamsize of $850\mu\text{m}$ observations means that $850\mu\text{m}$ sources which lack $24\mu\text{m}$ or radio identifications have

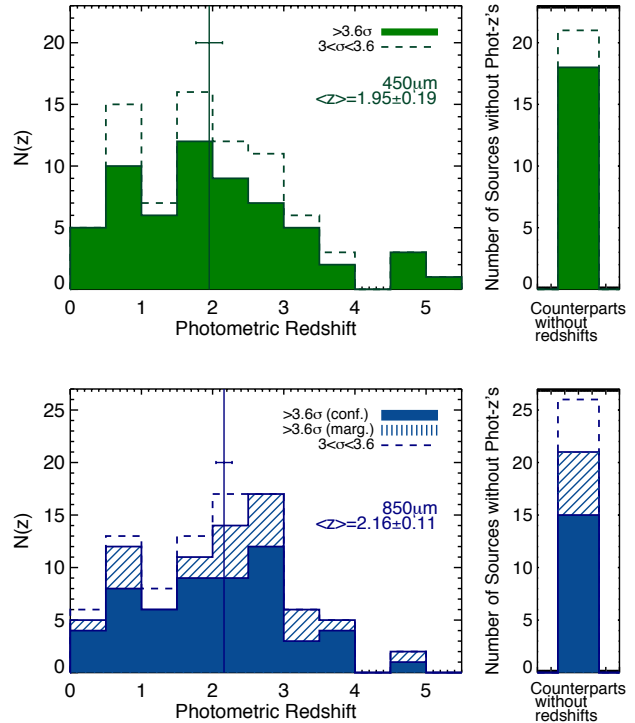


Figure 10. The distribution in photometric redshift for SCUBA-2 sources identified at $450\mu\text{m}$ (green) and $850\mu\text{m}$ (blue). The median redshifts of the two samples are $\langle z \rangle = 1.95$ and $\langle z \rangle = 2.16$ respectively. At $450\mu\text{m}$, we illustrate two distributions, the first consisting of just $>3.6\sigma$ $450\mu\text{m}$ sources (solid green shaded region), and the second of the $3 < \sigma < 3.6$ sample (dashed green line). We also indicate the number of sources without photometric redshifts at right. Due to the larger beamsize at $850\mu\text{m}$, our counterpart matching is done first using $24\mu\text{m}$, radio, or $450\mu\text{m}$ identification (solid blue shaded region). The remaining $850\mu\text{m}$ SMGs without $24\mu\text{m}$ /radio/ $450\mu\text{m}$ counterparts are shown in the hashed region. The dashed blue line corresponds to the $3 < \sigma < 3.6$ sample. The median redshifts are marked with vertical lines and 1σ bootstrap uncertainty on the median.

more uncertain counterparts. We illustrate the distribution of redshifts for the $24\mu\text{m}$ /radio identified subset, then those without (dashed area) and finally those from the $3 < \sigma < 3.6$ marginal catalogue. Note that the number of sources lacking redshift identifications is ≈ 18 –21 (amounting to 21–23%) of either sample.

Are those sources without photometric redshifts intrinsically different than those with photometric redshifts? We investigate this by seeing if the FIR properties, i.e. S_{850} to S_{450} colour, (a) evolves with redshift, or (b) differs between the sample of galaxies with photometric redshifts and without. Figure 11 plots the FIR colour of both $>3.6\sigma$ samples against photometric redshift and in histogram form. As expected, $450\mu\text{m}$ sources are much brighter at $450\mu\text{m}$ than $850\mu\text{m}$ and vice versa. There is some shallow evolution of the $\log(S_{850}/S_{450})$ colour with redshift, although the statistical variation within subsamples dominates. As we find that sources display a wide range of FIR properties irrespective of redshift, this does not necessarily bode well for work which

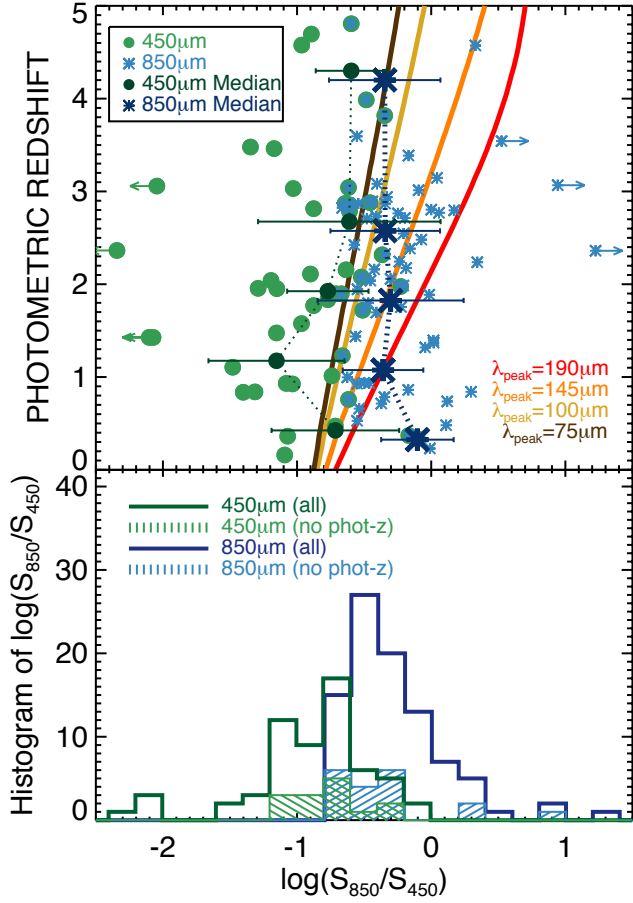


Figure 11. The FIR colour properties of the SCUBA-2 sample, measured as $\log(S_{850}/S_{450})$. At top, we plot against the optical/near-infrared photometric redshift. Sources with arrows represent galaxies which have flux densities close to zero in one band or the other; sources with negative flux densities are not included here. The $450\mu\text{m}$ sample (green) has, on average, $450\mu\text{m}$ flux densities which exceed $850\mu\text{m}$ flux densities by a factor of 5, while the $850\mu\text{m}$ sample (blue) has naturally ‘redder’ colours. Median values, binned by redshift, are shown in dark green/blue with deviations in the population indicated by error bars (the uncertainties in the median are much smaller $\sim 0.05\text{--}0.08$ dex). Slight redshift evolution is seen in the median. We overplot evolution of constant temperature (or constant SED peak wavelength) and note that our samples are inconsistent with non-evolving SED shape (i.e. the dust temperatures of high redshift, more luminous sources are much higher than they are at low redshift). At bottom, we plot the distribution in FIR colour for both samples with the subset of the samples which do not have any photometric redshift. The distribution of colours for the samples without redshifts resembles the parent population, indicating no obvious redshift-colour bias.

makes use of FIR photometric redshifts which assume a certain FIR template with fixed temperature and use FIR photometry to estimate the redshift more precisely than $\Delta z \sim 2$ (some work using this technique include Roseboom et al. 2012; Barger et al. 2012; Chen et al. 2013, , but often under specific luminosity restrictions, not broadly applicable to a wide range of high- z ULIRGs). Furthermore, sources

which do not have photometric redshifts show roughly the same distribution in FIR colour as the parent population of galaxies they are selected from. This suggests that the systems lacking photometric redshifts are not intrinsically biased with FIR properties. While there is significant variation in SED shape, the differences between the measured medians for $450\mu\text{m}$ and $850\mu\text{m}$ samples (measured by uncertainty of the median) are statistically significant at $>5\sigma$ at $z \lesssim 2$ and $\sim 3\sigma$ at $z \sim 3$.

It is difficult to say if sources without photometric redshifts differ significantly from those with redshift estimates. Wardlow et al. (2011) estimate the redshift distribution of $870\mu\text{m}$ sources in CDFS without photometric redshifts using the density of IRAC $3.6\mu\text{m}$ emitters, and guess that they largely sit at $z \sim 2.5$, near the expected peak of the whole population. The SCUBA2 population is likely similar to the $870\mu\text{m}$ galaxies from Wardlow et al. (2011), although only spectroscopic confirmation will unequivocally reveal their true nature.

4.2 Infrared luminosities & dust properties

We can go beyond basic FIR colour comparisons with our SCUBA-2 data and use SED fits to measure infrared luminosities, temperatures and in some cases dust masses. Simple greybody SED fitting combined with a mid-infrared powerlaw gives us this information with a minimum number of free parameters or model assumptions. We fit all available infrared photometry, from $24\mu\text{m}$ MIPS, $70\mu\text{m}$ MIPS, $450\mu\text{m}$ SCUBA-2, $850\mu\text{m}$ SCUBA-2, $870\mu\text{m}$ LABOCA, 1.1 mm AzTEC, 1.2 mm MAMBO, and 1.3 mm PdBI.

The combination of a greybody and mid-infrared powerlaw accounts for both galaxy-wide cold dust emission and smaller-scale warm dust emission (Blain et al. 2003; Kovács et al. 2006). The fitting method is described in full in Casey (2012) and is represented by the equation

$$S_\nu = N_{\text{bb}} \frac{(1 - e^{-(\nu/\nu^0)^\beta})\nu^3}{e^{h\nu/kT} - 1} + N_{\text{pl}}(c/\nu)^\alpha e^{-(\nu_c/\nu)^2} \quad (3)$$

where S_ν is flux density (in units of mJy), T is greybody dust temperature, β is the emissivity index of the greybody, α is the mid-infrared powerlaw slope, and N_{bb} and N_{pl} are the normalisations of the greybody and powerlaw, respectively (N_{pl} is a fixed function of N_{bb} , T , and α). Note however that in this work we do not quote our best-fit temperatures since they are heavily dependent on the assumed opacity and emissivity model. For example, an SED peaking at $100\mu\text{m}$ can be described as 29 K (blackbody), 31 K (optically thin greybody), 44 K (greybody with $\tau = 1$ at $100\mu\text{m}$), or 46 K (greybody with $\tau = 1$ at $200\mu\text{m}$). All of these models have been used in the literature to derive dust temperature despite the fact that they are not directly comparable (e.g. Blain et al. 2003; Kovács et al. 2010; Casey et al. 2009a; Coppin et al. 2008; Hwang et al. 2010); see Casey (2012), Figure 2, for more details on the impact of model assumption on measured dust temperature. Instead of estimating temperatures, we estimate the rest-frame SED peak wavelength of S_ν called $\lambda_{\text{peak}} (\propto 1/T_{\text{dust}})$, which is much more easily constrained by the data.

Since the number of far-infrared photometric data points is limited to 2–5 (from *Spitzer*-MIPS, SCUBA-2,

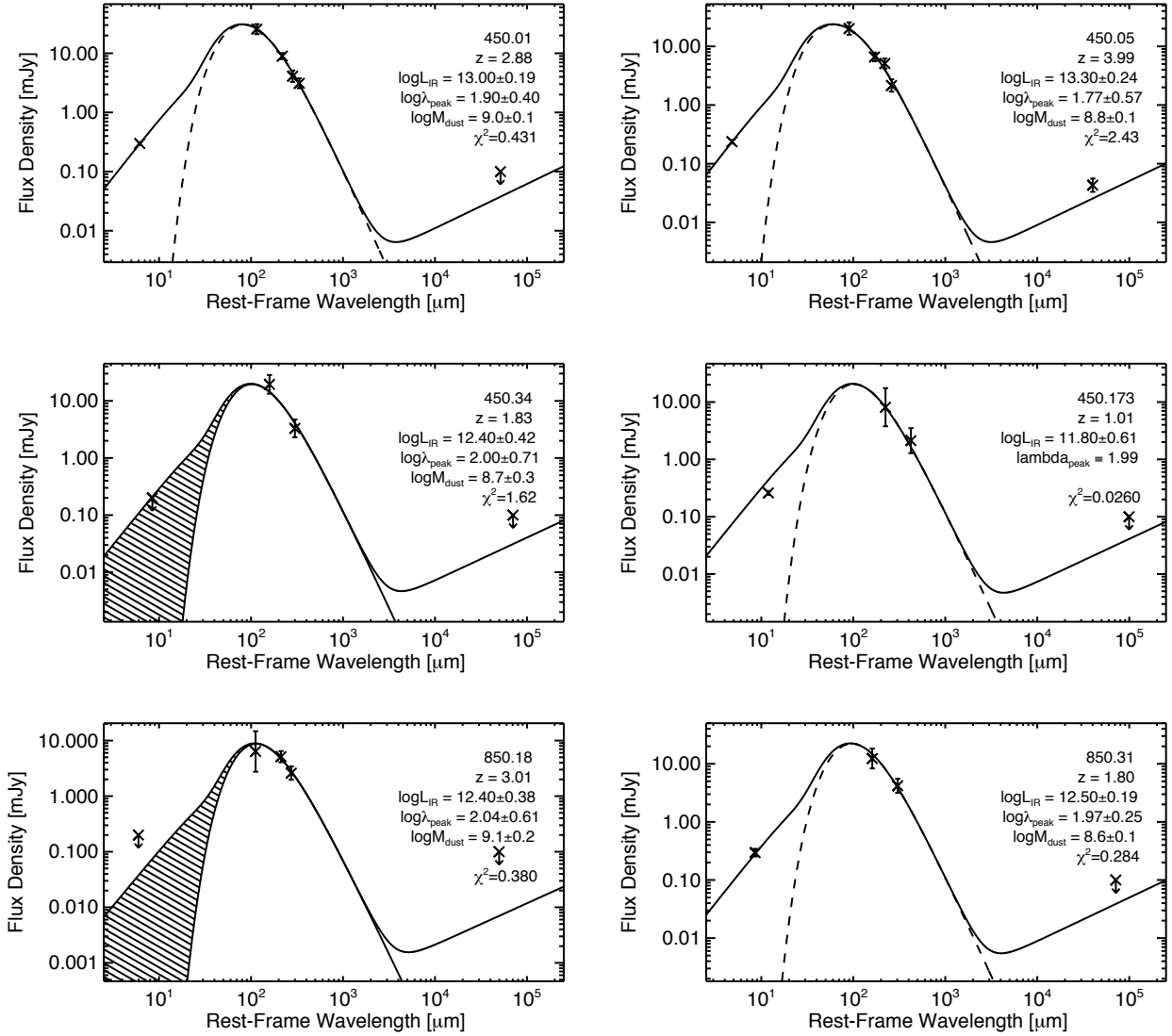


Figure 12. Example far-infrared SEDs for select SCUBA-2 sources, some 450 μm -selected and some 850 μm -selected. The assumed optical/near-infrared photometric redshift is specified in the upper right corner of each panel, as well as the measured L_{IR} , λ_{peak} , M_{dust} , and χ^2 goodness of fit. If the SED fit used a fixed temperature due to a lack of >2 infrared photometric detections, then no dust mass is measured. In cases where there is no 24 μm detection, the mid-infrared portion of the SED is shaded to indicate its uncertainty. The uncertainty in L_{IR} reflects this uncertainty. The radio portion of the SEDs are extrapolated from assuming the FIR/radio correlation holds (and evolves as measured in Ivison et al. 2010a,b) and are not fit to the radio data.

AzTEC and MAMBO measurements), we only fit SEDs with two free parameters, L_{IR} , and λ_{peak} and do not attempt to constrain emissivity or mid-infrared powerlaw index⁵. The emissivity index, $\beta = 1.5$ is fixed (e.g. Pope et al. 2008; Younger et al. 2009; Chapin et al. 2010), as is the mid-infrared powerlaw index, $\alpha = 2.0$ (e.g. Blain et al. 2003; Casey 2012). A representative sample of best-fit SEDs, including both high and low signal-to-noise sources, is illustrated in Figure 12.

⁵ Although for sources with ≥ 4 photometric points at $>3\sigma$, we allow variation in α ; this removes some reliance on the 24 μm flux to map directly to the FIR peak.

Table 9 gives the basic derived properties from the SED fits, including χ^2 goodness of fit, L_{IR} , the implied SFR from L_{IR} to one significant figure⁶, and the SED peak wavelength and dust masses, λ_{peak} and M_{dust} . Note that all of the flux densities used in the fits do factor into χ^2 , even non-detections; instead of treating non-detections as upper limits, we treat them as flux density measurements with very low significance (given by the extracted flux density from the map at the extracted position). The uncertainties on L_{IR} , λ_{peak} and M_{dust} are derived from the photometric un-

⁶ Assuming the Kennicutt (1998b) L_{IR} -SFR scaling and a Salpeter IMF.

certainties in the FIR data and average ~ 0.2 – 0.4 dex, ~ 0.2 – 0.4 dex and ~ 0.4 – 0.5 dex respectively. These uncertainties *do not* account for uncertainty in the IMF or dust absorption coefficient which impact the SFR and M_{dust} respectively. Sources with just two FIR photometric points (and upper limits at other bands) have SEDs fixed to the mean dust λ_{peak} of their parent sample, either $450\mu\text{m}$ -selected galaxies or $850\mu\text{m}$ -selected galaxies. In the next section we measure these peak wavelengths as $\log \lambda_{\text{peak}} = 2.05 \pm 0.04$ and $\log \lambda_{\text{peak}} = 2.12 \pm 0.03$, respectively. We do not attempt to constrain the SEDs of sources without photometric redshifts.

4.3 Bulk Infrared Properties of the Population

Figure 13 illustrates infrared luminosities against photometric redshift for both $450\mu\text{m}$ - and $850\mu\text{m}$ -selected galaxies. Both $450\mu\text{m}$ and $850\mu\text{m}$ samples by and large sit at $1 < z < 4$ with $10^{12} < L_{\text{IR}} < 10^{13.2} L_{\odot}$. This is very similar to the luminosity and redshift range probed by the original SCUBA $850\mu\text{m}$ surveys; the distribution of the Chapman et al. (2005) spectroscopically-confirmed sample (with improved luminosity estimates using photometry from Kovács et al. 2006) is shown for comparison. The parameter space probed by ~ 1 mm-selected populations (e.g. Yun et al. 2012) is similar. We also compare to the recent spectroscopically-confirmed sample of *Herschel*-SPIRE sources analysed in Casey et al. (2012a) and Casey et al. (2012b); the SPIRE sources (selected at 250 – $500\mu\text{m}$) peak in density at lower redshifts and lower luminosities, although at a given redshift, the SCUBA-2 sources probe ~ 0.1 – 0.5 dex fainter sources than SPIRE.

The distributions in infrared luminosity and peak SED wavelength (the two free parameters of our SED fitting technique) are plotted in the middle of Figure 13 and can be used to assess basic differences between subsets of the population. What we find is that the subset detected at both $450\mu\text{m}$ and $850\mu\text{m}$ are more luminous than the marginal sample and those detected at only one wavelength. The median SED peak wavelength of the $850\mu\text{m}$ -only sample is longer than those detected at both wavelengths (translating to cooler temperatures). The subsets which are $450\mu\text{m}$ -only detected and marginal $3 < \sigma < 3.6$ sources have median SED peak wavelengths which lie between. Uncertainties on the median values in luminosity and SED peak wavelength are determined through bootstrapping.

Figure 13 also shows the change in SED peak wavelength with redshift, where higher redshift sources tend to have hotter SEDs peaking at shorter rest-frame wavelengths. This increase in temperature (decrease in SED peak wavelength) also correlates with L_{IR} , whereby the higher redshift sources are also the most luminous and hotter, which is a well-documented correlation (e.g. Soifer et al. 1987, 1989; Chapman et al. 2003; Chapin et al. 2009; Hwang et al. 2010). Figure 13 shows us that the sources detected only at $450\mu\text{m}$ are statistically warmer (peak at shorter wavelengths) than average and $850\mu\text{m}$ are statistically cooler (peak at longer wavelengths), and that the difference in median peak wavelengths is $\Delta \log(\lambda_{\text{peak}}) = 0.16$ dex, which is $\sim 50\mu\text{m}$, at $z \lesssim 1$ and 0.10 dex at $1 < z < 2.5$, which is $\sim 20\mu\text{m}$.

These results suggest that, by and large, SCUBA-2 $450\mu\text{m}$ and $850\mu\text{m}$ galaxies are not significantly dissim-

ilar in their redshifts, luminosities, or SED peak wavelengths/temperatures, but that systems detected in only one of the two bands can be primarily distinguished based on their SED peak wavelengths (or temperatures) rather than their luminosities or redshifts.

4.4 Galaxies' distribution in z – L_{IR} – λ_{peak} space

To better understand the relative selection differences between $450\mu\text{m}$ and $850\mu\text{m}$, we use Monte Carlo methods to test for detectability as a function of the primary SED parameters, z , L_{IR} , and λ_{peak} . For a given redshift, luminosity and SED peak wavelength, we generate a number of SEDs satisfying those characteristics with varying emissivity, opacities, and mid-infrared powerlaw slopes and then compute the relative probability that a galaxy of those characteristics (z , L_{IR} , and λ_{peak}) is detectable in our survey. Instead of setting a strict flux density threshold which is representative of our sample (e.g. $S_{450} > 14.9$ mJy or $S_{850} > 2.9$ mJy, at $> 3.6\sigma$), we inject galaxies of these given SED types into our jackknife maps and measure the $> 3.6\sigma$ detectability.

We then assume an underlying distribution or density of galaxies in z – L_{IR} – λ_{peak} space, as given by integrated-infrared luminosity functions (Le Flocc'h et al. 2005; Caputi et al. 2007; Magnelli et al. 2011; Casey et al. 2012a; Grupioni et al. 2013). However, the luminosity functions only constrain the distribution of galaxies in z and L_{IR} , therefore we must assume some distribution of sources in SED peak wavelength, or temperature. The simplest assumption is that any galaxy SED, regardless of luminosity or redshift, should peak at $100 \pm 40\mu\text{m}$. This model of the population fails since it predicts that $450\mu\text{m}$ -detected galaxies peak at $\langle z \rangle = 0.8$ while $850\mu\text{m}$ -detected galaxies peak at $\langle z \rangle = 2.8$. It also predicts that the populations have indistinguishable SED shapes and that nearly all $450\mu\text{m}$ sources will be $850\mu\text{m}$ detected. Both the predicted redshift and SED peak wavelength distributions and fraction of overlap between populations disagree significantly with our observations.

Adjusting the distribution of sources in SED peak wavelength produces results which are consistent with our observations. In other words, by invoking a correlation whereby $L_{\text{IR}} \propto T_{\text{dust}} \propto 1/\lambda_{\text{peak}}$, we can predict $\langle z \rangle = 1.5$ – 2.0 for $450\mu\text{m}$ sources and $\langle z \rangle = 2.3$ – 2.6 for $850\mu\text{m}$ sources. Perhaps most pertinent, we can recover approximately the same overlap fraction of the population, namely that only ~ 25 – 40% of the $450\mu\text{m}$ galaxies are $850\mu\text{m}$ detected and vice versa. The predicted SED peak wavelength distributions also differ between $450\mu\text{m}$ and $850\mu\text{m}$ with this model. Unfortunately, our data are not significant enough to place meaningful constraints on the slope of the underlying correlation between luminosity and peak wavelength, or provide better estimates to overlap fraction than $\sim 25\%$. However, future large samples ($N \approx 5000$) selected at even more wavelengths across the submillimeter will provide meaningful constraints on the distribution of galaxies in z – L_{IR} – λ_{peak} space.

These simulations can also be used to test the reliability of our SED fits. For instance, does SED fitting at $450\mu\text{m}$ and $850\mu\text{m}$ (vs. a more fully-sampled range of wavelengths) have a systematic effect on measured SED peak wavelength? Having generated sets of SEDs which describe a galaxy of known

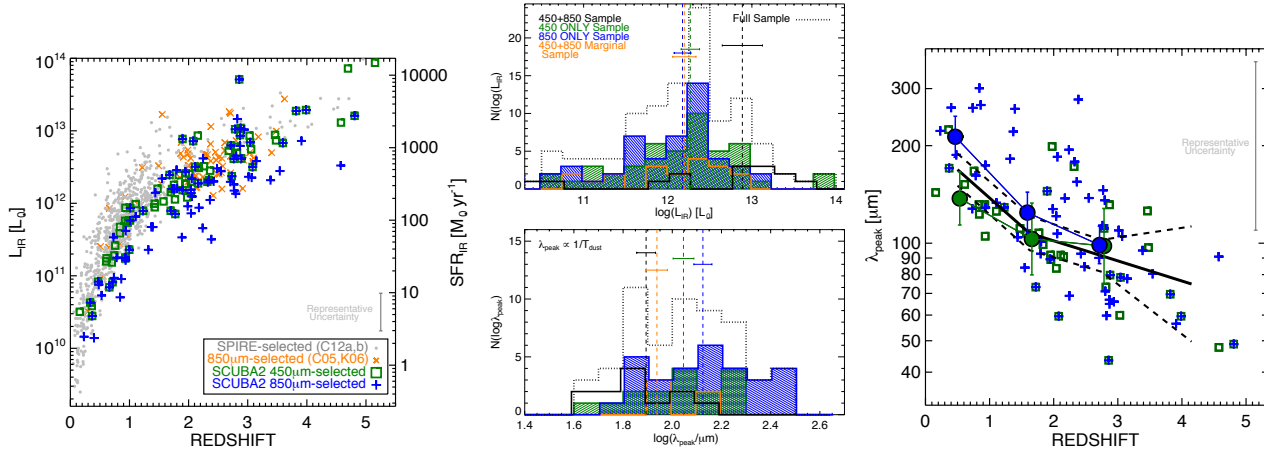


Figure 13. **LEFT:** Infrared luminosity against photometric redshift for 450 μm (green squares) and 850 μm -selected (blue crosses) sources. For context, the 850 μm -selected SCUBA sources (orange crosses; Chapman et al. 2005; Kovács et al. 2006) and *Herschel*-SPIRE-selected, spectroscopically confirmed sources (gray circles; Casey et al. 2012a,b) are overplotted. The mean redshift of the SCUBA2 sample is similar to the original SCUBA-selected sources and higher than SPIRE sources while the SCUBA-2 luminosities, at a given redshift, probe to slightly lower luminosities (~ 0.1 – 0.4 dex) than SPIRE sources. **MIDDLE:** Histograms of infrared luminosity and SED peak wavelength (inversely proportional to dust temperature), for various subsamples of SCUBA-2 sources: the whole sample (dotted lines), the overlapping $>3.6\sigma$ 450 and 850 sources (detected in both bands, black), 450 μm $>3.6\sigma$ sources not detected at 850 μm (green), 850 μm $>3.6\sigma$ sources not detected at 450 μm (blue), and the marginal $3 < \sigma < 3.6$ 450 and 850 source catalogue (orange). Vertical lines mark the median value for each subset and 1σ statistical variation on the median determined by bootstrapping. **RIGHT:** SED peak wavelength against redshift for sources which have peak wavelength constraints. The median SED peak wavelength for all SCUBA-2 galaxies as a function of redshift is shown in black with dashed 67% intervals and error bars representing uncertainty on the median. The median dust temperature evolution of 450 μm -only detected galaxies is shown as green circles, while 850 μm -only detected galaxies are in blue. At low redshifts ($z \leq 2$) the two populations have statistically distinct SED shapes, echoing the results from Figure 11.

z , L_{IR} and λ_{peak} , we can re-measure the SED characteristics by refitting the noise-added 450 μm and 850 μm photometry (and using an additional constraint at observed 24 μm). At high signal-to-noise, where galaxies are luminous enough to be detected at both wavelengths, the scatter in the log of measured SED peak wavelength is 0.05 dex with no systematic offset. At lower luminosities, where galaxies are more likely to be detected in only one of the two bands, the scatter in measured SED peak wavelength increases to 0.11 dex although there is still no systematic offset. We attribute the lack of systematic offset in measured peak wavelengths to the SCUBA-2 selection wavelengths, which sample the SED in significantly different regimes, e.g. the SED’s peak and the SED’s Rayleigh-Jeans tail. Even galaxies which are not formally detected in one of the two bands still has a flux density constraint at both wavelengths which, on average, provides an accurate estimate to the SED peak wavelength.

5 DISCUSSION

The ultimate goal of this work is the characterisation of galaxies which emit at 450 μm and 850 μm , how they relate to other similarly-selected galaxy populations, how they relate to the more extensively-studied optical/UV-selected populations, and how important they are in the context of total star formation in the Universe. Follow-up studies can pursue source characterisation in more detail. These initial observations from SCUBA-2 are also incredibly valuable in providing first insight of high-resolution bolometer observations which will become more commonplace with completion

of the Large Millimeter Telescope (LMT) and the Cornell-Caltech Atacama Telescope (CCAT).

5.1 Are 450 μm and 850 μm populations different?

When contrasting the physical characteristics of 450 μm with 850 μm galaxies, like redshift distribution, luminosity, and dust temperature, this work suggests that the two populations are quite similar. Are these similarities between 450 μm and 850 μm galaxies what we expect, given the lack of direct overlap of the samples?

If you naïvely assume there is little evolution or luminosity dependence of SMG SEDs, then selecting at shorter wavelengths than 850 μm would select a lower redshift population. If you take the mean redshift for 850 μm -selected SMGs as $\langle z \rangle = 2.2$ and assume they peak at rest-frame 100 μm , then no change in SED type would predict the mean redshift for 450 μm -selected galaxies is $\langle z \rangle \approx 0.5$. This assumption fails primarily since it does not consider that 850 μm selects galaxies almost exclusively on the Rayleigh-Jeans tail of dust emission versus the peak. Adjusting this to reflect that 450 μm will select more galaxies near their peak (a factor of ~ 2 in wavelength) implies that 450 μm galaxies should peak near $\langle z \rangle \approx 1$ (this test is similar to that in section 4.4). Still, this is inconsistent with our data which predicts that both populations peak at around $z \sim 2$.

Geach et al. (2013) and Roseboom et al. (2013) find a 450 μm redshift distribution which averages $\langle z \rangle = 1.3$, which is statistically different than our finding of $\langle z \rangle = 2.0 \pm 0.2$. Note however that the median distribution of the Geach et al. and Roseboom et al. sample is $z \sim 1.6$, significantly

different than the average, and closer to the median value we measure. The offset between median redshifts between the two samples is likely due to the difference in depths of coverage between our surveys; the Geach et al. and Roseboom et al. work is a factor of $\approx 3\times$ deeper at its centre, while ours is a factor of $\approx 4\times$ larger, so our sample naturally picks up more luminous sources that might sit at higher redshifts than the fainter, lower redshift $450\mu\text{m}$ -population.

Despite the overlap in redshift distribution with $850\mu\text{m}$ sources, 62–76% of $450\mu\text{m}$ sources are not $850\mu\text{m}$ detected. Similarly, 61–81% of $850\mu\text{m}$ sources are not $450\mu\text{m}$ -detected. If the difference is not the sources’ redshifts, then the SED properties could be the cause of the lack of overlap between the galaxy populations. Dust temperature has been thought to cause a significant selection difference between $850\mu\text{m}$ –1 mm and $<500\mu\text{m}$ populations (Blain et al. 2004; Chapman et al. 2004; Casey et al. 2009b), where the former population is biased towards colder temperature SEDs. Before *Herschel* and SCUBA-2, this population of warm-dust high- z ULIRGs was called Optically Faint Radio Galaxies (OFRGs) or Submm-faint, Star-Forming Radio Galaxies (SFRGs), and was shown to exist in Casey et al. (2009b). In this paper, our finding that $850\mu\text{m}$ -only sources are statistically cooler (at a fixed redshift or luminosity) than $450\mu\text{m}$ -only sources is consistent with this hypothesis and is the most prominent difference between $450\mu\text{m}$ -only and $850\mu\text{m}$ -only populations, even though the average SED peak wavelength offset is only $\sim 20\mu\text{m}$ at $z \sim 2$ (information presented in Figure 13).

Certainly the lack of one-to-one overlap in the $450\mu\text{m}$ and $850\mu\text{m}$ -samples implies that systems selected at any one wavelength in the FIR are *not* representative of *all* ultraluminous infrared star formation at high redshift. This becomes an issue when studies try to compare the relative importance of normal galaxies to infrared galaxies in the context of universal star formation and completeness for interpretation of the star formation rate density.

5.2 Relation to ‘Normal’ Galaxies

Recent work has proposed that most submillimeter or infrared-luminous systems are a different, more extreme class of galaxy than most ‘normal’ star forming galaxies in the Universe (e.g. Daddi et al. 2009; Genzel et al. 2010; Tacconi et al. 2010). This distinction is likely valid when speaking of the most luminous subset of SMGs. SMGs at $\approx 10^{13} L_{\odot}$ are nearly all found to be major merger-driven starbursts, much more extreme and much more rare than normal, more modest star forming galaxies at comparable redshifts (e.g. Engel et al. 2010).

Although many SMGs exhibit extreme properties not seen in typical star forming systems, this is not true of the entire infrared-luminous population. Here we measure a mean infrared luminosity of SCUBA-2 galaxies as $\approx 1\text{--}2 \times 10^{12} L_{\odot}$, and the average star formation rates in our sample are $\approx 200 M_{\odot} \text{yr}^{-1}$, which is typical of high mass ($>10^{10} M_{\odot}$) ‘normal’ galaxies at $z \approx 2$. Most normal galaxies at this epoch have specific star formation rates (sSFR) of $1\text{--}10 \text{Gyr}^{-1}$ while SCUBA-2 galaxies span sSFRs from $1\text{--}100 \text{Gyr}^{-1}$, averaging 10Gyr^{-1} at the upper end of sSFRs for normal galaxies. This is consistent with the idea that SMGs,

although rare and extreme systems, can exhibit both properties of ‘normal’ star forming galaxies and extreme starbursts during different stages of evolution (as suggested in the models of Hayward et al. 2013).

Comparing the star formation rates from the UV/optical/near-infrared SED fits (dubbed “SFR_{UV}”) directly with the star formation rates in the far-infrared, there is a substantial discrepancy. Despite the fact that SFR_{UV} is supposedly corrected for the effects of dust extinction, a cap on the maximum extinction introduced in the LE PHARE SED fitting procedure implies that very dust obscured galaxies will have much higher SFR_{IR} than SFR_{UV}. By our measure, SFR_{UV} is underestimating the star formation rate by a factor of $\gtrsim 13$ (where the total SFR can be approximated as SFR_{IR} in infrared-luminous galaxies).

Table 9 gives the LE PHARE-estimated quantities for star formation rate and stellar mass, as derived from the UV through to the near-infrared. These SCUBA-2 sources are known to be unusual in that the *are* directly detected in the infrared, so the discrepancy between star formation rate measurements is not unexpected or new (Rosa-González et al. 2002; Dye et al. 2008; Yun et al. 2012). Nevertheless, the discrepancy should emphasise the need to treat extinction carefully in model fits, especially for infrared-luminous galaxies. This potentially will alter the interpretation of galaxies’ specific star formation rates. A future work, which will summarise our progress in confirming redshifts spectroscopically, will explore the total energy output of these galaxies in more depth and provide more context for comparing the sample to ‘normal’ galaxies.

5.3 Contribution to Universal Star Formation

Here we measure the net contribution of SCUBA-2 galaxies to the star formation rate density (SFRD) of the Universe, or in other words, how significantly they impact net star formation in the Universe at any given epoch.

We compute SFRD estimates for the SCUBA-2 population in this paper using the $1/V_{\text{max}}$ method. Within a redshift bin, we sum each galaxy’s star formation rate divided by accessible volume. Our survey area is roughly uniform over 394arcmin^2 , although individual sources’ accessible volume is computed as a function of the local map noise. Note that we avoid estimating the luminosity functions directly given the limited statistics of this sample, where $\gtrsim 500$ galaxies would be necessary to place accurate constraints in L_{IR} and z . The maximum accessible volume for a source is computed given that sources’ selection wavelength, flux density, and peak wavelength (either measured explicitly or assumed to be $\log \lambda_{\text{peak}} = 2.05$ [$450\mu\text{m}$] or 2.12 [$850\mu\text{m}$] if unconstrained). We split the sample into five redshift bins spanning the range of our data: $0 < z < 1$, $1 < z < 2$, $2 < z < 3$, $3 < z < 4$, and $4 < z < 5$. We exclude the three individual sources which have luminosities $\log L_{\text{IR}} > 13.6$, as they might be contaminated by AGN or could be lensed. Figure 14 shows the results. The black points—representing the total contribution from $450\mu\text{m}$ and $850\mu\text{m}$ sources—should be regarded as lower limits as they only constitute narrow dynamic range in luminosity where our survey is sensitive ($> 3.6\sigma$).

Figure 14 shows us that (a) work done to-date on mea-

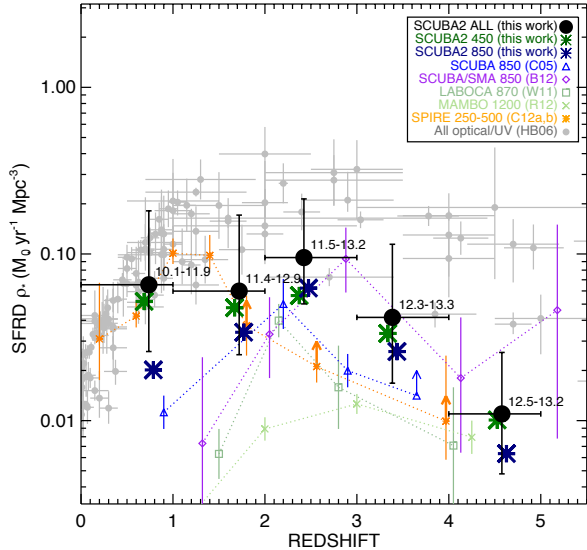


Figure 14. The estimated contribution of SCUBA-2 sources in this paper to the cosmic star formation rate density (SFRD). We split up the contribution estimates by selection wavelength, showing both the contribution from $450\mu\text{m}$ -selected (dark green) and $850\mu\text{m}$ -selected sources (navy), and we compare the total (black points) to literature SFRD values for similarly selected populations. Note that the total SFRD estimate is incomplete and only represents sources characterised at $>3.6\sigma$ in this paper and does not extrapolate to fainter luminosities; thus they should be regarded as lower limits. The range of luminosities represented by each black point is given adjacent to the point, in logarithmic solar luminosities. Galaxies with $\log L_{\text{IR}} > 13.6$ are excluded from this estimate due to potential lensing bias. Literature comparisons are Chapman et al. (2005) $850\mu\text{m}$ -selected SCUBA sources (blue), Barger et al. (2012) SCUBA sources (purple), Wardlow et al. (2011) $870\mu\text{m}$ -selected LABOCA sources (light sea green), the Roseboom et al. (2012) 1.2mm -selected MAMBO sources (light green), and the Casey et al. (2012a,b) *Herschel*-SPIRE $250\text{--}500\mu\text{m}$ -selected sources (orange).

suring the SFRD from infrared/submm samples has been incomplete and is highly dependent on survey depth, but (b) with more multi-wavelength submillimeter surveys—like the SCUBA-2 survey presented herein—we are beginning to see more of the infrared contribution to cosmic star formation which we had not previously seen. This is particularly evident at $z \sim 1\text{--}2$, where $450\mu\text{m}$ -selected galaxies are dominant, while at $z \sim 2\text{--}3$ $450\mu\text{m}$ and $850\mu\text{m}$ -selected galaxies contribute equally, and $850\mu\text{m}$ -selected galaxies might have a more prominent contribution to the SFRD at $z \sim 3$. This survey is conducted at similar depths to previous submillimeter surveys, however it probes more of cosmic infrared-based star formation due to the multiwavelength submillimeter approach. Although deeper, wider surveys are necessary for complete surveys, probing a larger dynamic range in luminosity, there is no doubt that the multi-wavelength selection approach is also necessary, as these SCUBA-2 samples represent a more complete subset of ultraluminous activity at these epochs than single-wavelength selected populations at $850\mu\text{m}\text{--}1.2\text{mm}$.

The contribution from infrared-luminous galaxies ap-

pears 1–10 times less significant than the SFRD contribution from more normal, optical and UV selected galaxies (Hopkins & Beacom 2006). However, here the estimates from Hopkins & Beacom are corrected for dust extinction, in that they are scaled up by a factor proportional to the rest-frame UV slope. As addressed earlier by the discrepancy between optical SED-derived SFR and infrared SFR, there might be cause for concern if the dust extinction is not properly handled for some of the potentially dustier optically-selected galaxies.

6 CONCLUSIONS

With simultaneous mapping at $450\mu\text{m}$ and $850\mu\text{m}$, the SCUBA-2 instrument is making substantial headway in the detection and characterisation of infrared emission in the distant Universe. The $\sim 7''$ high-resolution blank-field mapping at $450\mu\text{m}$ opens up a unique parameter space in high- z submillimeter science, and the efficient mapping at $850\mu\text{m}$ means that the confusion limit is reached in far less time than previous observations. This paper has presented initial SCUBA-2 mapping of a uniformly-covered 394arcmin^2 area in the COSMOS field at both $450\mu\text{m}$ and $850\mu\text{m}$. We reach the following conclusions about our maps and the identification of point sources:

- The root-mean-square (RMS) noise values of our maps are $\sigma_{450} = 4.13\text{mJy}$ and $\sigma_{850} = 0.80\text{mJy}$ at our map centres and find largely uniform RMS over a 22.4arcmin diameter (394arcmin^2), the threshold where the RMS exceeds two times the central RMS value.
- We extract point sources down to a 3.6σ detection threshold at $450\mu\text{m}$ and $850\mu\text{m}$, where we find 78 and 99 sources respectively. These extraction limits are determined via Monte Carlo simulations and an expected sample contamination rates of 3–5%.
- Source number counts at $450\mu\text{m}$ and $850\mu\text{m}$ are measured and we compare them to previous results at both wavelengths. We provide best-fit double-power law and Schechter function fits.
- Positional uncertainties of $1\text{--}2.5''$ at $450\mu\text{m}$ and $2\text{--}6''$ at $850\mu\text{m}$ are estimated using Monte Carlo tests; we use this uncertainty to match both $450\mu\text{m}$ and $850\mu\text{m}$ sources to multiwavelength counterparts. The low positional uncertainties at $450\mu\text{m}$ allow direct matching to counterparts in the optical/near-infrared, without relying on detection at $24\mu\text{m}$ or radio wavelengths. Our $850\mu\text{m}$ counterpart matching is done first by identifying $24\mu\text{m}$ and radio counterparts, then if absent, taken as the nearest neighbour optical source.
- 56% of all $450\mu\text{m}$ galaxies and 40% of all $850\mu\text{m}$ galaxies lack both $24\mu\text{m}$ and radio counterparts down to the deep field detection limits ($S_{24} \approx 80\mu\text{Jy}$ and $S_{1.4} \approx 50\mu\text{Jy}$). This suggests that submillimeter samples relying on identification at either wavelength could be significantly biased, producing up to $\sim 1/2$ mis-identifications.

After analysis of field number counts and counterpart matching techniques, we also analyse the population characteristics of $450\mu\text{m}$ and $850\mu\text{m}$ galaxies, how they differ from one another and how they relate to other high-redshift

galaxy populations. We reach the following conclusions on their physical attributes:

- The redshift distributions for both populations is measured using the extensive COSMOS ancillary optical and near-infrared data. The $450\mu\text{m}$ population peaks at $\langle z \rangle = 1.95 \pm 0.19$ while the $850\mu\text{m}$ population peaks at $\langle z \rangle = 2.16 \pm 0.11$.
- The far-infrared colour of SCUBA-2 sources (measured as $\log(S_{850}/S_{450})$) is found not to evolve significantly with redshift, although $450\mu\text{m}$ identified galaxies have statistically ‘bluer’ far-infrared SEDs than $850\mu\text{m}$ identified galaxies. Both $450\mu\text{m}$ and $850\mu\text{m}$ populations have colours which are inconsistent with a fixed SED peak wavelength (i.e. fixed temperature) across $0 < z < 5$.
- $850\mu\text{m}$ -detected sources which are $450\mu\text{m}$ -dropouts peak at $z \approx 2$ and do not sit at higher redshifts as would be suspected if SED shape were not evolving or changing with infrared luminosity. Similarly $450\mu\text{m}$ -detected sources which are $850\mu\text{m}$ -dropouts also sit at $z \approx 2$ and not at lower redshifts. This is consistent with model populations where there is correlation between luminosity and dust temperatures, although whether or not that correlation evolves with z is unconstrained by this data.
- Infrared luminosities, SED peak wavelengths and dust masses are estimated for both populations, and we determine that $450\mu\text{m}$ galaxies and $850\mu\text{m}$ galaxies are equally luminous and peak at similar rest-frame wavelengths. The most significant distinction is the SED peak wavelength of $450\mu\text{m}$ -only or $850\mu\text{m}$ -only detected galaxies, which differs by $\sim 20\text{--}50\mu\text{m}$ (or $8\text{--}12\text{K}$, with $450\mu\text{m}$ -sources being the warmer subset).
- The star formation rates measured directly in the far-infrared exceed those predicted from UV/optical/near-infrared photometry by ~ 13 times if restrictions are placed on extinction when generating best-fit stellar population fits.
- The contribution of these SCUBA-2 sources to the cosmic infrared luminosity density, or the star formation rate density, is measured to be higher than previous submm surveys, not due to depth, but due to multi-wavelength selection. The $450\mu\text{m}$ and $850\mu\text{m}$ samples complement one another in that they only overlap by $\sim 30\%$, so together they constitute a more complete census of luminous infrared activity than either subset. The total SFRD contribution we measure here is a factor of 2–3 times higher than previous single-wavelength $\sim 850\mu\text{m}$ selection at the same depth. This demonstrates that multiple selection wavelengths are necessary for a complete census of infrared luminous star formation.

SCUBA-2 high-resolution $450\mu\text{m}$ mapping has allowed the first detailed look at an infrared-luminous population not surveyed before. This work has revealed the necessity to exercise caution when identifying multiwavelength counterparts of submillimeter sources (especially those with a large beamsize) and the biases and limitations of previously analysed $850\mu\text{m}\text{--}1\text{mm}$ samples. Direct far-infrared interferometry still proves the best method for unequivocally identifying multiwavelength counterparts, however future work from CCAT will enable large field-of-view mapping with resolution significantly improved over JCMT, both at $850\mu\text{m}$ and $450\mu\text{m}$. This work provides a stepping stone to link

infrared-luminous systems to the more ubiquitous, ‘normal’ star forming galaxies across a wide range of epochs, shedding light on galaxy evolution and the nature of cosmic star formation.

ACKNOWLEDGEMENTS

We would like to thank the referee for a very thoughtful and helpful report in reviewing this manuscript. CMC is generously supported by a Hubble Fellowship from Space Telescope Science Institute, grant HST-HF-51268.01-A. CCC and LC are generously supported by NSF grant AST 0709356. AB thanks the University of Wisconsin Research Committee with funds granted by the Wisconsin Alumni Research Foundation, and the David and Lucile Packard Foundation. CMC and DBS would like to thank the Aspen Center for Physics and the NSF grant 1066293 for many fruitful conversations with the community regarding this work during “The Obscured Universe” summer workshop. The James Clerk Maxwell Telescope is operated by the Joint Astronomy Centre on behalf of the Science and Technology Facilities Council of the United Kingdom, the National Research Council of Canada, and (until 31 March 2013) the Netherlands Organisation for Scientific Research. Additional funds for the construction of SCUBA-2 were provided by the Canada Foundation for Innovation. The authors also wish to recognise and acknowledge the very significant cultural role and reverence that the summit of Mauna Kea has always had within the indigenous Hawaiian community. We are most fortunate to have the opportunity to conduct observations from this mountain.

REFERENCES

- Alaghband-Zadeh S. et al., 2012, MNRAS, 3329
 Alexander D. M., Bauer F. E., Chapman S. C., Smail I., Blain A. W., Brandt W. N., Ivison R. J., 2005, ApJ, 632, 736
 Aretxaga I. et al., 2011, MNRAS, 415, 3831
 Armus L. et al., 2009, PASP, 121, 559
 Banerji M., Chapman S. C., Smail I., Alaghband-Zadeh S., Swinbank A. M., Dunlop J. S., Ivison R. J., Blain A. W., 2011, MNRAS, 418, 1071
 Barger A. J., Cowie L. L., Richards E. A., 2000, AJ, 119, 2092
 Barger A. J., Cowie L. L., Sanders D. B., Fulton E., Taniguchi Y., Sato Y., Kawara K., Okuda H., 1998, Nature, 394, 248
 Barger A. J., Cowie L. L., Smail I., Ivison R. J., Blain A. W., Kneib J., 1999, AJ, 117, 2656
 Barger A. J., Wang W.-H., Cowie L. L., Owen F. N., Chen C.-C., Williams J. P., 2012, ApJ, 761, 89
 Barnard V. E., Vielva P., Pierce-Price D. P. I., Blain A. W., Barreiro R. B., Richer J. S., Qualtrough C., 2004, MNRAS, 352, 961
 Bertin E., Arnouts S., 1996, A&A, 117, 393
 Bertoldi F. et al., 2007, ApJS, 172, 132
 Béthermin M., et al., 2012, A&A, 542

- Blain A. W., Barnard V. E., Chapman S. C., 2003, *MNRAS*, 338, 733
- Blain A. W., Chapman S. C., Smail I., Ivison R., 2004, *ApJ*, 611, 725
- Borys C., Chapman S., Halpern M., Scott D., 2003, *MNRAS*, 344, 385
- Bothwell M. S. et al., 2010, *MNRAS*, 405, 219
- Bruzual G., Charlot S., 2003, *MNRAS*, 344, 1000
- Caputi K. I. et al., 2007, *ApJ*, 660, 97
- Casey C. M., 2012, *MNRAS*, 425, 3094
- Casey C. M. et al., 2012a, *ApJ*, 761, 140
- Casey C. M. et al., 2012b, *ApJ*, 761, 139
- Casey C. M. et al., 2009a, *MNRAS*, 399, 121
- Casey C. M., Chapman S. C., Muxlow T. W. B., Beswick R. J., Alexander D. M., Conselice C. J., 2009b, *MNRAS*, 395, 1249
- Chapin E. L. et al., 2010, *MNRAS*, 1682
- Chapin E. L., Hughes D. H., Aretxaga I., 2009, *MNRAS*, 393, 653
- Chapin E. L., et al., 2013, *MNRAS*, 430, 2545
- Chapman S. C., Blain A. W., Smail I., Ivison R. J., 2005, *ApJ*, 622, 772
- Chapman S. C., Helou G., Lewis G. F., Dale D. A., 2003, *ApJ*, 588, 186
- Chapman S. C., Smail I., Blain A. W., Ivison R. J., 2004, *ApJ*, 614, 671
- Chen C.-C., Cowie L. L., Barger A. J., Casey C. M., Lee N., Sanders D. B., Wang W.-H., Williams J. P., 2013, *ApJ*, 762, 81
- Clements D. L. et al., 2010, *A&A*, 518, L8
- Condon J. J., 1992, *ARA&A*, 30, 575
- Coppin K. et al., 2006, *MNRAS*, 372, 1621
- Coppin K., Halpern M., Scott D., Borys C., Chapman S., 2005, *MNRAS*, 357, 1022
- Coppin K. et al., 2010, *ApJ*, 713, 503
- Coppin K. E. K. et al., 2008, *MNRAS*, 389, 45
- Cowie L. L., Barger A. J., Kneib J.-P., 2002, *AJ*, 123, 2197
- Daddi E. et al., 2009, *ApJ*, 694, 1517
- Dempsy J. T., et al., 2013, *MNRAS*, 430, 2534
- Downes A. J. B., Peacock J. A., Savage A., Carrie D. R., 1986, *MNRAS*, 218, 31
- Dye S. et al., 2008, *MNRAS*, 386, 1107
- Eales S. et al., 2010, *PASP*, 122, 499
- Eales S., Lilly S., Gear W., Dunne L., Bond J. R., Hammer F., Le Fèvre O., Crampton D., 1999, *ApJ*, 515, 518
- Eddington A. S., 1913, *MNRAS*, 73, 359
- Elbaz D. et al., 2011, *A&A*, 533, A119+
- Engel H. et al., 2010, *ApJ*, 724, 233
- Frayer D. T. et al., 2009, *AJ*, 138, 1261
- Geach J. E. et al., 2013, *MNRAS*, 432, 53
- Genzel R. et al., 2010, *MNRAS*, 407, 2091
- Greve T. R. et al., 2005, *MNRAS*, 359, 1165
- Gruppioni C., et al., 2013, *MNRAS*, 432, 23
- Hayward C. C., Behroozi P. S., Somerville R. S., Primack J. R., Moreno J., Wechsler R. H., 2013, *MNRAS*, 434, 2572
- Hayward C. C., Jonsson P., Kereš D., Magnelli B., Hernquist L., Cox T. J., 2012, *MNRAS*, 424, 951
- Helou G., Soifer B. T., Rowan-Robinson M., 1985, *ApJL*, 298, L7
- Hinshaw G. et al., 2009, *ApJS*, 180, 225
- Hodge J. A. et al., 2013, *ApJ*, 768, 91
- Holland W. S. et al., 1999, *MNRAS*, 303, 659
- Holland W. S., et al., 2013, *MNRAS*, 430, 2513
- Hopkins A. M., Beacom J. F., 2006, *ApJ*, 651, 142
- Hughes D. H. et al., 1998, *Nature*, 394, 241
- Hwang H. S., et al., 2010, *MNRAS*, 409
- Ilbert O. et al., 2009, *ApJ*, 690, 1236
- Ilbert O. et al., 2010, *ApJ*, 709, 644
- Ivison R. J. et al., 2010a, *MNRAS*, 402, 245
- Ivison R. J. et al., 2010b, *A&A*, 518, L31+
- Karim A. et al., 2013, *MNRAS*, 432, 2
- Kennicutt, Jr. R. C., 1998a, *ARA&A*, 36, 189
- Kennicutt, Jr. R. C., 1998b, *ApJ*, 498, 541
- Knudsen K. K., van der Werf P. P., Kneib J.-P., 2008, *MNRAS*, 384, 1611
- Kovács A., Chapman S. C., Dowell C. D., Blain A. W., Ivison R. J., Smail I., Phillips T. G., 2006, *ApJ*, 650, 592
- Kovács A. et al., 2010, *ApJ*, 717, 29
- Laird E. S., Nandra K., Pope A., Scott D., 2010, *MNRAS*, 401, 2763
- Le Floch E. et al., 2009, *ApJ*, 703, 222
- Le Floch E. et al., 2005, *ApJ*, 632, 169
- Lee N. et al., 2010, *ApJ*, 717, 175
- Magnelli B., Elbaz D., Chary R. R., Dickinson M., Le Borgne D., Frayer D. T., Willmer C. N. A., 2011, *A&A*, 528, A35
- Menéndez-Delmestre K. et al., 2009, *ApJ*, 699, 667
- Meurer G. R., Heckman T. M., Calzetti D., 1999, *ApJ*, 521, 64
- Neri R. et al., 2003, *ApJL*, 597, L113
- Oliver S. et al., 2010, *MNRAS*, 405, 2279
- Oliver S. J. et al., 2012, *MNRAS*, 424, 1614
- Pilbratt G. L. et al., 2010, *A&A*, 518, L1
- Polletta M. et al., 2007, *ApJ*, 663, 81
- Pope A. et al., 2008, *ApJ*, 675, 1171
- Reddy N. et al., 2012, *ApJ*, 744, 154
- Rodighiero G. et al., 2011, *ApJL*, 739, L40
- Rosa-González D., Terlevich E., Terlevich R., 2002, *MNRAS*, 332, 283
- Roseboom I. G. et al., 2013, *ArXiv e-prints*
- Roseboom I. G. et al., 2012, *MNRAS*, 419, 2758
- Sanders D. B., Mirabel I. F., 1996, *ARA&A*, 34, 749
- Sanders D. B. et al., 2007, *ApJS*, 172, 86
- Sanders D. B., Soifer B. T., Elias J. H., Neugebauer G., Matthews K., 1988, *ApJL*, 328, L35
- Scott K. S. et al., 2008, *MNRAS*, 385, 2225
- Scott S. E. et al., 2002, *MNRAS*, 331, 817
- Scoville N. et al., 2013, *ApJS*, 206, 3
- Scoville N. et al., 2007, *ApJS*, 172, 1
- Serjeant S. et al., 2008, *MNRAS*, 386, 1907
- Smail I., Ivison R. J., Blain A. W., 1997, *ApJL*, 490, L5+
- Smail I., Ivison R. J., Blain A. W., Kneib J., 2002, *MNRAS*, 331, 495
- Smolčić V. et al., 2012, *A&A*, 548, A4
- Soifer B. T., Boehmer L., Neugebauer G., Sanders D. B., 1989, *AJ*, 98, 766
- Soifer B. T., Sanders D. B., Madore B. F., Neugebauer G., Danielson G. E., Elias J. H., Lonsdale C. J., Rice W. L., 1987, *ApJ*, 320, 238
- Swinbank A. M., Smail I., Chapman S. C., Blain A. W., Ivison R. J., Keel W. C., 2004, *ApJ*, 617, 64

- Tacconi L. J. et al., 2010, *Nature*, 463, 781
Tacconi L. J. et al., 2006, *ApJ*, 640, 228
Tacconi L. J., et al., 2008, *ApJ*, 680, 246
Targett T. A., 2011, *MNRAS*
U V. et al., 2012, *ApJS*, 203, 9
Wang W.-H., Cowie L. L., Barger A. J., 2006, *ApJ*, 647, 74
Wang W.-H., Cowie L. L., Barger A. J., Williams J. P.,
2011, *ApJL*, 726, L18
Wardlow J. L. et al., 2011, *MNRAS*, 415, 1479
Webb T. M. et al., 2003, *ApJ*, 582, 6
Wilson C. D. et al., 2008, *ApJS*, 178, 189
Younger J. D. et al., 2007, *ApJ*, 671, 1531
Younger J. D. et al., 2008, *ApJ*, 688, 59
Younger J. D. et al., 2009, *MNRAS*, 394, 1685
Yun M. S. et al., 2012, *MNRAS*, 420, 957

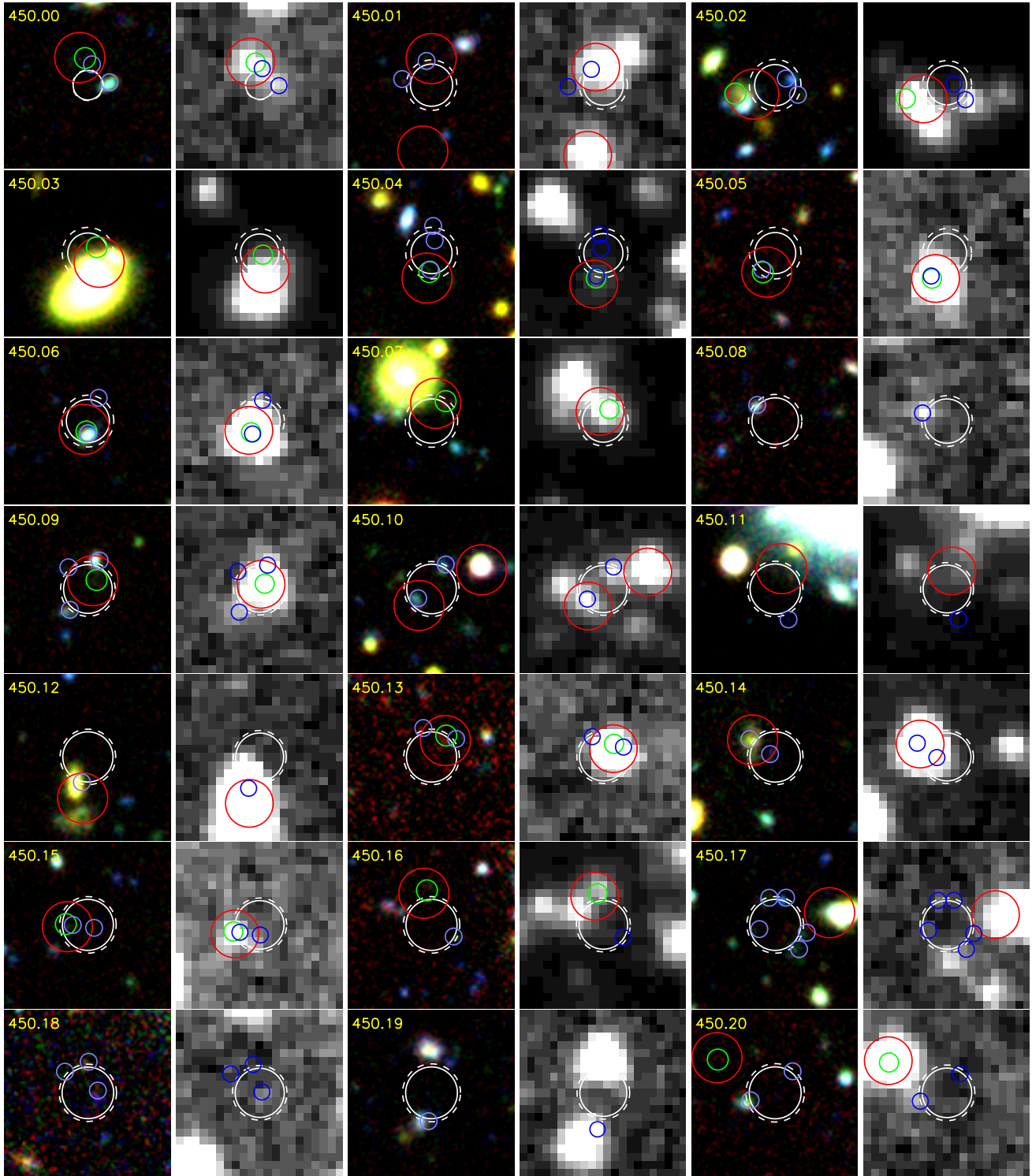


Figure 15. $12'' \times 12''$ cutouts for $450\mu\text{m}$ -detected sources in optical tri-colour (SUBARU B, I, and Z) and *Spitzer*-IRAC $3.6\mu\text{m}$. White solid circles indicate the position of the $450\mu\text{m}$ source with associated positional uncertainty, varying $1.5\text{--}3''$. The outer ring (white dashed circle) corresponds to the 95% confidence interval on position, while the inner is the 90% interval. *Spitzer*-MIPS $24\mu\text{m}$ source positions are marked with red circles and 1.4 GHz source positions are marked with green circles. Optical counterparts are marked with blue circles.

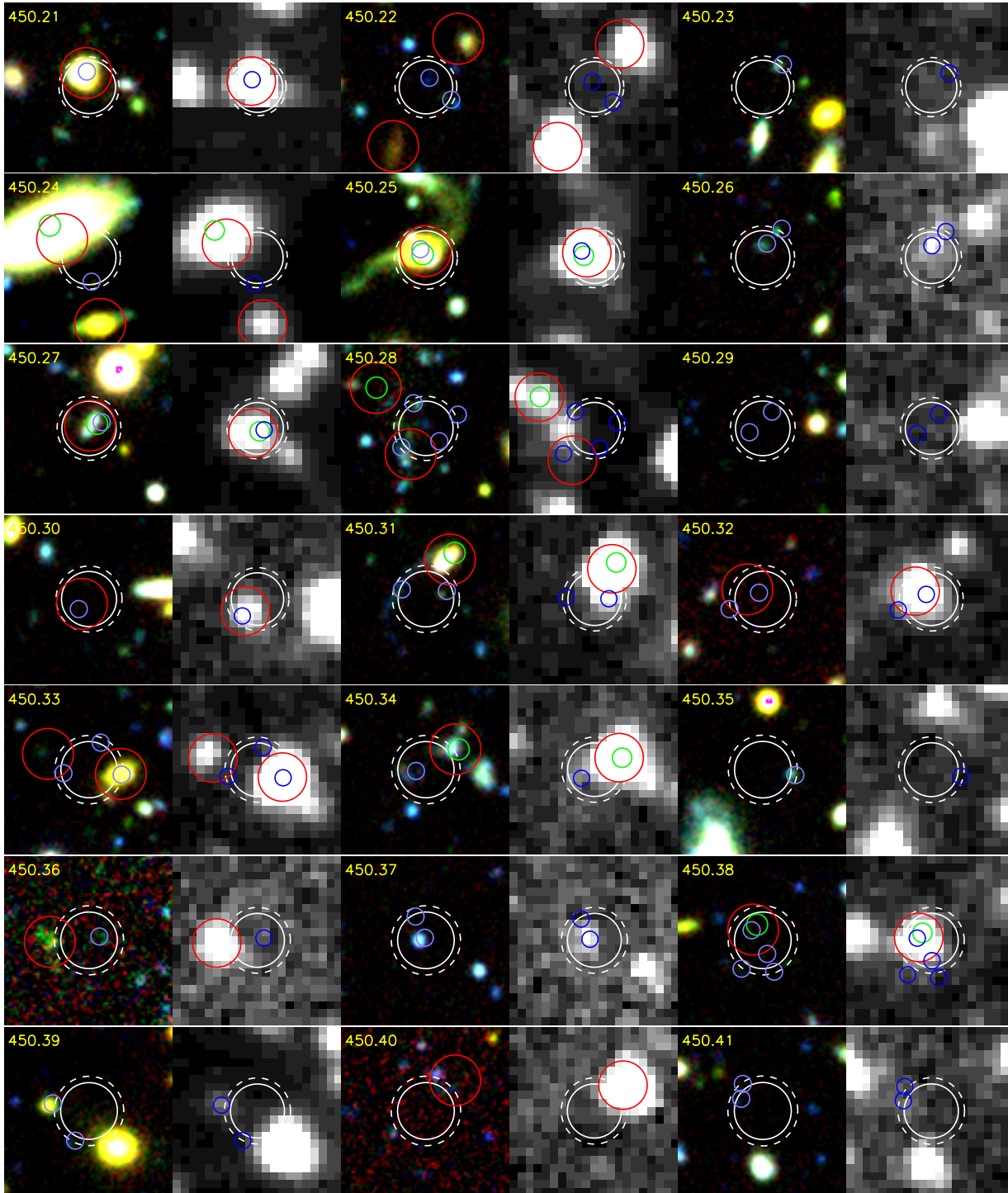


Figure 15 – continued.

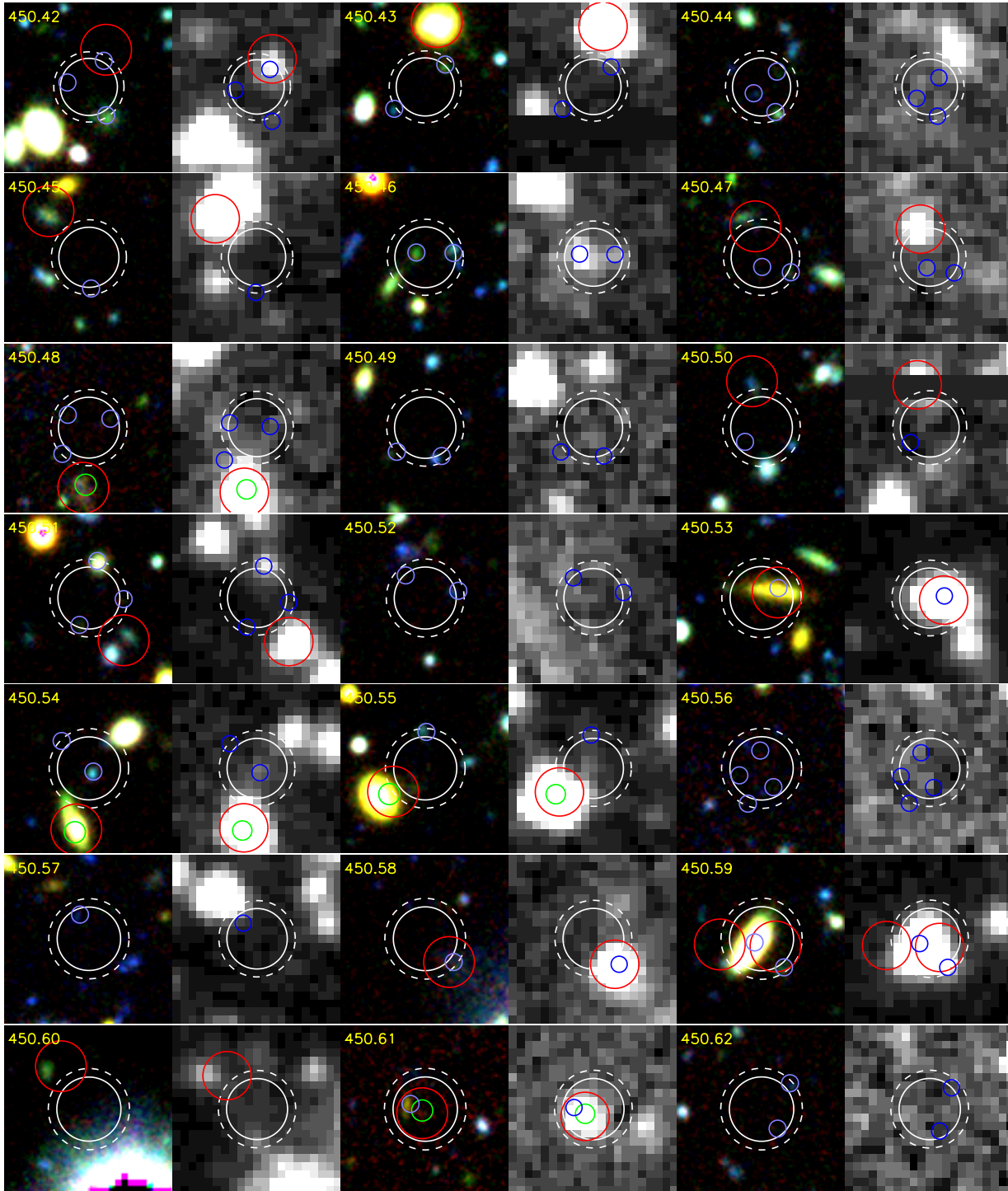


Figure 15 – continued.

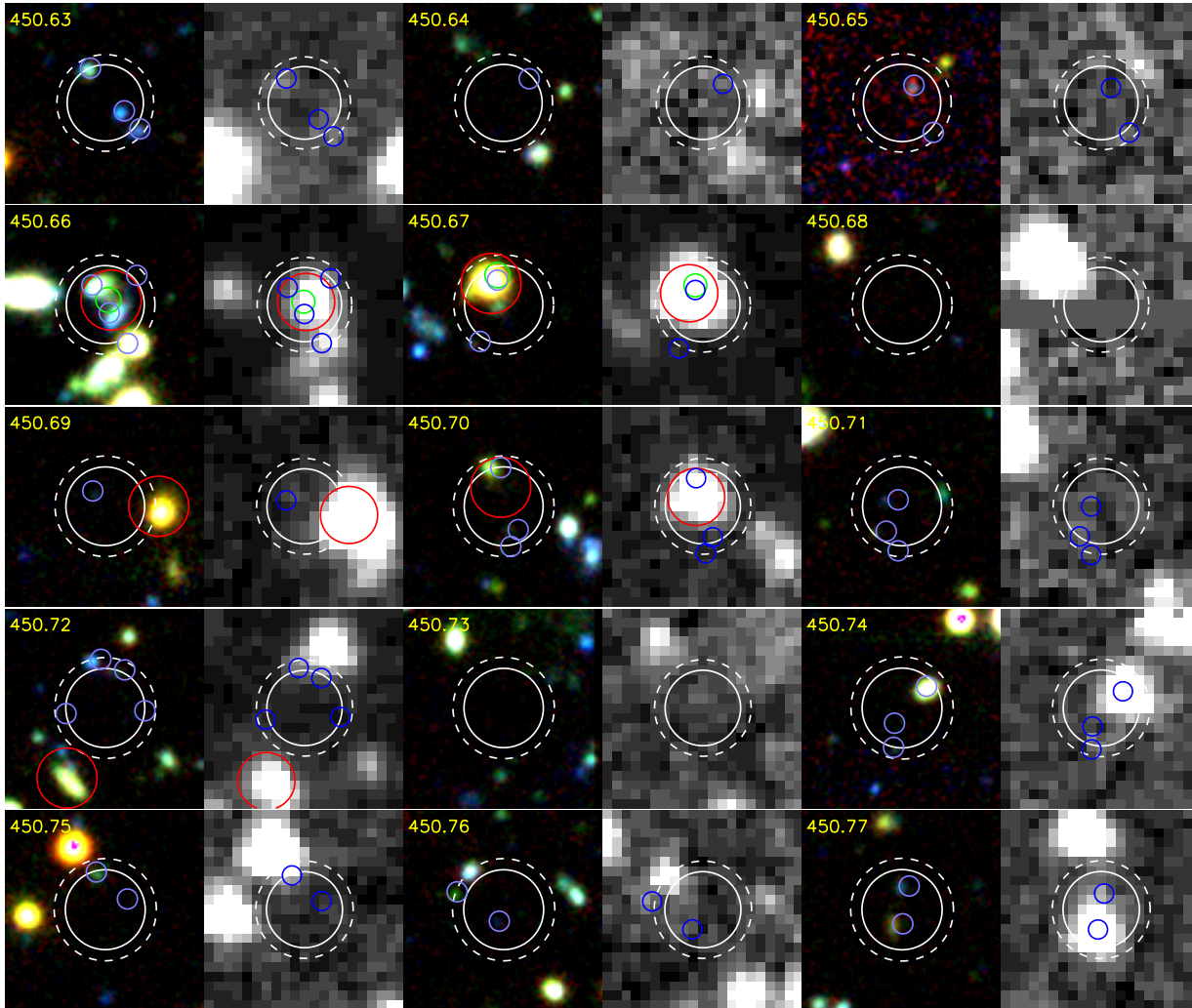


Figure 15 – continued.

Table 5. 850 μm -identified $>3.6\sigma$ point sources in COSMOS.

Name	Short Name	RA ₈₅₀	DEC ₈₅₀	S/N	S ₈₅₀ RAW [mJy]	S ₈₅₀ DEBOOSTED [mJy]	$\Delta(\alpha, \delta)$ [$''$]	P_{contam}	450 μm - SOURCE	Offset [$''$]	S ₄₅₀ RAW [mJy]	S ₄₅₀ DEBOOSTED [mJy]
SMM J100008.0+022612...	850.00	10:00:08.0	02:26:12	20.1	16.15 \pm 0.80	16.15 \pm 0.80	1.19	<0.01	450.03	0.6	23.47 \pm 4.10	20.46 \pm 4.78
SMM J095957.3+022730...	850.01	09:59:57.3	02:27:30	13.0	11.98 \pm 0.92	11.49 \pm 1.10	1.65	<0.01	(450.168)		11.02 \pm 4.75	
SMM J100033.3+022559...	850.02	10:00:33.3	02:25:59	11.8	9.47 \pm 0.80	8.97 \pm 1.04	1.78	<0.01	450.01	0.6	28.43 \pm 4.13	25.62 \pm 4.96
SMM J100019.7+023204...	850.03	10:00:19.7	02:32:04	11.7	12.11 \pm 1.03	11.42 \pm 1.38	1.77	<0.01	450.04	1.5	29.15 \pm 5.19	25.35 \pm 6.04
SMM J100015.5+021550...	850.04	10:00:15.5	02:15:50	10.8	11.80 \pm 1.08	11.09 \pm 1.56	1.85	<0.01			10.67 \pm 5.79	
SMM J100057.0+022014...	850.05	10:00:57.0	02:20:14	10.8	12.24 \pm 1.13	11.49 \pm 1.62	1.85	<0.01	(450.28)		18.48 \pm 5.43	
SMM J100024.0+021750...	850.06	10:00:24.0	02:17:50	10.4	9.30 \pm 0.89	8.64 \pm 1.24	1.88	<0.01	450.55	3.1	17.06 \pm 4.57	12.70 \pm 5.42
SMM J100028.6+023202...	850.07	10:00:28.6	02:32:02	9.41	9.94 \pm 1.06	9.21 \pm 1.45	2.18	<0.01	450.00	0.6	40.58 \pm 5.20	37.54 \pm 6.58
SMM J100023.5+022155...	850.08	10:00:23.5	02:21:55	8.98	7.19 \pm 0.80	6.60 \pm 1.12	2.10	<0.01	450.05	1.9	23.14 \pm 4.12	20.12 \pm 4.80
SMM J100025.3+021847...	850.09	10:00:25.3	02:18:47	8.89	7.47 \pm 0.84	6.83 \pm 1.17	2.10	<0.01	450.87	2.8	15.24 \pm 4.30	10.74 \pm 5.24
SMM J100034.4+022121...	850.10	10:00:34.4	02:21:21	8.61	6.90 \pm 0.80	6.24 \pm 1.13	2.12	<0.01	450.81	0.8	14.71 \pm 4.11	10.47 \pm 4.98
SMM J100049.9+022257...	850.11	10:00:49.9	02:22:57	8.59	7.51 \pm 0.87	6.79 \pm 1.24	2.12	<0.01			5.94 \pm 4.41	
SMM J100039.1+022221...	850.12	10:00:39.1	02:22:21	8.14	6.49 \pm 0.80	5.83 \pm 1.13	2.10	<0.01	450.06	1.3	22.29 \pm 4.11	19.32 \pm 4.76
SMM J100024.1+022005...	850.13	10:00:24.1	02:20:05	8.00	6.44 \pm 0.80	5.76 \pm 1.13	2.12	<0.01			8.53 \pm 4.13	
SMM J100010.2+022221...	850.14	10:00:10.2	02:22:21	7.81	6.25 \pm 0.80	5.55 \pm 1.11	2.17	<0.01	450.38	2.8	16.47 \pm 4.12	12.91 \pm 4.73
SMM J100025.2+022607...	850.15	10:00:25.2	02:26:07	7.26	5.79 \pm 0.80	5.08 \pm 1.09	2.30	<0.01			11.51 \pm 4.11	
SMM J100103.9+022447...	850.16	10:01:03.9	02:24:47	7.12	8.94 \pm 1.25	7.82 \pm 1.71	2.34	<0.01			14.52 \pm 5.92	
SMM J100000.4+022256...	850.17	10:00:00.4	02:22:56	7.01	5.88 \pm 0.84	5.14 \pm 1.14	2.39	<0.01			8.96 \pm 4.28	
SMM J100024.0+022947...	850.18	10:00:24.0	02:29:47	6.85	5.87 \pm 0.86	5.13 \pm 1.16	2.45	<0.01			6.37 \pm 4.36	
SMM J100015.7+022445...	850.19	10:00:15.7	02:24:45	6.74	5.40 \pm 0.80	4.71 \pm 1.08	2.48	<0.01			2.13 \pm 4.13	
SMM J100027.0+023137...	850.20	10:00:27.0	02:31:37	6.64	6.69 \pm 1.01	5.83 \pm 1.36	2.51	<0.01			3.93 \pm 5.00	
SMM J100035.9+022151...	850.21	10:00:35.9	02:21:51	6.60	5.29 \pm 0.80	4.60 \pm 1.08	2.52	<0.01	450.58	3.6	15.32 \pm 4.12	11.35 \pm 4.90
SMM J100018.7+021655...	850.22	10:00:18.7	02:16:55	6.25	6.05 \pm 0.97	5.15 \pm 1.28	2.69	<0.01			10.34 \pm 5.10	
SMM J100022.1+022842...	850.23	10:00:22.1	02:28:42	6.25	5.06 \pm 0.81	4.31 \pm 1.07	2.69	<0.01	450.94	0.6	14.67 \pm 4.19	10.14 \pm 5.17
SMM J100004.8+023045...	850.24	10:00:04.8	02:30:45	6.20	6.26 \pm 1.01	5.32 \pm 1.34	2.69	<0.01	(450.20)		11.37 \pm 5.23	
SMM J100012.5+021444...	850.25	10:00:12.5	02:14:44	6.15	7.93 \pm 1.29	6.72 \pm 1.70	2.69	<0.01			14.85 \pm 6.90	
SMM J100010.3+022627...	850.26	10:00:10.3	02:26:27	6.09	4.87 \pm 0.80	4.12 \pm 1.06	2.69	<0.01	450.32	3.0	16.86 \pm 4.11	13.37 \pm 4.67
SMM J100023.5+021918...	850.27	10:00:23.5	02:19:18	6.09	5.00 \pm 0.82	4.23 \pm 1.08	2.69	<0.01	450.215	2.7	13.05 \pm 4.20	7.48 \pm 5.28
SMM J100004.3+022059...	850.28	10:00:04.3	02:20:59	5.79	4.86 \pm 0.84	4.07 \pm 1.08	2.76	<0.01	450.15	1.8	19.92 \pm 4.33	16.53 \pm 4.88
SMM J100050.1+022615...	850.29	10:00:50.1	02:26:15	5.70	5.13 \pm 0.90	4.28 \pm 1.15	2.79	<0.01			10.89 \pm 4.50	
SMM J100006.7+022209...	850.30	10:00:06.7	02:22:09	5.69	4.58 \pm 0.80	3.82 \pm 1.03	2.79	<0.01			3.90 \pm 4.15	
SMM J100026.1+021741...	850.31	10:00:26.1	02:17:41	5.57	5.02 \pm 0.90	4.19 \pm 1.14	2.84	<0.01			12.34 \pm 4.62	
SMM J100001.5+022429...	850.32	10:00:01.5	02:24:29	5.56	4.56 \pm 0.82	3.81 \pm 1.04	2.84	<0.01	(450.13)		13.33 \pm 4.20	
SMM J095950.7+022827...	850.33	09:59:50.7	02:28:27	5.55	6.20 \pm 1.12	5.18 \pm 1.41	2.85	<0.01	450.99	3.7	20.15 \pm 5.80	13.76 \pm 7.20
SMM J100016.4+022638...	850.34	10:00:16.4	02:26:38	5.49	4.41 \pm 0.80	3.68 \pm 1.01	2.86	<0.01	450.09	2.3	20.41 \pm 4.14	17.26 \pm 4.68
SMM J100105.1+022150...	850.35	10:01:05.1	02:21:50	5.47	6.02 \pm 1.39	6.35 \pm 1.74	2.87	<0.01			0.38 \pm 6.54	
SMM J100001.3+021745...	850.36	10:00:01.3	02:17:45	5.39	5.60 \pm 1.04	4.68 \pm 1.30	2.90	<0.01			0.09 \pm 5.62	
SMM J100035.6+022826...	850.37	10:00:35.6	02:28:26	5.38	4.45 \pm 0.83	3.72 \pm 1.03	2.91	<0.01			1.74 \pm 4.25	
SMM J100023.5+021536...	850.38	10:00:23.5	02:15:36	5.22	5.67 \pm 1.09	4.72 \pm 1.34	2.99	<0.01			13.39 \pm 5.74	
SMM J100012.1+022310...	850.39	10:00:12.1	02:23:10	5.21	4.17 \pm 0.80	3.47 \pm 0.99	2.99	<0.01			10.53 \pm 4.13	
SMM J100013.5+022227...	850.40	10:00:13.5	02:22:27	5.20	4.16 \pm 0.80	3.47 \pm 0.99	3.00	<0.01	450.252	3.7	12.57 \pm 4.14	6.91 \pm 5.15
SMM J100025.4+022544...	850.41	10:00:25.4	02:25:44	5.17	4.12 \pm 0.80	3.43 \pm 0.98	3.01	<0.01	450.11	2.0	19.57 \pm 4.11	16.40 \pm 4.62
SMM J100017.2+022519...	850.42	10:00:17.2	02:25:19	5.14	4.12 \pm 0.80	3.43 \pm 0.99	3.02	<0.01	450.17	2.6	19.01 \pm 4.14	15.76 \pm 4.67
SMM J100026.3+021528...	850.43	10:00:26.3	02:15:28	5.02	5.55 \pm 1.11	4.60 \pm 1.35	3.10	<0.01			2.32 \pm 5.82	
SMM J100018.2+022249...	850.44	10:00:18.2	02:22:49	5.00	3.99 \pm 0.80	3.31 \pm 0.97	3.10	<0.01			3.93 \pm 4.12	
SMM J100006.9+022047...	850.45	10:00:06.9	02:20:47	4.99	4.12 \pm 0.83	3.42 \pm 1.01	3.11	<0.01			3.79 \pm 4.25	
SMM J100025.4+021506...	850.46	10:00:25.4	02:15:06	4.85	5.62 \pm 1.16	4.64 \pm 1.40	3.20	<0.01	(450.08)		21.40 \pm 6.11	
SMM J095952.3+022137...	850.47	09:59:52.3	02:21:37	4.83	4.74 \pm 0.98	3.92 \pm 1.19	3.21	<0.01	450.50	3.6	19.82 \pm 5.25	14.90 \pm 6.19
SMM J100037.0+021942...	850.48	10:00:37.0	02:19:42	4.83	3.99 \pm 0.83	3.30 \pm 1.00	3.22	<0.01	450.42	3.6	16.71 \pm 4.24	13.01 \pm 4.89
SMM J100005.0+021719...	850.49	10:00:05.0	02:17:19	4.80	4.91 \pm 1.02	4.05 \pm 1.24	3.23	<0.01	450.193	0.6	17.40 \pm 5.50	10.27 \pm 6.95
SMM J100009.1+022023...	850.50	10:00:09.1	02:20:23	4.78	3.94 \pm 0.82	3.25 \pm 1.00	3.25	<0.01			4.68 \pm 4.23	
SMM J095956.4+021854...	850.51	09:59:56.4	02:18:54	4.74	4.94 \pm 1.04	4.06 \pm 1.26	3.27	<0.01			9.29 \pm 5.61	
SMM J100011.9+022937...	850.52	10:00:11.9	02:29:37	4.74	4.09 \pm 0.86	3.37 \pm 1.04	3.28	<0.01	450.134	1.7	14.45 \pm 4.36	9.26 \pm 5.50
SMM J100011.4+021508...	850.53	10:00:11.4	02:15:08	4.68	5.72 \pm 1.22	4.70 \pm 1.47	3.32	<0.01	450.206	4.8	20.69 \pm 6.60	12.04 \pm 8.32
SMM J095948.9+022748...	850.54	09:59:48.9	02:27:48	4.55	5.10 \pm 1.12	4.17 \pm 1.35	3.41	<0.01			0.47 \pm 5.90	
SMM J095950.9+022742...	850.55	09:59:50.9	02:27:42	4.52	4.77 \pm 1.06	3.89 \pm 1.27	3.43	<0.01	450.86	3.6	19.80 \pm 5.58	13.95 \pm 6.80
SMM J100005.1+021526...	850.56	10:00:05.1	02:15:26	4.42	5.69 \pm 1.29	4.63 \pm 1.54	3.58	0.02			-4.70 \pm 6.84	
SMM J100006.8+023307...	850.57	10:00:06.8	02:33:07	4.35	5.94 \pm 1.36	4.82 \pm 1.63	3.68	0.02			3.66 \pm 7.17	
SMM J100101.3+022800...	850.58	10:01:01.3	02:28:00	4.33	5.67 \pm 1.31	4.60 \pm 1.57	3.71	0.03	450.36	3.8	24.27 \pm 6.07	19.03 \pm 6.96
SMM J100000.7+022001...	850.59	10:00:00.7	02:20:01	4.32	3.92 \pm 0.91	3.18 \pm 1.08	3.72	0.03			2.88 \pm 4.76	
SMM J100000.7+022740...	850.60	10:00:00.7	02:27:40	4.32	3.79 \pm 0.88	3.07 \pm 1.05	3.73	0.03			11.26 \pm 4.49	
SMM J100002.0+022820...	850.61	10:00:02.0	02:28:20	4.31	3.83 \pm 0.89	3.10 \pm 1.06	3.73	0.03			11.06 \pm 4.53	
SMM J100031.0+022751...	850.62	10:00:31.0	02:27:51	4.29	3.46 \pm 0.81	2.80 \pm 0.96	3.76	0.03	450.78	0.9	14.94 \pm 4.15	10.72 \pm 4.99
SMM J095953.3+021850...	850.63	09:59:53.3	02:18:50	4.28	4.77 \pm 1.11	3.86 \pm 1.33	3.78	0.03			3.99 \pm 6.07	
SMM J100000.6+022137...	850.64	10:00:00.6	02:21:37	4.18	3.59 \pm 0.86	2.89 \pm 1.02	3.95	0.04			4.27 \pm 4.41	
SMM J100059.2+022108...	850.65	10:00:59.2	02:21:08	4.15	4.71 \pm 1.14	3.79 \pm 1.35	4.04	0.04			2.93 \pm 5.46	
SMM J100024.4+022831...	850.66	10:00:24.4	02:28:31	4.09	3.30 \pm 0.81	2.64 \pm						

Name	Short Name	RA ₈₅₀	DEC ₈₅₀	S/N	S ₈₅₀ RAW [mJy]	S ₈₅₀ DEBOOSTED [mJy]	$\Delta(\alpha, \delta)$ ['']	P_{contam}	450 μm - SOURCE	Offset ['']	S ₄₅₀ RAW [mJy]	S ₄₅₀ DEBOOSTED [mJy]
SMM J100014.1+022704...	850.80	10:00:14.1	02:27:04	3.81	3.06±0.80	2.39±0.96	5.06	0.10			0.71±4.13	<12.40
SMM J095959.0+022441...	850.81	09:59:59.0	02:24:41	3.80	3.21±0.84	2.51±1.01	5.10	0.10			-1.34±4.32	<12.97
SMM J100054.8+021945...	850.82	10:00:54.8	02:19:45	3.78	4.14±1.09	3.22±1.32	5.20	0.11			7.10±5.30	<15.91
SMM J100010.2+021759...	850.83	10:00:10.2	02:17:59	3.77	3.52±0.93	2.74±1.12	5.22	0.11	450.166	1.8	15.87±4.90	9.79±6.20
SMM J100041.8+022111...	850.84	10:00:41.8	02:21:11	3.75	3.07±0.82	2.39±0.99	5.32	0.11			8.93±4.19	<12.57
SMM J100025.0+022753...	850.85	10:00:25.0	02:27:53	3.73	2.99±0.80	2.32±0.97	5.40	0.12	450.105	4.5	14.24±4.14	9.60±5.16
SMM J100101.3+022439...	850.86	10:01:01.3	02:24:39	3.73	4.23±1.13	3.28±1.37	5.41	0.12			-0.42±5.41	<16.22
SMM J100040.3+021758...	850.87	10:00:40.3	02:17:58	3.70	3.49±0.94	2.70±1.14	5.55	0.13			4.66±4.74	<14.22
SMM J100022.2+023026...	850.88	10:00:22.2	02:30:26	3.70	3.31±0.90	2.56±1.08	5.56	0.13	450.179	6.8	14.51±4.52	8.80±5.73
SMM J100020.2+021727...	850.89	10:00:20.2	02:17:27	3.69	3.41±0.92	2.63±1.11	5.60	0.13			10.84±4.77	<14.32
SMM J100032.8+023049...	850.90	10:00:32.8	02:30:49	3.68	3.52±0.96	2.71±1.16	5.64	0.13	450.40	5.0	19.15±4.81	14.98±5.53
SMM J100027.8+022554...	850.91	10:00:27.8	02:25:54	3.67	2.93±0.80	2.26±0.96	5.66	0.13			6.82±4.10	<12.30
SMM J100041.8+022404...	850.92	10:00:41.8	02:24:04	3.67	2.94±0.80	2.27±0.97	5.66	0.13	450.106	5.6	14.19±4.13	9.57±5.15
SMM J100056.7+022945...	850.93	10:00:56.7	02:29:45	3.67	4.80±1.31	3.69±1.58	5.68	0.14			2.09±6.13	<18.38
SMM J100002.6+021632...	850.94	10:00:02.6	02:16:32	3.65	4.21±1.15	3.23±1.39	5.77	0.14			-1.62±6.22	<18.67
SMM J095959.9+022705...	850.95	09:59:59.9	02:27:05	3.65	3.18±0.87	2.44±1.05	5.77	0.14			6.96±4.46	<13.38
SMM J100026.4+022315...	850.96	10:00:26.4	02:23:15	3.64	2.93±0.80	2.24±0.97	5.81	0.14	450.54	8.1	15.46±4.13	11.51±4.90
SMM J100013.4+021807...	850.97	10:00:13.4	02:18:07	3.61	3.27±0.90	2.50±1.09	5.91	0.15			5.64±4.69	<14.08
SMM J100014.5+023008...	850.98	10:00:14.5	02:30:08	3.61	3.18±0.88	2.43±1.07	5.95	0.15			-6.89±4.43	<13.30

TABLE 5 – CONTINUED.

NAME	COUNTER-PART #	<i>p-val</i>	RA ₂₄	DEC ₂₄	δ_{24} ["]	S_{24} [μ Jy]	RA _{1.4}	DEC _{1.4}	$\delta_{1.4}$ ["]	$S_{1.4}$ [μ Jy]	RA _{opt}	DEC _{opt}	δ_{opt} ["]	<i>i</i> [AB-mag]	3.6 μ m [AB-mag]	<i>z</i> _{phot}
450.46	1/2	0.02									10:00:32.46	+02:21:49.1	0.74	24.77	22.16	3.06
	2/2	0.14									10:00:32.29	+02:21:49.0	2.01	24.69	22.49	2.73
450.47	1/3	0.02	10:00:25.24	+02:19:32.9	2.24	84 \pm 15					10:00:25.26	+02:19:33.1	2.47	—	—	—
	2/3	0.02									10:00:25.21	+02:19:30.1	0.68	28.22	24.39	2.77
	3/3	0.19									10:00:25.07	+02:19:29.7	2.36	25.87	24.60	3.03
450.48	1/3	0.09									10:00:09.37	+02:22:24.3	1.62	—	24.43	—
	2/3	0.11									10:00:09.57	+02:22:24.6	1.75	27.38	23.47	—
	3/3	0.23									10:00:09.60	+02:22:21.8	2.68	27.17	23.17	—
450.49	1/2	0.17									09:59:59.98	+02:25:22.7	2.28	25.41	24.16	1.70
	2/2	0.23									10:00:00.20	+02:25:23.0	2.68	26.21	—	2.55
450.50	1/2	0.40									09:59:52.33	+02:21:32.7	1.53	27.79	—	—
	2/2	0.48									09:59:52.21	+02:21:35.3	1.75	—	—	—
450.51	1/3	0.13									10:00:44.41	+02:23:11.9	1.95	25.56	23.87	1.58
	2/3	0.21									10:00:44.20	+02:23:13.7	2.50	26.22	22.57	2.58
	3/3	0.25									10:00:44.32	+02:23:16.4	2.77	23.29	21.72	0.97
450.52	NA															
450.53	1/1	0.007	10:00:10.33	+02:20:27.1	1.19	413 \pm 15					10:00:10.32	+02:20:27.4	1.36	22.95	19.03	1.01
450.54	1/2	0.006									10:00:26.86	+02:23:18.5	0.40	24.82	22.74	1.90
	2/2	0.24									10:00:27.01	+02:23:20.7	2.73	27.04	24.52	2.01
450.55	1/2	0.04	10:00:23.96	+02:17:50.1	2.78	162 \pm 17					10:00:24.01	+02:17:50.3	3.26	—	—	—
	2/2	0.22									10:00:23.81	+02:17:54.3	2.60	24.73	22.64	2.60
450.56	1/3	0.30									09:59:59.40	+02:30:02.0	1.29	26.49	—	2.82
	2/3	0.40									09:59:59.34	+02:29:59.4	1.54	26.06	—	3.18
	3/3	0.46									09:59:59.50	+02:30:00.2	1.69	26.82	—	1.94
450.57	1/1	0.11									10:00:32.46	+02:18:04.4	1.79	28.59	21.85	3.48
450.58	1/1	0.02	10:00:36.05	+02:21:51.1	2.28	194 \pm 17					10:00:36.03	+02:21:51.1	2.53	24.47	20.79	—
450.59	1/2	0.005	10:00:19.35	+02:20:24.2	1.08	197 \pm 52					10:00:19.44	+02:20:24.5	0.61	20.61	19.60	0.47
	2/2	0.04	10:00:19.61	+02:20:24.3	3.05	86 \pm 15					—	—	—	—	—	—
450.60	NA															
450.61	1/1	2×10^{-5}	10:00:18.76	+02:28:13.5	0.32	136 \pm 13	10:00:18.76	+02:28:13.7	0.20	92 \pm 11	10:00:18.81	+02:28:14.1	1.11	25.04	21.88	4.58
450.62	1/1	0.47									10:00:47.23	+02:20:48.4	1.71	27.78	—	1.95
450.63	1/3	0.05									10:00:19.94	+02:21:29.2	1.20	25.09	24.02	2.36
	2/3	0.17									10:00:20.07	+02:21:31.8	2.25	24.40	23.74	2.84
	3/3	0.22									10:00:19.87	+02:21:28.1	2.58	25.19	24.42	1.56
450.64	NA															
450.65	1/1	0.30									10:00:27.23	+02:24:49.8	1.29	25.42	—	0.70
450.66	1/4	8×10^{-5}	10:01:04.63	+02:26:34.0	0.47	586 \pm 24	10:01:04.64	+02:26:34.0	0.38	86 \pm 11	10:01:04.63	+02:26:33.2	0.51	23.20	20.54	—
	2/4	0.07									10:01:04.70	+02:26:34.9	1.45	22.59	20.44	—
	3/4	0.22									10:01:04.53	+02:26:35.5	2.60	25.94	22.14	—
	4/4	0.23									10:01:04.56	+02:26:31.4	2.64	21.86	20.50	—
450.67	1/2	0.002	10:00:00.37	+02:29:03.9	1.43	538 \pm 15	10:00:00.35	+02:29:04.4	1.76	114 \pm 14	10:00:00.35	+02:29:04.1	1.47	21.37	19.06	0.93
	2/2	0.23									10:00:00.42	+02:29:00.5	2.64	25.83	23.47	1.67
450.68	NA															
450.69	1/2	0.05									10:00:47.55	+02:25:21.6	1.16	26.82	23.67	2.04
	2/2	0.05									10:00:47.27	+02:25:20.3	3.45	22.28	19.36	0.95
450.70	1/2	0.006	10:00:47.29	+02:25:20.7	3.20	251 \pm 14					09:59:52.66	+02:27:14.0	2.30	23.77	21.06	3.03
	2/2	0.10									09:59:52.59	+02:27:10.3	1.67	26.17	22.47	2.89
450.71	1/1	0.006									09:59:46.40	+02:29:32.0	0.42	26.81	24.22	1.95
450.72	1/2	0.20									09:59:50.44	+02:20:18.9	2.48	25.61	22.92	1.43
	2/2	0.26									09:59:50.54	+02:20:19.6	2.87	24.92	23.11	1.72
450.73	NA															
450.74	1/2	0.13									10:00:41.26	+02:16:42.1	1.96	22.79	21.36	0.75
	2/2	0.19									10:00:41.39	+02:16:39.9	0.99	26.45	—	0.96
450.75	1/2	0.08									10:00:34.20	+02:34:22.4	1.48	26.81	24.79	2.26
	2/2	0.18									10:00:34.33	+02:34:24.0	2.32	—	23.01	—
450.76	1/2	0.02									10:00:21.76	+02:31:14.0	0.77	31.02	24.83	1.96
	2/2	0.27									10:00:21.93	+02:31:15.7	2.92	25.27	23.61	0.73
450.77	1/2	0.03									09:59:52.65	+02:22:57.8	0.92	25.12	21.05	1.43
	2/2	0.07									09:59:52.62	+02:23:00.0	1.41	25.64	22.35	1.65

TABLE 6 CONTINUED.

Table 7. Counterpart identifications and Multiwavelength Properties for marginal SCUBA-2 450 μ m- and 850 μ m-detected Sources

NAME	COUNTER- PART #	p - val	RA ₂₄	DEC ₂₄	δ_{24} [$''$]	S_{24} [μ Jy]	RA _{1.4}	DEC _{1.4}	$\delta_{1.4}$ [$''$]	$S_{1.4}$ [μ Jy]	RA _{opt}	DEC _{opt}	δ_{opt} [$''$]	i [AB-mag]	3.6 μ m [AB-mag]	z_{phot}
450.78/850.62	1/2	0.006									10:00:31.05	+02:27:51.8	0.40	27.35	22.40	—
	2/2	0.21									10:00:31.05	+02:27:54.2	2.55	26.26	24.53	—
450.81/850.10	1/3	2×10^{-5}	10:00:34.33	+02:21:21.4	0.53	130 \pm 17	10:00:34.37	+02:21:21.6	0.21	517 \pm 23	10:00:34.33	+02:21:21.0	0.76	25.34	21.78	1.75
	2/3	0.19									10:00:34.43	+02:21:19.6	2.36	25.18	23.21	1.66
	3/3	0.27									10:00:34.53	+02:21:20.2	2.94	25.61	23.80	1.95
450.86/850.55	1/2	0.06									09:59:50.90	+02:27:44.6	1.34	25.86	23.56	3.59
	2/2	0.15									09:59:50.97	+02:27:46.7	2.07	26.80	24.16	3.69
450.87/850.09	1/2	0.004	10:00:25.29	+02:18:45.9	2.76	204 \pm 29	10:00:25.28	+02:18:46.2	2.53	58 \pm 12	10:00:25.32	+02:18:46.3	2.98	26.22	21.45	2.71
	2/2	0.12									10:00:25.20	+02:18:46.0	1.90	26.82	21.87	4.85
450.94/850.23	1/3	0.03									10:00:22.26	+02:28:43.2	0.83	21.82	20.20	0.71
	2/3	0.03	10:00:22.12	+02:28:44.8	2.50	128 \pm 15					10:00:22.04	+02:28:43.9	2.92	24.18	20.44	3.34
	3/3	0.27									10:00:22.32	+02:28:45.2	2.95	24.83	24.95	0.52
450.96/850.133	1/1	0.26									10:00:49.95	+02:24:51.0	2.85	26.67	22.93	2.34
450.99/850.33	1/4	0.02	09:59:50.90	+02:28:22.5	2.19	217 \pm 15					09:59:50.86	+02:28:22.4	1.77	26.18	21.21	2.16
	2/4	0.06									09:59:50.69	+02:28:23.8	1.30	27.43	22.86	2.15
	3/4	0.19									09:59:50.64	+02:28:22.5	2.38	26.51	23.82	1.82
	4/4	0.29									09:59:50.78	+02:28:26.7	3.03	26.75	24.02	2.33
450.103/850.128	1/1	0.42									10:00:18.42	+02:23:59.3	3.87	23.82	21.86	1.54
450.105/850.85	1/1	0.03	10:00:25.19	+02:27:55.8	2.58	173 \pm 13					10:00:25.17	+02:27:56.0	2.20	22.82	19.21	—
450.106/850.92	1/1	0.44									10:00:42.08	+02:23:59.8	3.95	23.33	20.67	1.00
450.126/850.159	1/1	0.32									10:00:25.70	+02:30:51.2	1.33	26.35	—	2.04
450.133/850.131	1/4	0.03	10:00:29.67	+02:21:29.6	2.74	518 \pm 16					10:00:29.68	+02:21:29.8	2.68	20.30	18.51	0.93
	2/4	0.16									10:00:29.60	+02:21:33.8	2.14	26.21	23.39	2.61
	3/4	0.22									10:00:29.68	+02:21:33.5	2.61	26.63	23.34	1.43
	4/4	0.36									10:00:29.46	+02:21:35.0	3.49	25.41	24.20	0.46
450.134/850.52	1/1	0.0002	10:00:11.87	+02:29:35.9	0.20	110 \pm 16					10:00:11.82	+02:29:35.3	0.77	—	—	—
	2/4	0.19									10:00:11.82	+02:29:33.5	2.36	25.99	22.11	2.89
	3/4	0.21									10:00:12.02	+02:29:34.7	2.51	27.82	23.50	2.54
	4/4	0.30									10:00:11.86	+02:29:38.9	3.14	28.49	23.70	4.60
450.135/850.163	1/4	0.01	09:59:52.96	+02:26:42.7	1.64	340 \pm 14					09:59:52.95	+02:26:42.8	1.83	24.45	21.04	1.68
	2/4	0.05									09:59:52.92	+02:26:40.3	2.46	25.88	23.47	3.06
	3/4	0.08									09:59:53.12	+02:26:40.7	1.46	26.10	24.50	1.11
	4/4	0.20									09:59:53.18	+02:26:42.6	2.10	25.67	24.00	0.66
450.166/850.83	1/2	0.14									10:00:10.34	+02:17:57.3	3.31	23.38	22.20	0.93
	2/2	0.33									10:00:10.17	+02:17:59.7	1.12	26.71	21.35	3.25
450.173/850.104	1/1	0.002	10:00:05.38	+02:25:16.1	0.67	260 \pm 20					10:00:05.31	+02:25:15.7	1.67	21.55	19.92	1.01
	2/3	0.27									10:00:05.23	+02:25:18.2	2.93	24.67	22.75	1.09
	3/3	0.33									10:00:05.61	+02:25:17.4	3.28	23.95	20.04	1.19
450.179/850.88	1/4	0.02	10:00:22.77	+02:30:25.3	2.02	103 \pm 14					10:00:22.78	+02:30:25.2	2.06	22.06	20.69	0.66
	2/4	0.06									10:00:22.65	+02:30:22.5	1.33	25.78	24.99	0.55
	3/4	0.13									10:00:22.76	+02:30:22.2	1.93	25.06	24.54	0.65
	4/4	0.13									10:00:22.55	+02:30:24.0	1.96	25.68	23.31	2.48
450.189/850.114	1/2	0.003	10:00:14.10	+02:28:38.6	1.94	1345 \pm 17	10:00:14.07	+02:28:38.8	2.30	146 \pm 11	10:00:14.08	+02:28:38.7	2.16	—	18.34	—
	2/2	0.14									10:00:14.25	+02:28:35.6	1.99	26.30	22.83	—
450.193/850.49	1/6	0.05									10:00:05.13	+02:17:19.4	1.14	24.62	21.16	3.08
	2/6	0.08	10:00:05.09	+02:17:14.6	4.08	159 \pm 28					10:00:05.06	+02:17:14.1	4.63	22.61	20.15	1.15
	3/6	0.14									10:00:04.94	+02:17:19.3	3.03	26.59	22.68	3.06
	4/6	0.29									10:00:04.91	+02:17:16.7	3.06	24.95	22.08	2.00
	5/6	0.30									10:00:04.96	+02:17:21.4	3.13	26.57	23.26	3.15
	6/6	0.33									10:00:05.26	+02:17:17.2	3.31	23.99	22.50	3.09
450.206/850.53	1/4	0.08									10:00:11.10	+02:15:06.4	1.47	25.86	24.67	1.70
	2/4	0.22									10:00:11.24	+02:15:05.6	2.58	25.27	23.60	1.65
	3/4	0.31									10:00:11.07	+02:15:04.7	3.15	25.49	23.45	1.88
	4/4	0.41									10:00:10.89	+02:15:07.1	3.80	26.08	22.93	1.44
450.215/850.27	1/2	0.01	10:00:23.69	+02:19:15.0	1.69	119 \pm 17					10:00:23.67	+02:19:15.1	1.67	25.19	21.73	2.76
	3/3	0.38									10:00:23.66	+02:19:13.1	3.62	26.62	22.74	2.87
450.240/850.67	1/2	0.37									10:00:32.03	+02:33:28.1	3.53	28.88	23.08	2.73
	2/2	0.40									10:00:32.23	+02:33:27.8	3.72	25.63	22.48	2.64
450.247/850.151	1/2	0.15									10:00:41.42	+02:25:33.7	2.10	26.92	25.04	1.78
	2/2	0.18									10:00:41.35	+02:25:34.4	0.95	26.95	—	1.74
450.252/850.40	1/5	0.003	10:00:13.58	+02:22:25.6	2.78	605 \pm 14	10:00:13.55	+02:22:25.7	2.43	88 \pm 15	10:00:13.57	+02:22:25.4	2.52	23.10	19.95	—
	2/5	0.30									10:00:13.21	+02:22:23.6	3.11	25.70	23.68	—
	3/5	0.34									10:00:13.41	+02:22:21.4	3.33	23.81	23.66	—
	4/5	0.37									10:00:13.21	+02:22:26.7	3.55	24.31	23.57	—
	5/5	0.44									10:00:13.31	+02:22:21.1	3.94	26.19	24.18	—

Table Notes. All quantities are measured and given as in Table 6.

Table 8. Counterpart identifications and Multiwavelength Properties for SCUBA-2 850 μ m-detected Sources

NAME	COUNTER- PART #	p - val	RA ₂₄	DEC ₂₄	δ_{24} [$''$]	S_{24} [μ Jy]	RA _{1.4}	DEC _{1.4}	$\delta_{1.4}$ [$''$]	$S_{1.4}$ [μ Jy]	RA _{opt}	DEC _{opt}	δ_{opt} [$''$]	i [AB-mag]	3.6 μ m [AB-mag]	z_{phot}
850.01	1/1	0.0008					09:59:57.30	+02:27:30.5	1.20	68 \pm 13	09:59:57.29	+02:27:30.1	1.23	25.67	23.22	1.45
850.04	1/1	0.01	10:00:15.47	+02:15:50.5	1.78	123 \pm 18					10:00:15.49	+02:15:50.2	1.43	23.83	20.72	1.39
850.05	1/2	0.02									10:00:57.02	+02:20:14.0	0.31	24.59	—	2.76
	2/2	0.19									10:00:57.01	+02:20:12.0	2.32	27.03	22.18	2.48
850.11	1/2	0.10									10:00:49.90	+02:22:58.8	1.71	25.83	22.08	2.77
	2/2	0.11									10:00:49.94	+02:22:55.4	1.82	27.02	24.07	2.68
850.13	1/3	0.002									10:00:24.12	+02:20:05.0	0.28	—	24.09	0.86
	2/3	0.21									10:00:24.27	+02:20:03.8	2.55	26.14	24.71	1.03
	3/3	0.22									10:00:24.08	+02:20:02.8	2.58	24.63	23.81	0.94
850.15	1/1	0.08									10:00:25.25	+02:26:05.9	1.50	21.70	20.25	—
850.16	1/1	0.002	10:01:03.92	+02:24:48.2	1.08	229 \pm 18	10:01:03.91	+02:24:48.9	1.69	57 \pm 10	10:01:03.92	+02:24:48.0	0.89	24.95	20.82	—
	2/2	0.18									10:01:03.83	+02:24:45.1	2.32	23.15	20.70	—
850.17	1/1	0.29									10:00:00.36	+02:22:56.3	1.26	26.09	—	—
850.18	1/2	0.01									10:00:24.02	+02:29:47.3	0.62	25.67	23.71	3.01
	2/2	0.27									10:00:24.04	+02:29:50.1	2.90	26.81	23.61	2.83
850.19	1/2	0.11									10:00:15.67	+02:24:45.5	1.76	26.87	24.99	2.24
	2/2	0.21									10:00:15.92	+02:24:46.8	2.51	27.43	23.17	3.61
850.20	1/1	0.18									10:00:27.13	+02:31:38.5	2.32	24.77	22.22	2.80
850.22	1/2	0.05	10:00:18.69	+02:16:51.9	3.38	300 \pm 17					10:00:18.70	+02:16:52.5	2.72	25.50	20.40	2.06
	2/2	0.26									10:00:18.77	+02:16:58.0	2.83	27.05	24.11	2.29
850.24	1/1	0.0002	10:00:04.82	+02:30:45.3	0.51	321 \pm 14	10:00:04.81	+02:30:45.2	0.55	96 \pm 15	10:00:04.78	+02:30:45.2	1.00	27.21	20.82	3.51
850.25	1/5	0.0002	10:00:12.59	+02:14:44.1	0.20	331 \pm 15					10:00:12.58	+02:14:44.0	0.20	24.09	20.31	2.33
	2/5	0.08									10:00:12.57	+02:14:42.7	1.52	23.67	20.79	2.78
	3/5	0.18									10:00:12.71	+02:14:45.6	2.30	26.28	22.99	2.61
	4/5	0.20									10:00:12.75	+02:14:43.9	2.44	26.27	23.01	2.32
	5/5	0.20									10:00:12.44	+02:14:43.1	2.45	25.83	22.14	2.75
850.29	1/2	0.03	10:00:50.18	+02:26:17.8	2.57	155 \pm 18					10:00:50.15	+02:26:18.3	3.10	—	21.12	—
	2/2	0.02									10:00:50.15	+02:26:14.4	0.77	25.86	23.42	—
850.30	1/1	0.02	10:00:06.82	+02:22:07.4	1.89	186 \pm 14					10:00:06.80	+02:22:07.5	1.71	20.94	20.61	0.23
	2/2	0.10									10:00:06.86	+02:22:11.6	2.64	25.36	23.80	—
850.31	1/1	0.02	10:00:26.17	+02:17:39.0	2.27	296 \pm 44					10:00:26.18	+02:17:39.5	1.89	24.43	20.46	1.80
850.32	1/2	0.004	10:00:01.67	+02:24:27.9	2.73	287 \pm 12	10:00:01.67	+02:24:28.3	2.52	90 \pm 14	10:00:01.62	+02:24:28.0	2.02	27.53	21.71	1.95
	2/2	0.34									10:00:01.44	+02:24:28.4	1.40	25.07	—	1.58
850.35	1/2	0.06									10:01:05.07	+02:21:51.5	1.35	25.59	23.02	2.36
	2/2	0.23									10:01:05.15	+02:21:52.7	2.65	25.08	22.90	2.63
850.36	1/3	0.04	10:00:01.23	+02:17:42.4	3.08	127 \pm 49					10:00:01.38	+02:17:42.4	2.96	24.20	20.42	2.05
	2/3	0.13									10:00:01.21	+02:17:43.9	1.94	20.88	21.44	0.22
	3/3	0.13									10:00:01.44	+02:17:45.2	1.97	24.09	21.70	2.04
850.37	1/3	0.12									10:00:35.70	+02:28:27.4	1.84	28.03	23.31	4.57
	2/3	0.15									10:00:35.68	+02:28:28.0	2.08	27.96	23.31	3.99
	3/3	0.27									10:00:35.54	+02:28:29.0	2.92	28.41	23.98	3.53
850.38	1/4	0.07									10:00:23.45	+02:15:35.5	1.39	24.90	22.75	2.04
	2/4	0.08									10:00:23.58	+02:15:37.5	1.50	26.39	23.01	2.72
	3/4	0.14									10:00:23.63	+02:15:35.0	1.99	27.04	24.92	2.58
	4/4	0.22									10:00:23.36	+02:15:36.4	2.60	26.60	23.31	2.43
850.39	1/2	0.01									10:00:12.21	+02:23:09.8	0.62	26.48	24.32	—
	2/2	0.18									10:00:12.16	+02:23:07.9	2.31	24.76	23.20	—
850.43	1/1	0.12									10:00:26.31	+02:15:29.0	0.77	—	—	0.84
850.44	1/3	0.007	10:00:18.32	+02:22:50.0	1.24	128 \pm 16					10:00:18.29	+02:22:51.0	1.81	25.03	22.78	2.48
	2/3	0.11									10:00:18.16	+02:22:50.3	1.79	23.27	21.41	2.56
	3/3	0.14									10:00:18.33	+02:22:47.5	2.06	27.58	23.56	2.03
850.45	1/1	0.06	10:00:06.75	+02:20:44.7	3.52	105 \pm 33					10:00:06.78	+02:20:44.8	3.07	24.22	21.03	1.32
850.46	1/1	0.0006	10:00:25.54	+02:15:05.9	1.12	560 \pm 17	10:00:25.52	+02:15:05.8	1.01	112 \pm 10	10:00:25.51	+02:15:06.1	0.65	26.03	20.78	3.04
850.50	1/3	0.009					10:00:08.97	+02:20:26.5	3.92	62 \pm 12	10:00:09.11	+02:20:26.4	3.20	26.07	23.73	2.38
	2/3	0.02									10:00:09.17	+02:20:23.2	0.78	25.06	22.90	1.97
	3/3	0.24									10:00:08.96	+02:20:24.7	2.71	26.43	23.47	2.87
850.51	1/4	0.007	09:59:56.41	+02:18:53.0	1.23	193 \pm 15					09:59:56.39	+02:18:52.7	1.66	24.39	20.82	1.11
	2/4	0.23									09:59:56.32	+02:18:56.2	2.64	25.18	22.04	1.09
	3/4	0.26									09:59:56.56	+02:18:56.5	2.89	21.06	19.07	0.66
	4/4	0.29									09:59:56.63	+02:18:53.3	3.04	25.46	22.37	1.02
850.54	1/1	0.02									09:59:48.89	+02:27:48.9	0.71	26.82	23.91	3.07
850.56	NA															
850.57	1/4	0.0003	10:00:06.90	+02:33:08.1	1.20	592 \pm 184	10:00:06.82	+02:33:07.9	0.75	82 \pm 14	—	—	—	—	—	—
	2/4	0.13									10:00:06.81	+02:33:05.4	1.94	23.93	22.89	0.50
	3/4	0.20									10:00:06.68	+02:33:07.2	2.49	20.13	18.28	0.74
	4/4	0.21									10:00:07.01	+02:33:07.2	2.51	24.78	21.95	1.51
850.59	1/4	0.007	10:00:00.80	+02:20:02.4	1.21	85 \pm 13					10:00:00.84	+02:20:02.4	1.60	26.08	24.06	3.15
	2/4	0.15									10:00:00.92	+02:20:01.2	2.13	26.18	24.01	2.64
	3/4	0.16									10:00:00.77	+02:20:03.4	2.15	24.22	21.79	2.97
	4/4	0.23									10:00:00.60	+02:20:00.8	2.69	24.59	22.85	0.97
850.60	1/2	0.03	10:00:00.86	+02:27:41.2	2.54	239 \pm 14					10:00:00.82	+02:27:41.3	2.03	24.38	19.74	1.44
	2/2	0.10									10:00:00.81	+02:27:39.6	1.69	26.20	22.12	2.75
850.61	1/1	0.06									10:00:01.96	+02:28:20.8	1.34	23.88	22.16	0.53
850.63	1/3	0.08									09:59:53.47	+02:18:50.6	1.55	25.87	23.90	1.89

NAME	COUNTER- PART #	<i>p</i> - <i>val</i>	RA ₂₄	DEC ₂₄	δ_{24} [$''$]	S_{24} [μ Jy]	RA _{1.4}	DEC _{1.4}	$\delta_{1.4}$ [$''$]	$S_{1.4}$ [μ Jy]	RA _{opt}	DEC _{opt}	δ_{opt} [$''$]	<i>i</i> [AB-mag]	3.6 μ m [AB-mag]	<i>z</i> _{phot}
850.71	1/2	0.24									09:59:44.05	+02:21:06.3	1.12	27.01	—	2.17
	2/2	0.08									09:59:43.99	+02:21:03.8	1.51	24.55	24.13	0.90
850.72	1/4	0.04	10:00:13.69	+02:17:34.2	3.06	150 \pm 13					10:00:13.70	+02:17:34.8	3.62	—	—	—
	2/4	0.21									10:00:13.73	+02:17:28.9	2.55	—	24.84	0.93
	3/4	0.23									10:00:13.81	+02:17:32.6	2.67	25.64	23.40	2.08
	4/4	0.26									10:00:13.47	+02:17:32.2	2.88	25.48	24.22	1.82
850.73	1/5	0.04	10:00:20.52	+02:22:49.2	2.93	112 \pm 26					10:00:20.48	+02:22:48.6	3.80	26.48	22.48	3.91
	2/5	0.005									10:00:20.63	+02:22:51.2	0.38	25.75	22.90	1.82
	3/5	0.02									10:00:20.70	+02:22:51.3	0.67	25.07	23.14	1.65
	4/5	0.14									10:00:20.69	+02:22:53.2	1.99	25.59	22.43	2.50
	5/5	0.15									10:00:20.69	+02:22:49.1	2.16	25.13	23.59	1.67
850.74	1/1	0.25									10:00:05.41	+02:14:47.1	2.78	27.42	23.87	2.76
850.75	1/4	0.007					10:00:26.97	+02:22:30.5	3.64	82 \pm 16	10:00:26.96	+02:22:30.8	3.40	25.86	21.91	—
	2/4	0.05									10:00:26.79	+02:22:31.1	1.20	26.69	23.28	—
	3/4	0.25									10:00:26.91	+02:22:29.3	2.81	25.99	23.05	—
	4/4	0.34									10:00:26.52	+02:22:29.4	3.34	25.59	23.43	—
850.76	1/2	0.08									10:00:48.95	+02:30:24.88	1.62	24.31	22.94	1.06
	2/2	0.31									10:00:48.82	+02:30:21.00	3.08	23.22	22.61	0.86
850.77	1/1	0.12	10:00:05.47	+02:29:53.1	5.17	441 \pm 178					—	—	—	—	—	—
850.78	1/6	0.08	10:00:08.77	+02:19:16.2	4.11	207 \pm 14					10:00:08.93	+02:19:16.2	5.07	22.89	21.18	0.94
	2/6	0.11									10:00:08.78	+02:19:13.8	1.82	25.98	24.27	2.39
	3/6	0.22									10:00:08.88	+02:19:11.4	2.58	29.41	—	3.24
	4/6	0.29									10:00:08.66	+02:19:13.2	1.26	—	—	0.71
	5/6	0.31									10:00:08.73	+02:19:15.4	3.19	26.46	22.75	4.35
	6/6	0.32									10:00:08.67	+02:19:09.0	3.26	27.65	23.83	2.94
850.79	1/3	0.001									10:01:02.28	+02:22:34.1	0.20	21.39	20.55	—
	2/3	0.18									10:01:02.14	+02:22:34.1	2.29	23.34	22.20	—
	3/3	0.26									10:01:02.27	+02:22:37.0	2.83	23.99	23.40	—
850.80	1/3	0.16									10:00:14.13	+02:27:02.1	2.15	25.23	22.72	3.54
	2/3	0.17									10:00:14.26	+02:27:03.3	2.28	24.07	23.74	2.40
	3/3	0.31									10:00:13.99	+02:27:01.7	3.19	26.74	23.94	3.87
850.81	1/2	0.06									09:59:59.12	+02:24:41.9	1.35	24.11	23.58	0.40
	2/2	0.47									09:59:58.97	+02:24:39.8	1.73	26.81	—	2.81
850.82	1/1	0.03	10:00:54.96	+02:19:47.4	2.46	203 \pm 17					10:00:54.95	+02:19:47.1	2.09	26.03	21.11	2.87
850.84	1/1	0.22									10:00:41.67	+02:21:12.7	2.58	26.85	24.03	2.42
850.86	1/2	0.005	10:01:01.30	+02:24:39.4	1.04	299 \pm 19					10:01:01.27	+02:24:39.9	1.51	23.28	20.03	—
	2/2	0.10									10:01:01.31	+02:24:37.6	1.73	21.73	19.55	—
850.87	1/2	0.05	10:00:40.23	+02:17:55.5	3.18	284 \pm 15					10:00:40.26	+02:17:55.7	2.85	26.99	20.78	2.24
	2/2	0.11									10:00:40.33	+02:18:00.0	1.75	26.48	22.91	1.45
850.89	1/4	0.02	10:00:20.26	+02:17:25.1	2.12	401 \pm 16					10:00:20.25	+02:17:25.7	1.53	22.53	19.94	—
	2/4	0.04									10:00:20.19	+02:17:27.0	1.00	25.42	22.16	1.87
	3/4	0.11									10:00:20.24	+02:17:29.0	1.79	25.72	23.02	1.72
	4/4	0.20									10:00:20.37	+02:17:28.9	2.43	24.88	23.21	0.92
850.91	1/3	0.18									10:00:27.85	+02:25:51.9	2.30	26.95	23.91	2.71
	2/3	0.26									10:00:27.94	+02:25:51.6	2.84	26.73	24.91	2.21
	3/3	0.46									10:00:27.76	+02:25:55.1	1.69	25.95	—	2.68
850.93	1/3	0.01					10:00:57.06	+02:29:42.9	4.97	123 \pm 10	10:00:57.06	+02:29:42.8	5.08	24.47	20.88	—
	2/3	0.09									10:00:56.66	+02:29:44.7	1.59	25.82	24.76	—
	3/3	0.32									10:00:56.69	+02:29:48.3	3.23	21.25	20.79	0.37
850.94	1/2	0.002	10:00:02.62	+02:16:34.0	1.84	393 \pm 16	10:00:02.61	+02:16:33.8	1.65	72 \pm 11	10:00:02.61	+02:16:34.2	2.03	24.62	20.29	2.04
	2/2	0.006									10:00:02.62	+02:16:32.1	0.39	25.70	22.38	4.16
850.95	1/3	0.02	09:59:59.82	+02:27:06.6	1.88	387 \pm 67					09:59:59.80	+02:27:07.4	2.74	22.78	19.60	1.55
	2/3	0.13									09:59:59.82	+02:27:03.7	1.94	—	19.82	0.74
	3/3	0.32									09:59:59.93	+02:27:02.0	3.21	—	21.05	—
850.97	1/3	0.005					10:00:13.57	+02:18:05.0	2.87	148 \pm 15	10:00:13.59	+02:18:05.1	3.00	20.46	18.63	0.73
	2/3	0.03	10:00:13.60	+02:18:08.6	2.62	349 \pm 15					10:00:13.59	+02:18:08.5	2.40	24.02	21.12	1.48
	3/3	0.25									10:00:13.29	+02:18:08.7	2.82	25.22	22.91	1.80
850.98	1/1	0.19									10:00:14.49	+02:30:10.1	2.37	—	19.02	—

TABLE 8 CONTINUED.

Table 9. Physical Characteristics of SCUBA-2 Selected Galaxies

SHORT 450 μ m NAME	SHORT 850 μ m NAME	z_{phot}	χ^2_{fit}	Estimates from Infrared SED Fitting (§4.2)				LE PHARE Properties	
				L_{IR} (L_{\odot})	$\log SFR_{\text{IR}}$ ($M_{\odot} \text{ yr}^{-1}$)	$\log \lambda_{\text{peak}}$ (μm)	M_{dust} (M_{\odot})	$\log SFR_{\text{UV}}$ ($M_{\odot} \text{ yr}^{-1}$)	M_{\star} (M_{\odot})
450.00	850.07	$2.86^{+0.21}_{-0.26}$	0.4	$(5.1^{+7.4}_{-3.2}) \times 10^{13}$	3.9 ± 0.2	1.6 ± 0.4	$(5^{+6}_{-4}) \times 10^8$	$1.71^{+0.13}_{-0.33}$	$(2^{+3}_{-1}) \times 10^{10}$
450.01	850.02	$2.88^{+0.09}_{-0.18}$	0.4	$(1.1^{+1.7}_{-0.7}) \times 10^{13}$	3.3 ± 0.2	1.9 ± 0.4	$(1^{+2}_{-1}) \times 10^9$	$1.86^{+0.39}_{-0.15}$	$(2^{+2}_{-1}) \times 10^{11}$
450.02		$2.16^{+0.04}_{-0.06}$	2.4	$(8.6^{+16.6}_{-4.5}) \times 10^{12}$	3.2 ± 0.3	2.0 ± 0.5	$(1^{+3}_{-1}) \times 10^9$	$1.10^{+0.07}_{-0.07}$	$(9^{+10}_{-8}) \times 10^{10}$
450.03	850.00	$0.34^{+0.01}_{-0.01}$	4.7	$(4.3^{+5.1}_{-3.6}) \times 10^{10}$	0.9 ± 0.1	$\equiv 2.0$	–	$-0.50^{+0.07}_{-0.07}$	$(6^{+8}_{-5}) \times 10^{10}$
450.04	850.03	$3.82^{+0.44}_{-0.69}$	1.2	$(1.9^{+3.3}_{-1.1}) \times 10^{13}$	3.5 ± 0.3	1.8 ± 0.5	$(1^{+2}_{-1}) \times 10^9$	$2.45^{+0.11}_{-0.32}$	$(7^{+10}_{-5}) \times 10^{10}$
450.05	850.08	$3.99^{+0.08}_{-0.85}$	2.4	$(1.9^{+3.4}_{-1.1}) \times 10^{13}$	3.5 ± 0.2	1.8 ± 0.6	$(7^{+9}_{-6}) \times 10^8$	$2.16^{+0.10}_{-0.09}$	$(7^{+8}_{-6}) \times 10^{11}$
450.06	850.12	$2.08^{+0.08}_{-0.07}$	0.3	$(7.2^{+9.2}_{-5.7}) \times 10^{12}$	3.1 ± 0.1	1.9 ± 0.1	$(6^{+7}_{-5}) \times 10^8$	$2.00^{+0.07}_{-0.07}$	$(1^{+1}_{-1}) \times 10^{11}$
450.07		$4.70^{+0.07}_{-0.08}$	4.3	$(7.2^{+8.7}_{-6.0}) \times 10^{13}$	4.1 ± 0.1	$\equiv 2.0$	–	$2.53^{+0.14}_{-0.47}$	$(4^{+6}_{-3}) \times 10^{11}$
450.08		$5.15^{+0.20}_{-0.33}$	3.7	$(8.7^{+10.4}_{-7.2}) \times 10^{13}$	4.2 ± 0.1	$\equiv 2.0$	–	$2.51^{+0.25}_{-0.59}$	$(2^{+3}_{-2}) \times 10^{11}$
450.09	850.34	$1.90^{+0.03}_{-0.04}$	0.1	$(7.7^{+10.3}_{-5.7}) \times 10^{12}$	3.1 ± 0.1	1.8 ± 0.1	$(3^{+4}_{-2}) \times 10^8$	$2.26^{+0.09}_{-0.08}$	$(8^{+7}_{-7}) \times 10^9$
450.12		$0.93^{+0.01}_{-0.01}$	0.1	$(5.8^{+18.6}_{-1.8}) \times 10^{11}$	2.0 ± 0.5	$\equiv 2.0$	–	$1.61^{+0.07}_{-0.07}$	$(3^{+3}_{-3}) \times 10^{10}$
450.13		$2.87^{+0.13}_{-0.26}$	0.1	$(8.7^{+11.5}_{-6.6}) \times 10^{12}$	3.2 ± 0.1	1.8 ± 0.1	$(4^{+5}_{-3}) \times 10^8$	$2.01^{+0.08}_{-0.09}$	$(2^{+2}_{-2}) \times 10^{11}$
450.14		$1.47^{+0.01}_{-0.02}$	3.2	$(1.6^{+2.8}_{-0.9}) \times 10^{12}$	2.4 ± 0.2	2.0 ± 0.2	$(6^{+10}_{-4}) \times 10^8$	$1.81^{+0.09}_{-0.10}$	$(2^{+2}_{-2}) \times 10^{11}$
450.15	850.28	$2.79^{+0.28}_{-0.29}$	0.5	$(1.1^{+1.4}_{-0.8}) \times 10^{13}$	3.3 ± 0.1	1.8 ± 0.1	$(4^{+4}_{-3}) \times 10^8$	$1.62^{+0.33}_{-0.19}$	$(4^{+5}_{-3}) \times 10^{10}$
450.16		$2.32^{+0.02}_{-0.03}$	2.1	$(2.0^{+2.8}_{-1.4}) \times 10^{12}$	2.5 ± 0.2	2.2 ± 0.2	$(9^{+40}_{-10}) \times 10^9$	$1.20^{+0.07}_{-0.07}$	$(1^{+1}_{-1}) \times 10^{11}$
450.17	850.42	$1.23^{+0.21}_{-0.11}$	0.1	$(7.9^{+18.9}_{-3.3}) \times 10^{11}$	2.1 ± 0.4	2.1 ± 0.5	$(6^{+20}_{-2}) \times 10^8$	$-0.35^{+0.40}_{-0.31}$	$(6^{+9}_{-3}) \times 10^8$
450.19		$1.11^{+0.06}_{-0.02}$	9.7	$(9.7^{+32.0}_{-3.0}) \times 10^{11}$	2.2 ± 0.5	$\equiv 2.0$	–	$0.56^{+0.09}_{-0.09}$	$(8^{+10}_{-7}) \times 10^9$
450.20		$0.76^{+0.04}_{-0.03}$	0.8	$(2.6^{+5.7}_{-1.2}) \times 10^{11}$	1.6 ± 0.3	2.2 ± 0.5	$(7^{+40}_{-2}) \times 10^8$	$-0.05^{+0.37}_{-0.28}$	$(8^{+10}_{-6}) \times 10^8$
450.21		$0.84^{+0.01}_{-0.01}$	0.1	$(4.7^{+7.9}_{-2.8}) \times 10^{11}$	1.9 ± 0.2	2.1 ± 0.2	$(2^{+4}_{-1}) \times 10^8$	$1.98^{+0.08}_{-0.07}$	$(4^{+3}_{-3}) \times 10^{10}$
450.22	850.149	$2.11^{+0.20}_{-0.28}$	5.5	$(3.2^{+10.6}_{-1.1}) \times 10^{12}$	2.7 ± 0.5	$\equiv 2.0$	–	$0.31^{+0.13}_{-0.36}$	$(4^{+5}_{-3}) \times 10^9$
450.23		$0.97^{+0.06}_{-0.04}$	0.6	$(5.4^{+17.9}_{-6.3}) \times 10^{11}$	2.0 ± 0.5	$\equiv 2.0$	–	$0.46^{+0.34}_{-0.16}$	$(8^{+10}_{-6}) \times 10^8$
450.24		$0.16^{+0.01}_{-0.01}$	3.5	$(3.2^{+10.6}_{-1.1}) \times 10^{10}$	0.7 ± 0.5	$\equiv 2.0$	–	$0.55^{+0.09}_{-0.11}$	$(6^{+7}_{-5}) \times 10^{10}$
450.25		$0.61^{+0.01}_{-0.01}$	2.0	$(1.7^{+3.1}_{-1.1}) \times 10^{11}$	1.5 ± 0.3	2.2 ± 0.2	$(2^{+10}_{-1}) \times 10^8$	$0.80^{+0.07}_{-0.07}$	$(1^{+2}_{-1}) \times 10^{11}$
450.26		$2.68^{+0.11}_{-0.13}$	4.6	$(5.3^{+17.7}_{-1.6}) \times 10^{12}$	3.0 ± 0.5	$\equiv 2.0$	–	$1.89^{+0.03}_{-0.12}$	$(7^{+9}_{-3}) \times 10^9$
450.28		$1.98^{+0.03}_{-0.07}$	0.7	$(1.2^{+1.7}_{-0.8}) \times 10^{12}$	2.3 ± 0.2	2.3 ± 0.2	$(1^{+10}_{-1}) \times 10^{10}$	$2.10^{+0.07}_{-0.07}$	$(1^{+1}_{-1}) \times 10^{10}$
450.30		$2.81^{+0.56}_{-0.56}$	3.5	$(6.0^{+10.1}_{-3.6}) \times 10^{12}$	3.0 ± 0.2	1.9 ± 0.2	$(4^{+5}_{-3}) \times 10^8$	$1.81^{+0.12}_{-0.18}$	$(1^{+1}_{-1}) \times 10^{11}$
450.32	850.26	$1.72^{+0.15}_{-0.09}$	5.0	$(1.6^{+2.3}_{-1.1}) \times 10^{12}$	2.4 ± 0.2	2.1 ± 0.2	$(7^{+10}_{-5}) \times 10^8$	$-0.27^{+0.22}_{-0.52}$	$(4^{+20}_{-1}) \times 10^8$
450.33		$0.84^{+0.01}_{-0.01}$	0.1	$(3.8^{+7.2}_{-2.1}) \times 10^{11}$	1.8 ± 0.3	2.1 ± 0.2	$(3^{+6}_{-1}) \times 10^8$	$1.30^{+0.08}_{-0.09}$	$(4^{+4}_{-4}) \times 10^{10}$
450.34		$1.83^{+0.03}_{-0.03}$	3.9	$(2.4^{+6.5}_{-0.9}) \times 10^{12}$	2.6 ± 0.4	2.0 ± 0.7	$(6^{+10}_{-3}) \times 10^8$	$1.89^{+0.08}_{-0.07}$	$(8^{+9}_{-7}) \times 10^{10}$
450.36	850.58	$3.04^{+0.16}_{-0.12}$	0.1	$(6.9^{+18.8}_{-2.6}) \times 10^{12}$	3.1 ± 0.4	1.9 ± 0.7	$(7^{+10}_{-5}) \times 10^8$	$2.39^{+0.13}_{-0.41}$	$(3^{+3}_{-6}) \times 10^{10}$
450.37		$2.17^{+0.08}_{-0.08}$	1.9	$(3.1^{+10.6}_{-0.9}) \times 10^{12}$	2.7 ± 0.5	$\equiv 2.0$	–	$1.26^{+0.37}_{-0.15}$	$(4^{+6}_{-2}) \times 10^9$
450.39		$0.61^{+0.02}_{-0.02}$	0.1	$(1.6^{+5.4}_{-0.5}) \times 10^{11}$	1.4 ± 0.5	$\equiv 2.0$	–	$-2.37^{+0.67}_{-3.00}$	$(3^{+4}_{-3}) \times 10^9$
450.41		$3.46^{+1.74}_{-1.90}$	0.1	$(8.8^{+30.3}_{-2.5}) \times 10^{12}$	3.2 ± 0.5	$\equiv 2.0$	–	$1.14^{+0.39}_{-0.56}$	$(5^{+10}_{-2}) \times 10^9$
450.42	850.48	$4.81^{+0.14}_{-0.21}$	3.1	$(1.6^{+4.0}_{-0.6}) \times 10^{13}$	3.4 ± 0.4	1.7 ± 0.8	$(3^{+4}_{-2}) \times 10^8$	$2.60^{+0.12}_{-0.34}$	$(3^{+4}_{-3}) \times 10^{11}$
450.43		$0.36^{+0.06}_{-0.07}$	1.6	$(3.8^{+13.3}_{-1.1}) \times 10^{10}$	0.8 ± 0.5	$\equiv 2.0$	–	$-1.11^{+0.48}_{-0.55}$	$(2^{+3}_{-3}) \times 10^8$
450.44		$1.75^{+0.15}_{-0.51}$	0.1	$(1.8^{+6.3}_{-0.5}) \times 10^{12}$	2.5 ± 0.5	$\equiv 2.0$	–	$0.33^{+0.41}_{-0.39}$	$(8^{+20}_{-4}) \times 10^8$
450.45		$2.01^{+0.93}_{-0.71}$	1.0	$(2.5^{+8.9}_{-0.7}) \times 10^{12}$	2.6 ± 0.5	$\equiv 2.0$	–	$0.61^{+0.43}_{-0.37}$	$(3^{+4}_{-1}) \times 10^9$
450.46		$3.06^{+0.08}_{-0.06}$	4.3	$(5.5^{+19.6}_{-1.6}) \times 10^{12}$	3.0 ± 0.5	$\equiv 2.0$	–	$2.17^{+0.12}_{-0.36}$	$(3^{+5}_{-3}) \times 10^{10}$
450.47		$1.77^{+0.07}_{-0.24}$	0.1	$(1.1^{+4.0}_{-0.3}) \times 10^{12}$	2.3 ± 0.5	$\equiv 2.0$	–	$1.64^{+0.35}_{-0.10}$	$(6^{+8}_{-4}) \times 10^9$
450.49		$1.70^{+0.16}_{-0.10}$	4.1	$(1.4^{+5.1}_{-0.4}) \times 10^{12}$	2.4 ± 0.6	$\equiv 2.0$	–	$0.48^{+0.28}_{-0.34}$	$(2^{+3}_{-3}) \times 10^9$
450.51		$1.58^{+0.22}_{-0.45}$	0.1	$(1.1^{+2.8}_{-0.3}) \times 10^{12}$	2.3 ± 0.6	$\equiv 2.0$	–	$0.79^{+0.37}_{-0.28}$	$(1^{+2}_{-0.7}) \times 10^9$
450.53	850.109	$1.01^{+0.01}_{-0.01}$	1.8	$(8.6^{+14.6}_{-5.1}) \times 10^{11}$	2.2 ± 0.2	2.0 ± 0.2	$(2^{+3}_{-1}) \times 10^8$	$1.40^{+0.08}_{-0.08}$	$(8^{+9}_{-7}) \times 10^{10}$
450.54	850.96	$1.90^{+0.14}_{-0.12}$	1.1	$(1.5^{+4.7}_{-0.5}) \times 10^{12}$	2.4 ± 0.5	2.0 ± 0.8	$(4^{+7}_{-2}) \times 10^8$	$1.73^{+0.13}_{-0.36}$	$(3^{+5}_{-3}) \times 10^9$
450.55	850.06	$0.37^{+0.01}_{-0.01}$	1.6	$(2.8^{+3.4}_{-2.3}) \times 10^{10}$	0.7 ± 0.1	$\equiv 2.0$	–	$-2.12^{+0.11}_{-0.34}$	$(3^{+4}_{-3}) \times 10^{10}$
450.56		$2.82^{+1.39}_{-1.20}$	3.6	$(5.0^{+17.8}_{-1.4}) \times 10^{12}$	2.9 ± 0.6	$\equiv 2.0$	–	$0.94^{+0.74}_{-0.74}$	$(3^{+20}_{-1}) \times 10^9$
450.57		$3.48^{+1.33}_{-1.60}$	3.6	$(7.4^{+26.5}_{-2.1}) \times 10^{12}$	3.1 ± 0.6	$\equiv 2.0$	–	$-3.61^{+2.43}_{-0.32}$	$(1^{+1}_{-0.9}) \times 10^{11}$
450.59	850.101	$0.47^{+0.01}_{-0.01}$	4.0	$(8.3^{+18.6}_{-3.7}) \times 10^{10}$	1.2 ± 0.3	2.2 ± 0.4	$(2^{+50}_{-1}) \times 10^8$	$0.91^{+0.08}_{-0.08}$	$(3^{+3}_{-2}) \times 10^{10}$
450.61		$4.58^{+0.11}_{-0.06}$	1.4	$(1.3^{+2.6}_{-0.7}) \times 10^{13}$	3.3 ± 0.3	1.7 ± 0.3	$(2^{+3}_{-2}) \times 10^8$	$2.69^{+0.12}_{-0.36}$	$(1^{+20}_{-7}) \times 10^{10}$
450.62		$1.95^{+1.32}_{-1.10}$	0.1	$(1.9^{+6.7}_{-0.5}) \times 10^{12}$	2.5 ± 0.6	$\equiv 2.0$	–	$0.40^{+0.56}_{-0.74}$	$(1^{+7}_{-0.2}) \times 10^9$
450.63		$2.36^{+0.13}_{-0.12}$	3.4	$(2.8^{+10.2}_{-0.8}) \times 10^{12}$	2.7 ± 0.6	$\equiv 2.0$	–	$0.53^{+0.35}_{-0.11}$	$(3^{+5}_{-2}) \times 10^9$
450.65		$0.70^{+2.57}_{-0.49}$	0.1	$(1.5^{+5.5}_{-0.4}) \times 10^{11}$	1.4 ± 0.6	$\equiv 2.0$	–	$-0.30^{+0.50}_{-0.57}$	$(2^{+4}_{-1}) \times 10^8$
450.67		$0.93^{+0.01}_{-0.01}$	1.4	$(8.7^{+18.1}_{-4.2}) \times 10^{11}$	2.2 ± 0.3	2.0 ± 0.2	$(2^{+4}_{-1}) \times 10^8$	$2.23^{+0.09}_{-0.10}$	$(5^{+5}_{-4}) \times 10^{10}$
450.69		$2.04^{+0.49}_{-0.48}$	0.1	$(2.0^{+7.3}_{-0.5}) \times 10^{12}$	2.5 ± 0.6	$\equiv 2.0$	–	$0.71^{+0.41}_{-0.38}$	$(3^{+5}_{-2}) \times 10^9$

Some basic derived properties of 450 μ m sources using the infrared SED fitting described in § 4.2. The sources' optical/near-infrared photometric redshifts are given by z_p . Their integrated 8–1000 μ m infrared luminosity, L_{IR} , infrared star formation rates SFR_{IR} (calculated via the relation given in Kennicutt 1998a), SED peak wavelength, and approximated dust masses M_{dust} are calculated assuming SEDs as described in section 4.2. Sources with fewer than three IR photometric points have the SED peak wavelength (or dust temperature) fixed to the mean of the remainder of the sample, measured to be $\langle \log(\lambda_{\text{peak}}/\mu\text{m}) \rangle = 2.05 \pm 0.04$ for 450 μ m-detected galaxies and $\langle \log(\lambda_{\text{peak}}/\mu\text{m}) \rangle = 2.12 \pm 0.04$ for 850 μ m-only detected galaxies.

SHORT 450 μ m NAME	SHORT 850 μ m NAME	z_{phot}	χ^2_{fit}	Estimates from Infrared SED Fitting (§4.2)				LE PHARE Properties	
				LIR (L_{\odot})	logSFR _{IR} ($M_{\odot} \text{ yr}^{-1}$)	log λ_{peak} (μm)	M_{dust} (M_{\odot})	logSFR _{UV} ($M_{\odot} \text{ yr}^{-1}$)	M_{\star} (M_{\odot})
450.70		$3.03^{+0.04}_{-0.03}$	0.1	$(8.6^{+17.7}_{-4.1}) \times 10^{12}$	3.2 ± 0.3	1.8 ± 0.3	$(3^{+4}_{-2}) \times 10^8$	$3.06^{+0.09}_{-0.36}$	$(6^{+8}_{-5}) \times 10^{10}$
450.71		$1.95^{+0.61}_{-0.42}$	0.6	$(2.6^{+9.5}_{-0.7}) \times 10^{12}$	2.6 ± 0.6	$\equiv 2.0$	—	$0.67^{+0.41}_{-0.38}$	$(2^{+4}_{-1}) \times 10^9$
450.72		$1.43^{+0.31}_{-0.11}$	2.8	$(9.9^{+36.1}_{-2.7}) \times 10^{11}$	2.2 ± 0.6	$\equiv 2.0$	—	$0.91^{+0.24}_{-0.51}$	$(2^{+4}_{-1}) \times 10^9$
450.74		$0.75^{+0.01}_{-0.01}$	3.8	$(1.9^{+7.0}_{-0.5}) \times 10^{11}$	1.5 ± 0.6	$\equiv 2.0$	—	$1.04^{+0.09}_{-0.10}$	$(4^{+5}_{-3}) \times 10^9$
450.75		$2.26^{+2.30}_{-1.30}$	3.9	$(3.2^{+11.9}_{-0.9}) \times 10^{12}$	2.7 ± 0.6	$\equiv 2.0$	—	$0.56^{+0.44}_{-0.39}$	$(2^{+3}_{-1}) \times 10^9$
450.76		$1.96^{+0.45}_{-0.51}$	0.1	$(1.9^{+6.8}_{-0.5}) \times 10^{12}$	2.5 ± 0.6	$\equiv 2.0$	—	$-0.03^{+0.43}_{-0.38}$	$(1^{+2}_{-0.5}) \times 10^9$
450.77		$1.43^{+0.03}_{-0.04}$	0.1	$(8.8^{+32.3}_{-2.4}) \times 10^{11}$	2.2 ± 0.6	$\equiv 2.0$	—	$1.27^{+0.63}_{-0.48}$	$(3^{+4}_{-1}) \times 10^{10}$
450.81	850.10	$1.75^{+0.08}_{-0.12}$	0.1	$(1.6^{+2.3}_{-1.1}) \times 10^{12}$	2.4 ± 0.2	2.1 ± 0.2	$(1^{+2}_{-1}) \times 10^9$	$1.58^{+0.14}_{-0.15}$	$(2^{+2}_{-1}) \times 10^{10}$
450.86	850.55	$3.59^{+0.45}_{-0.81}$	1.8	$(6.8^{+25.4}_{-1.8}) \times 10^{12}$	3.1 ± 0.6	$\equiv 2.0$	—	$1.69^{+0.41}_{-0.29}$	$(1^{+2}_{-0.9}) \times 10^{10}$
450.87	850.09	$2.71^{+0.19}_{-0.17}$	3.2	$(6.3^{+9.0}_{-4.4}) \times 10^{12}$	3.0 ± 0.2	1.9 ± 0.2	$(1^{+10}_{-8}) \times 10^8$	$2.04^{+0.09}_{-0.10}$	$(1^{+2}_{-1}) \times 10^{11}$
450.94	850.23	$0.71^{+0.01}_{-0.01}$	3.4	$(8.2^{+30.9}_{-2.1}) \times 10^{10}$	1.1 ± 0.6	$\equiv 2.0$	—	$-4.41^{+3.35}_{-0.33}$	$(2^{+3}_{-2}) \times 10^{10}$
450.96	850.133	$2.34^{+0.40}_{-0.41}$	0.1	$(2.1^{+3.0}_{-0.6}) \times 10^{12}$	2.6 ± 0.6	$\equiv 2.0$	—	$1.09^{+0.42}_{-0.22}$	$(2^{+1}_{-1}) \times 10^{10}$
450.99	850.33	$2.16^{+0.08}_{-0.13}$	2.9	$(1.9^{+5.0}_{-0.7}) \times 10^{12}$	2.5 ± 0.4	2.1 ± 0.6	$(2^{+4}_{-1}) \times 10^9$	$1.74^{+0.11}_{-0.32}$	$(9^{+10}_{-7}) \times 10^{10}$
450.106	850.92	$1.0^{+0.01}_{-0.01}$	0.1	$(2.3^{+8.8}_{-0.9}) \times 10^{11}$	1.6 ± 0.6	$\equiv 2.0$	—	$0.96^{+0.27}_{-0.17}$	$(2^{+2}_{-1}) \times 10^{10}$
450.126	850.159	$2.04^{+0.92}_{-1.30}$	0.4	$(1.4^{+5.5}_{-0.4}) \times 10^{12}$	2.4 ± 0.6	$\equiv 2.0$	—	$1.27^{+0.27}_{-0.35}$	$(1^{+2}_{-0.5}) \times 10^{10}$
450.133	850.131	$0.93^{+0.01}_{-0.01}$	0.1	$(1.8^{+7.2}_{-0.4}) \times 10^{11}$	1.5 ± 0.6	$\equiv 2.0$	—	$2.80^{+0.07}_{-0.07}$	$(3^{+3}_{-2}) \times 10^{10}$
450.134	850.52	$2.89^{+0.14}_{-0.24}$	2.8	$(4.1^{+7.0}_{-2.2}) \times 10^{12}$	2.8 ± 0.2	1.9 ± 0.3	$(4^{+6}_{-4}) \times 10^8$	$1.73^{+0.14}_{-0.32}$	$(6^{+7}_{-7}) \times 10^{10}$
450.135	850.163	$1.68^{+0.08}_{-0.06}$	1.0	$(2.5^{+9.9}_{-0.6}) \times 10^{12}$	2.6 ± 0.6	$\equiv 2.0$	—	$1.88^{+0.08}_{-0.08}$	$(2^{+3}_{-2}) \times 10^{10}$
450.166	850.83	$0.93^{+0.01}_{-0.01}$	3.2	$(1.7^{+7.1}_{-0.4}) \times 10^{11}$	1.5 ± 0.6	$\equiv 2.0$	—	$0.54^{+0.12}_{-0.12}$	$(2^{+3}_{-2}) \times 10^9$
450.173	850.104	$1.01^{+0.01}_{-0.01}$	3.3	$(5.8^{+23.9}_{-1.4}) \times 10^{11}$	2.0 ± 0.6	$\equiv 2.0$	—	$1.83^{+0.36}_{-0.12}$	$(2^{+3}_{-2}) \times 10^{10}$
450.179	850.88	$0.66^{+0.01}_{-0.01}$	0.1	$(6.9^{+28.8}_{-1.7}) \times 10^{10}$	1.1 ± 0.6	$\equiv 2.0$	—	$1.62^{+0.11}_{-0.42}$	$(5^{+6}_{-4}) \times 10^9$
450.193	850.49	$3.08^{+0.13}_{-0.16}$	2.9	$(3.2^{+13.3}_{-0.8}) \times 10^{12}$	2.7 ± 0.6	$\equiv 2.0$	—	$2.28^{+0.10}_{-0.29}$	$(1^{+2}_{-1}) \times 10^{11}$
450.206	850.53	$1.70^{+0.20}_{-0.20}$	3.4	$(7.9^{+33.5}_{-1.9}) \times 10^{11}$	2.1 ± 0.6	$\equiv 2.0$	—	$-0.16^{+0.15}_{-0.06}$	$(1^{+2}_{-0.6}) \times 10^9$
450.215	850.27	$2.76^{+0.10}_{-0.12}$	3.0	$(4.1^{+6.5}_{-2.6}) \times 10^{12}$	2.8 ± 0.2	1.9 ± 0.3	$(6^{+8}_{-5}) \times 10^8$	$1.66^{+0.25}_{-0.10}$	$(8^{+9}_{-6}) \times 10^{10}$
450.240	850.67	$2.73^{+2.39}_{-1.20}$	3.0	$(2.4^{+10.3}_{-0.5}) \times 10^{12}$	2.6 ± 0.6	$\equiv 2.0$	—	$1.12^{+0.28}_{-2.30}$	$(2^{+3}_{-1}) \times 10^{10}$
450.247	850.151	$1.78^{+0.93}_{-0.71}$	0.1	$(7.1^{+31.1}_{-1.6}) \times 10^{11}$	2.1 ± 0.6	$\equiv 2.0$	—	$0.07^{+0.44}_{-0.42}$	$(5^{+10}_{-2}) \times 10^8$
850.01		$1.37^{+0.44}_{-0.25}$	1.9	$(4.7^{+8.6}_{-2.6}) \times 10^{11}$	1.9 ± 0.3	2.3 ± 0.3	$(6^{+20}_{-2}) \times 10^9$	$0.98^{+0.29}_{-0.25}$	$(2^{+2}_{-1}) \times 10^9$
850.04		$1.39^{+0.02}_{-0.02}$	1.3	$(4.7^{+7.9}_{-2.8}) \times 10^{11}$	1.9 ± 0.2	2.4 ± 0.2	$(1^{+2}_{-1}) \times 10^{10}$	$1.37^{+0.09}_{-0.07}$	$(3^{+4}_{-3}) \times 10^{10}$
850.05		$2.55^{+0.12}_{-0.15}$	0.1	$(2.8^{+5.1}_{-1.5}) \times 10^{12}$	2.7 ± 0.3	2.1 ± 0.3	$(5^{+10}_{-2}) \times 10^9$	$1.47^{+0.10}_{-0.08}$	$(2^{+2}_{-2}) \times 10^{10}$
850.11		$2.77^{+0.16}_{-0.19}$	0.3	$(1.5^{+4.4}_{-0.5}) \times 10^{12}$	2.4 ± 0.5	$\equiv 2.1$	—	$1.36^{+0.10}_{-0.34}$	$(4^{+5}_{-4}) \times 10^{10}$
850.13		$0.83^{+0.48}_{-0.55}$	0.2	$(9.0^{+17.5}_{-4.7}) \times 10^{10}$	1.2 ± 0.3	2.4 ± 0.3	$(2^{+10}_{-1}) \times 10^9$	$-0.13^{+0.51}_{-0.38}$	$(8^{+10}_{-9}) \times 10^8$
850.18		$3.01^{+0.17}_{-0.21}$	0.1	$(2.3^{+5.6}_{-1.0}) \times 10^{12}$	2.6 ± 0.4	2.0 ± 0.6	$(1^{+2}_{-1}) \times 10^9$	$1.08^{+0.35}_{-0.30}$	$(9^{+10}_{-6}) \times 10^9$
850.19		$2.24^{+2.19}_{-1.00}$	0.1	$(4.5^{+14.0}_{-1.5}) \times 10^{11}$	1.9 ± 0.5	$\equiv 2.1$	—	$0.48^{+0.43}_{-0.39}$	$(1^{+2}_{-0.7}) \times 10^9$
850.20		$2.80^{+0.05}_{-0.07}$	0.1	$(1.4^{+3.4}_{-0.9}) \times 10^{12}$	2.4 ± 0.4	2.1 ± 0.5	$(2^{+4}_{-1}) \times 10^9$	$1.08^{+0.08}_{-0.07}$	$(3^{+4}_{-3}) \times 10^{10}$
850.22		$2.06^{+0.10}_{-0.10}$	0.4	$(1.2^{+2.6}_{-0.6}) \times 10^{12}$	2.3 ± 0.3	2.3 ± 0.3	$(5^{+10}_{-1}) \times 10^9$	$1.83^{+0.11}_{-0.35}$	$(2^{+2}_{-2}) \times 10^{11}$
850.24		$2.94^{+0.96}_{-0.36}$	1.2	$(1.0^{+1.5}_{-0.7}) \times 10^{13}$	3.2 ± 0.2	1.8 ± 0.1	$(5^{+6}_{-4}) \times 10^8$	$0.21^{+0.14}_{-0.35}$	$(1^{+10}_{-0.2}) \times 10^9$
850.25		$2.33^{+0.05}_{-0.05}$	1.3	$(1.9^{+3.5}_{-1.1}) \times 10^{12}$	2.5 ± 0.2	2.3 ± 0.3	$(8^{+30}_{-2}) \times 10^9$	$2.50^{+0.13}_{-0.50}$	$(2^{+2}_{-2}) \times 10^{11}$
850.30		$0.23^{+0.01}_{-0.01}$	1.9	$(1.4^{+2.2}_{-1.1}) \times 10^{10}$	0.4 ± 0.2	2.3 ± 0.1	$(1^{+2}_{-1}) \times 10^8$	$0.15^{+0.10}_{-0.10}$	$(1^{+2}_{-1}) \times 10^9$
850.31		$1.80^{+0.04}_{-0.05}$	0.6	$(2.9^{+4.5}_{-1.9}) \times 10^{12}$	2.7 ± 0.2	2.0 ± 0.3	$(5^{+6}_{-4}) \times 10^8$	$2.05^{+0.10}_{-0.12}$	$(7^{+8}_{-5}) \times 10^{10}$
850.32		$2.87^{+0.13}_{-0.26}$	13.	$(8.5^{+11.9}_{-6.1}) \times 10^{12}$	3.2 ± 0.1	1.8 ± 0.1	$(4^{+4}_{-3}) \times 10^8$	$2.01^{+0.08}_{-0.09}$	$(2^{+2}_{-2}) \times 10^{11}$
850.35		$2.36^{+0.20}_{-0.33}$	0.1	$(1.1^{+3.4}_{-0.4}) \times 10^{12}$	2.3 ± 0.5	2.2 ± 0.6	$(3^{+10}_{-1}) \times 10^9$	$1.06^{+0.08}_{-0.09}$	$(1^{+2}_{-0.9}) \times 10^{10}$
850.36		$2.05^{+0.02}_{-0.03}$	2.9	$(2.2^{+7.0}_{-0.7}) \times 10^{12}$	2.6 ± 0.5	$\equiv 2.1$	—	$1.72^{+0.10}_{-0.30}$	$(1^{+2}_{-1}) \times 10^{11}$
850.37		$4.57^{+1.07}_{-1.60}$	0.3	$(3.3^{+10.6}_{-1.0}) \times 10^{12}$	2.8 ± 0.5	$\equiv 2.1$	—	$2.10^{+0.19}_{-0.33}$	$(7^{+10}_{-4}) \times 10^{10}$
850.38		$2.04^{+0.14}_{-0.09}$	0.1	$(1.5^{+4.0}_{-0.6}) \times 10^{12}$	2.4 ± 0.4	2.1 ± 0.6	$(1^{+2}_{-1}) \times 10^9$	$1.79^{+0.07}_{-0.07}$	$(3^{+3}_{-2}) \times 10^9$
850.43		$0.84^{+0.43}_{-0.42}$	1.3	$(5.1^{+16.4}_{-1.6}) \times 10^{10}$	0.9 ± 0.5	$\equiv 2.1$	—	$-0.07^{+0.52}_{-0.38}$	$(8^{+20}_{-4}) \times 10^8$
850.44		$2.48^{+0.13}_{-0.10}$	1.5	$(3.0^{+4.9}_{-1.9}) \times 10^{12}$	2.7 ± 0.2	1.9 ± 0.2	$(4^{+5}_{-3}) \times 10^8$	$1.61^{+0.11}_{-0.34}$	$(1^{+2}_{-0.7}) \times 10^{10}$
850.45		$1.32^{+0.03}_{-0.05}$	1.1	$(2.3^{+7.4}_{-0.7}) \times 10^{11}$	1.6 ± 0.5	$\equiv 2.1$	—	$1.56^{+0.11}_{-0.27}$	$(3^{+3}_{-2}) \times 10^{10}$
850.46		$2.84^{+0.13}_{-0.19}$	0.1	$(1.5^{+2.0}_{-1.0}) \times 10^{13}$	3.4 ± 0.1	1.8 ± 0.1	$(4^{+5}_{-7}) \times 10^8$	$1.90^{+0.16}_{-0.24}$	$(2^{+2}_{-2}) \times 10^{11}$
850.50		$2.38^{+0.37}_{-0.51}$	0.1	$(3.2^{+10.6}_{-1.1}) \times 10^{11}$	1.7 ± 0.5	2.4 ± 0.4	$(2^{+70}_{-1}) \times 10^{10}$	$0.90^{+0.40}_{-0.19}$	$(5^{+3}_{-2}) \times 10^9$
850.51		$1.11^{+0.07}_{-0.04}$	1.0	$(6.6^{+10.5}_{-4.1}) \times 10^{11}$	2.1 ± 0.2	2.1 ± 0.2	$(6^{+10}_{-3}) \times 10^8$	$1.29^{+0.08}_{-0.07}$	$(8^{+10}_{-7}) \times 10^9$
850.54		$3.07^{+1.19}_{-1.20}$	1.6	$(2.3^{+7.5}_{-0.7}) \times 10^{12}$	2.6 ± 0.5	$\equiv 2.1$	—	$1.25^{+0.40}_{-0.48}$	$(8^{+10}_{-4}) \times 10^9$
850.57		$0.74^{+0.01}_{-0.01}$	1.2	$(9.4^{+21.3}_{-4.1}) \times 10^{10}$	1.2 ± 0.4	2.4 ± 0.4	$(2^{+7}_{-1}) \times 10^9$	$-1.83^{+1.35}_{-0.14}$	$(2^{+2}_{-2}) \times 10^{11}$
850.59		$3.15^{+0.13}_{-0.17}$	0.3	$(3.8^{+12.9}_{-1.1}) \times 10^{12}$	2.8 ± 0.5	$\equiv 2.1$	—	$1.05^{+0.38}_{-0.13}$	$(8^{+10}_{-4}) \times 10^9$

TABLE 9 – CONTINUED.

SHORT 450 μ m NAME	SHORT 850 μ m NAME	z_{phot}	χ_{fit}^2	Estimates from Infrared SED Fitting (§4.2)				LE PHARE Properties	
				L_{IR} (L_{\odot})	$\log \text{SFR}_{\text{IR}}$ ($M_{\odot} \text{ yr}^{-1}$)	$\log \lambda_{\text{peak}}$ (μm)	M_{dust} (M_{\odot})	$\log \text{SFR}_{\text{UV}}$ ($M_{\odot} \text{ yr}^{-1}$)	M_{\star} (M_{\odot})
850.60		$1.44^{+0.02}_{-0.02}$	4.5	$(1.4^{+2.2}_{-0.9}) \times 10^{12}$	2.4 ± 0.2	2.0 ± 0.2	$(4^{+5}_{-3}) \times 10^8$	$1.43^{+0.08}_{-0.09}$	$(1^{+1}_{-1}) \times 10^{11}$
850.61		$0.53^{+0.02}_{-0.02}$	0.4	$(5.4^{+14.4}_{-2.0}) \times 10^{10}$	1.0 ± 0.4	2.3 ± 0.5	$(4^{+50}_{-1}) \times 10^8$	$-0.31^{+0.23}_{-0.15}$	$(6^{+8}_{-6}) \times 10^8$
850.63		$1.89^{+0.23}_{-0.18}$	1.2	$(3.4^{+4.1}_{-2.8}) \times 10^{11}$	1.8 ± 0.1	$\equiv 2.1$	—	$0.23^{+0.14}_{-0.33}$	$(3^{+4}_{-2}) \times 10^9$
850.64		$3.39^{+1.16}_{-1.50}$	0.1	$(2.1^{+7.1}_{-0.6}) \times 10^{12}$	2.6 ± 0.5	$\equiv 2.1$	—	$1.61^{+0.30}_{-0.40}$	$(1^{+2}_{-0.7}) \times 10^{10}$
850.65		$0.48^{+0.01}_{-0.01}$	5.3	$(7.6^{+13.1}_{-4.4}) \times 10^{10}$	1.1 ± 0.2	2.3 ± 0.2	$(3^{+30}_{-1}) \times 10^8$	$0.42^{+0.80}_{-0.09}$	$(4^{+4}_{-2}) \times 10^8$
850.66		$0.94^{+0.14}_{-0.16}$	1.2	$(1.6^{+5.6}_{-0.5}) \times 10^{11}$	1.4 ± 0.5	$\equiv 2.1$	—	$0.14^{+0.37}_{-0.37}$	$(5^{+8}_{-4}) \times 10^8$
850.68		$1.95^{+0.04}_{-0.04}$	0.1	$(2.7^{+4.4}_{-1.7}) \times 10^{12}$	2.7 ± 0.2	2.0 ± 0.2	$(4^{+5}_{-3}) \times 10^8$	$1.76^{+0.10}_{-0.30}$	$(2^{+2}_{-1}) \times 10^{11}$
850.69		$1.80^{+0.15}_{-0.11}$	0.1	$(1.6^{+2.9}_{-0.9}) \times 10^{12}$	2.4 ± 0.3	2.0 ± 0.2	$(4^{+6}_{-3}) \times 10^8$	$1.60^{+0.07}_{-0.07}$	$(4^{+5}_{-3}) \times 10^{10}$
850.70		$0.78^{+0.01}_{-0.03}$	2.3	$(1.8^{+3.2}_{-1.0}) \times 10^{11}$	1.5 ± 0.3	2.2 ± 0.2	$(4^{+10}_{-1}) \times 10^8$	$1.40^{+0.07}_{-0.07}$	$(2^{+3}_{-2}) \times 10^9$
850.71		$2.17^{+1.36}_{-1.40}$	0.3	$(8.7^{+30.0}_{-2.5}) \times 10^{11}$	2.2 ± 0.5	$\equiv 2.1$	—	$0.61^{+0.60}_{-0.78}$	$(2^{+10}_{-1}) \times 10^9$
850.72		$2.80^{+0.15}_{-0.16}$	2.0	$(4.5^{+7.9}_{-2.6}) \times 10^{12}$	2.9 ± 0.2	1.9 ± 0.2	$(3^{+4}_{-2}) \times 10^8$	$1.78^{+0.10}_{-0.09}$	$(2^{+2}_{-2}) \times 10^{11}$
850.73		$3.91^{+0.94}_{-1.20}$	0.1	$(7.2^{+25.2}_{-2.1}) \times 10^{12}$	3.1 ± 0.5	$\equiv 2.1$	—	$2.32^{+0.13}_{-0.19}$	$(6^{+9}_{-4}) \times 10^{10}$
850.74		$2.76^{+2.78}_{-1.50}$	0.1	$(1.8^{+6.4}_{-0.5}) \times 10^{12}$	2.5 ± 0.5	$\equiv 2.1$	—	$1.21^{+0.36}_{-0.42}$	$(8^{+10}_{-4}) \times 10^9$
850.76		$1.99^{+0.07}_{-0.22}$	1.4	$(9.1^{+32.0}_{-2.6}) \times 10^{11}$	2.2 ± 0.5	$\equiv 2.1$	—	$2.69^{+0.07}_{-0.07}$	$(5^{+5}_{-5}) \times 10^9$
850.78		$0.94^{+0.01}_{-0.01}$	0.3	$(4.2^{+7.3}_{-2.4}) \times 10^{11}$	1.9 ± 0.2	2.1 ± 0.2	$(3^{+5}_{-2}) \times 10^8$	$0.79^{+0.08}_{-0.07}$	$(1^{+2}_{-1}) \times 10^{10}$
850.80		$3.54^{+0.12}_{-0.15}$	0.2	$(2.8^{+9.8}_{-0.8}) \times 10^{12}$	2.7 ± 0.5	$\equiv 2.1$	—	$1.77^{+0.12}_{-0.36}$	$(4^{+6}_{-3}) \times 10^{10}$
850.81		$0.40^{+0.03}_{-0.03}$	1.3	$(1.4^{+4.9}_{-1.3}) \times 10^{10}$	0.4 ± 0.5	$\equiv 2.1$	—	$-1.45^{+0.35}_{-0.23}$	$(5^{+7}_{-3}) \times 10^8$
850.82		$2.87^{+0.17}_{-0.25}$	1.3	$(6.2^{+11.3}_{-3.4}) \times 10^{12}$	3.0 ± 0.3	1.8 ± 0.2	$(3^{+4}_{-2}) \times 10^8$	$2.10^{+0.08}_{-0.10}$	$(2^{+3}_{-2}) \times 10^{11}$
850.84		$2.42^{+0.38}_{-0.48}$	1.1	$(2.0^{+7.1}_{-0.6}) \times 10^{12}$	2.5 ± 0.6	$\equiv 2.1$	—	$0.68^{+0.40}_{-0.17}$	$(4^{+6}_{-2}) \times 10^9$
850.87		$2.24^{+0.42}_{-0.19}$	0.1	$(4.2^{+7.3}_{-2.4}) \times 10^{12}$	2.9 ± 0.2	1.8 ± 0.2	$(2^{+2}_{-1}) \times 10^8$	$1.07^{+0.62}_{-0.70}$	$(6^{+40}_{-1}) \times 10^9$
850.91		$2.71^{+0.46}_{-0.55}$	0.1	$(2.0^{+7.1}_{-0.6}) \times 10^{12}$	2.5 ± 0.6	$\equiv 2.1$	—	$1.03^{+0.41}_{-0.36}$	$(8^{+10}_{-5}) \times 10^9$
850.94		$2.04^{+0.10}_{-0.21}$	0.1	$(7.3^{+9.1}_{-5.8}) \times 10^{11}$	2.1 ± 0.1	$\equiv 2.1$	—	$2.10^{+0.07}_{-0.07}$	$(1^{+1}_{-1}) \times 10^{11}$
850.95		$1.55^{+0.05}_{-0.08}$	0.2	$(2.2^{+7.9}_{-0.6}) \times 10^{12}$	2.6 ± 0.6	$\equiv 2.1$	—	$2.48^{+0.09}_{-0.28}$	$(8^{+10}_{-7}) \times 10^{10}$
850.97		$0.73^{+0.01}_{-0.01}$	0.1	$(3.4^{+6.4}_{-1.8}) \times 10^{11}$	1.8 ± 0.3	2.1 ± 0.2	$(2^{+4}_{-1}) \times 10^8$	$-3.90^{+1.94}_{-0.88}$	$(2^{+2}_{-2}) \times 10^{11}$

TABLE 9 – CONTINUED.